

**EXPLORING THE ROLE OF LARGE ORGANIC
CATIONS IN HALIDE PEROVSKITE
NANOCRYSTAL FORMATION AND SURFACE
PASSIVATION**

**A Thesis Submitted to
the Graduate School of Engineering and Sciences of
İzmir Institute of Technology
in Partial Fulfillment of the Requirements for the Degree of**

DOCTOR OF PHILOSOPHY

in Materials Science and Engineering

**by
Çetin Meriç GÜVENÇ**

**November 2024
İZMİR**

We approve the thesis of **Çetin Meriç GÜVENÇ**

Examining Committee Members:

Prof. Dr. Sinan BALCI

Department of Photonics, IZTECH

Prof. Dr. Yaşar AKDOĞAN

Department of Materials Science and Engineering, IZTECH

Assoc. Prof. Dr. Engin KARABUDAK

Department of Chemistry, IZTECH

Assoc. Prof. Dr. Muhammed ÜÇÜNCÜ

Department of Pharmaceutical Basic Sciences, IKCU

Assoc. Prof. Dr. Burak GÜLTEKİN

Department of Energy, EU

8 November 2024

Prof. Dr. Sinan BALCI

Supervisor, Department of
Photonics, IZTECH

Assoc. Prof. Dr. Umut ADEM

Co-Supervisor, Material Science
and Engineering, IZTECH

Prof. Dr. Yaşar AKDOĞAN

Head of the Department of
Materials Science and Engineering

Prof. Dr. Mehtap EANES

Dean of the Graduate School

ACKNOWLEDGEMENTS

I would like to express my deepest gratitude to my supervisor, Prof. Dr. Sinan Balcı, for his unwavering support and guidance throughout my PhD journey.

I am also deeply thankful to my wife, Tuğçe, for her patience, encouragement, and support during this challenging and rewarding journey.

My endless gratitude goes to my family, who have always supported me and nurtured my curiosity about science. Their encouragement has been invaluable to my growth as a researcher.

I am profoundly grateful to Prof. Dr. Liberato Manna for his insightful guidance, advice, and discussions, as well as for giving me the opportunity to be part of the Nanochemistry research group.

I extend my heartfelt thanks to Dr. Stefano Toso, Prof. Dr. Giorgio Divitini, Dr. Yurii Ivanov, and Dr. Gabriele Saleh for their valuable help, discussions, and collaboration.

Finally, I would like to thank Dr. Güncem Özgün Eren, Dr. Houman Bahmani Jalali, Dr. Mehmet Zafer Akgül, Umberto Filippi, Anna Cabona, Dr. Ecem Tiryaki, Dr. Ana Maria Panaite, Dr. Pascal Rusch, Dr. Irina Gushchina, Dr. Clara Otero Martinez, Nikolaos Livakas, Dr. Zeynep Kahraman, Necip Ayhan Tertemiz, and Dr. Levent Karacasulu for their valuable help and friendship throughout this journey.

I would like to express my gratitude for the support given by TÜBİTAK (The Scientific and Technological Research Council of Turkey) within the scope of 2214-A-International Research Scholarship Program during my doctoral study.

ABSTRACT

EXPLORING THE ROLE OF LARGE ORGANIC CATIONS IN HALIDE PEROVSKITE NANOCRYSTAL FORMATION AND SURFACE PASSIVATION

Lead halide perovskite nanocrystals have received great attention during the last decade due to their excellent properties such as defect tolerance, tunable bandgaps in the entire visible spectrum, ease of synthesis, near unity photoluminescence quantum yields, fast radiative rates. Perovskite nanocrystals hold great promise for optoelectronic devices such as light-emitting diodes, photodetectors, and devices for quantum technologies. Traditional perovskite nanocrystals can incorporate Cesium (Cs), methylammonium (MA), and formamidinium (FA) cations at the A-site of the perovskite lattice. In this dissertation, we explore the influence of larger cations, specifically guanidinium (GA) and ethylammonium (EA), on the perovskite structure. The first chapter introduces colloidal nanocrystals and provides the fundamentals of halide perovskite nanocrystals. The second chapter presents the synthesis and optical properties of pure $L_2[GAPbI_3]PbI_4$ Ruddlesden-Popper perovskites and their alloys with FA. In the third chapter, we describe the guanidinium-induced formation of $CsPbX_3$ ($X = Cl, Br$) nanocubes at room temperature. GA cannot fit into $APbX_3$ lattice due to its large ionic radius but efficiently passivates perovskite surfaces via its extra amino groups. In the final part, we report the synthesis and characterization of $EAPbI_3$ perovskite nanocrystals as a material $EAPbI_3$ perovskite had never been reported. The new member of the perovskite family has a notably large lattice constant of 6.43 Å. Its photoluminescence (PL) emission can be tuned within the 664–690 nm range by adjusting the nanocrystal size. These findings highlight the potential of large organic cations in tuning both the lattice and surface properties of perovskite nanocrystals.

ÖZET

HALİDE PEROVSKİT NANOKRİSTAL OLUŞUMU VE YÜZEY PASİVASYONUNDA BÜYÜK ORGANİK KATYONLARIN ROLÜNÜN ARAŞTIRILMASI

Kurşun halojenür perovskit nanokristalleri, kusur toleransı, tüm görünür spektrumda ayarlanabilir bant aralıkları, sentez kolaylığı, yüksek fotoluminesans kuantum verimleri, hızlı radyasyon oranları gibi mükemmel özellikleri nedeniyle son on yılda büyük ilgi görmüştür. Perovskit nanokristalleri, ışık yayan diyotlar, fotodedektörler ve kuantum teknolojileri için cihazlar gibi optoelektronik cihazlar için büyük bir gelecek vaat etmektedir. Geleneksel perovskit nanokristalleri, perovskit kafesinin A-bölgesinde Sezyum (Cs), metilamonyum (MA) ve formamidinyum (FA) katyonlarını içerebilir. Bu tezde, daha büyük katyonların, özellikle guanidinyum (GA) ve etilamonyumun (EA) perovskit yapısı üzerindeki etkisini araştırdık. İlk bölümde kolloidal nanokristaller tanıtılmakta ve halide perovskit nanokristallerinin temelleri verilmektedir. İkinci bölümde saf $L_2[GAPbI_3]PbI_4$ Ruddlesden-Popper perovskitlerinin ve FA ile alaşımlarının sentezi ve optik özellikleri sunulmaktadır. Üçüncü bölümde, oda sıcaklığında guanidinyum kaynaklı $CsPbX_3$ ($X = Cl, Br$) nanoküplerinin oluşumunu açıklıyoruz. GA, büyük iyonik yarıçapı nedeniyle $APbX_3$ kafeslerine sığamaz ancak ekstra amino grupları aracılığıyla perovskit yüzeylerini etkili bir şekilde pasifleştirir. Son bölümde, daha önce hiç bildirilmemiş bir malzeme olan $EAPbI_3$ perovskit nanokristallerinin sentezini ve karakterizasyonunu bildiriyoruz. Perovskit ailesinin yeni üyesi, 6,43 Å'lik dikkate değer derecede büyük bir kafes sabitine sahiptir. Fotoluminesans (PL) emisyonu, nanokristal boyutunu ayarlayarak 664–690 nm aralığında ayarlanabilir. Bu bulgular, büyük organik katyonların hem perovskit nanokristallerinin kafes hem de yüzey özelliklerini ayarlamadaki potansiyellerini göstermektedir.

TABLE OF CONTENTS

LIST OF FIGURES.....	viii
LIST OF TABLES.....	xvi
CHAPTER 1. INTRODUCTION TO COLLOIDAL SEMICONDUCTOR NANOCRYSTALS..... 1	
1.1. Definition of Semiconductor Nanocrystals	1
1.2. Quantum Confinement Effect.....	2
1.3. Chemistry of Colloidal Nanocrystals	4
1.4. Nucleation and Growth of Colloidal Nanocrystals	5
1.5. Lead Halide Perovskite Nanocrystals.....	6
1.6. References	8
CHAPTER 2. L ₂ [GA _x FA _{1-x} PbI ₃]PbI ₄ (0 ≤ x ≤ 1) RUDDLESDEN-POPPE PEROVSKITE NANOCRYSTALS FOR SOLAR CELLS AND LIGHT EMITTING DIODES..... 12	
2.1. Introduction	13
2.2. Results and Discussion	15
2.3. Conclusion.....	23
2.4. Experimental Section.....	24
2.4.1. Chemicals.....	24
2.4.2. Synthesis of OLAM-I.....	24
2.4.3. Synthesis of FA-oleate.....	24
2.4.4. Synthesis of GA-oleate.....	24
2.4.5. Synthesis of PbI ₂ Seeds.....	25
2.4.6. Synthesis of PbBr ₂ Seeds.....	25
2.4.7. L ₂ [GA _x FA _{1-x} PbI ₃]PbI ₄	25
2.4.8. Halide Exchange Reactions.....	26
2.4.9. Characterization of NCs.....	26
2.5. References	26

CHAPTER 3. POLAR SOLVENT FREE ROOM TEMPERATURE SYNTHESIS
OF CsPbX₃ (X = Br, Cl) PEROVSKITE NANOCUBES³⁴

3.1. Introduction	35
3.2. Results and Discussion	37
3.3. Conclusion	48
3.4. Materials and Methods	49
3.4.1. Chemicals.....	49
3.4.2. Synthesis of OLAM-X.....	50
3.4.3. Synthesis of Cs-oleate.....	50
3.4.4. Synthesis of GA-oleate.....	50
3.4.5. Synthesis of PbBr ₂ and PbCl ₂ Solution.....	51
3.4.6. CsPbX ₃ Nanocube Synthesis.....	51
3.4.7. Characterization of NCs.....	52
3.4.8. In-situ Absorbance and PL Measurements of NCs.....	52
3.5. References	53

CHAPTER 4. BREAKING THE BOUNDARIES OF THE GOLDSCHMIDT
TOLERANCE FACTOR WITH ETHYLAMMONIUM LEAD
IODIDE PEROVSKITE NANOCRYSTALS.....

4.1. Introduction	61
4.2. Results and Discussion	62
4.3. Conclusion.....	82
4.4. Methods	83
4.4.1. Chemicals.....	82
4.4.2. Synthesis of OLAM-I.....	82
4.4.3. Synthesis of EA-oleate.....	82
4.4.4. Synthesis of Cs-oleate.....	82
4.4.5. Synthesis of FA-oleate.....	83
4.4.6. Synthesis of Pb-precursor with OLAM-I and OA.....	83
4.4.7. Synthesis of Pb-precursor with TOPO.....	83
4.4.8. EAPbI ₃ NC Synthesis from Pb-precursor with OLAM-I and OA...	84
4.4.9. EAPbI ₃ NC Synthesis from Pb-precursor with TOPO.....	84
4.4.10. EAPbI ₃ NPL Synthesis.....	84
4.4.11. Cs or FA Alloyed EAPbI ₃ NC Synthesis.....	85

4.4.12. Optical Characterization.....	85
4.4.13. Powder X-ray Diffraction (XRD) Analysis.....	85
4.4.14. Electron Microscopy.....	86
4.4.15. Atomistic Simulations.....	87
4.5. References	88
CHAPTER 5. CONCLUSION AND OUTLOOK	94
5.1. Conclusion.....	94
5.2. Outlook.....	93

LIST OF FIGURES

<u>Figure</u>	<u>Page</u>
Figure 1.1. (a) The density of the states of bulk, nanocrystal, and atom of metal and semiconductor material, respectively. (b) Effect of dimensional confinement on the density of the states from 3D nanocrystals to 0D quantum dot. ²	2
Figure 1.2. Schematic presentation of the quantum size effect in the semiconductor quantum dots.	3
Figure 1.3. Total Gibbs free energy changes during the formation of solids from monomers. ΔG_v and ΔG_s represents the volume and surface Gibbs free energy, respectively.	6
Figure 1.4. (a) Hot injection ¹⁵ and (b) LARP ²⁰ synthesis methods. Adapted with permission from reference (20). Copyright (2015) American Chemical Society.....	7
Figure 1.5. Schematic of the cubic perovskite unit cell and electronic band structure of the CdSe, GaAs, and CsPbX ₃ . ¹⁴	8
Figure 2.1. Schematic representation of the synthesis route of L ₂ [GA _x FA _{x-1} PbI ₃]PbI ₄ NCs. PbI ₂ was dissolved in OA and OLAM-I solution at elevated temperatures. The prepared precursor solution was diluted with 2 mL of hexane for reducing viscosity of the liquid mixture at room temperature. Subsequently, a definite amount of PbI ₂ precursor solution and a desired ratio of GA-oleate/FA-oleate solution were quickly injected into hexane for the synthesis of L ₂ [GA _x FA _{x-1} PbI ₃]PbI ₄ NCs.....	14
Figure 2.2. Structural characterization of NCs. (a) Powder XRD patterns of L ₂ [GAPbI ₃]PbI ₄ , L ₂ [GA _{0.5} FA _{0.5} PbI ₃]PbI ₄ , and L ₂ [FAPbI ₃]PbI ₄ NCs. (b) Schematic presentation of the stacking multiple NCs. Average thickness of the LHP unit cell and distance between LHP layers were shown. HAADF images of (c) L ₂ [GAPbI ₃]PbI ₄ , (d) L ₂ [GA _{0.5} FA _{0.5} PbI ₃]PbI ₄ , and (e) L ₂ [FAPbI ₃]PbI ₄ NCs. Particle size	

distributions of (f) $L_2[GAPbI_3]PbI_4$, (g) $L_2[GA_{0.5}FA_{0.5}PbI_3]PbI_4$, and (h) $L_2[FAPbI_3]PbI_4$ NCs.	16
Figure 2.3. (a) Large area HAADF image of $L_2[GAPbI_3]PbI_4$ NCs. (b) High magnification HAADF image of the same sample. (c) Energy dispersive spectroscopy (EDS) area scan analysis of NCs which demonstrates $L_2[GAPbI_3]PbI_4$ NCs contain Pb and I atoms.....	17
Figure 2.4. Optical properties of NCs. (a) Absorption and photoluminescence (PL) spectra of $L_2[GAPbI_3]PbI_4$, $L_2[GA_{0.5}FA_{0.5}PbI_3]PbI_4$, and $L_2[FAPbI_3]PbI_4$ NCs. (b) PL lifetime decays of the colloid samples and their photographs were taken under day light (left) and under illumination of 365 nm UV light (right). (c) From left-hand side to right-hand side, $L_2[GAPbI_3]PbI_4$, $L_2[GA_{0.5}FA_{0.5}PbI_3]PbI_4$, and $L_2[FAPbI_3]PbI_4$ NC colloids are placed, respectively.	18
Figure 2.5. (a) PLQY versus FA content graph of $L_2[GA_xFA_{x-1}PbI_3]PbI_4$ NCs. (b, c) Time-dependent degradation of colloids and drop-cast films, respectively. The left-hand side to the right-hand side in the photographs are $L_2[GAPbI_3]PbI_4$, $L_2[GA_{0.5}FA_{0.5}PbI_3]PbI_4$, and $L_2[FAPbI_3]PbI_4$ NCs, respectively.....	20
Figure 2.6. XRD pattern of 1D $FAPbI_3$ NCs. 1D hexagonal ($P6_3mc$) phase of $FAPbI_3$ was obtained after 6 days.	21
Figure 2.7. Halide exchange reaction of $L_2[GAPbI_3]PbI_4$, $L_2[GA_{0.5}FA_{0.5}PbI_3]PbI_4$, and $L_2[FAPbI_3]PbI_4$ NCs via bromide addition. Absorption spectra and normalized PL spectra of $L_2[GAPbI_3]PbI_4$ (a, b), $L_2[GA_{0.5}FA_{0.5}PbI_3]PbI_4$ (e, f), and $L_2[FAPbI_3]PbI_4$ (i, j) NCs, and their corresponding photographs under day light and UV light illumination (d, h, l). Bromide amount in the colloids increases from left-hand side to the right-hand site in the photographs. Bromide mediated PL quenching of $L_2[GAPbI_3]PbI_4$, $L_2[GA_{0.5}FA_{0.5}PbI_3]PbI_4$, and $L_2[FAPbI_3]PbI_4$ NCs (c, g, k).....	22
Figure 3.1. Schematic representation of GA assisted polar solvent free synthesis of the $CsPbX_3$ ($X=Br, Cl$) nanocubes at room-temperature.	37
Figure 3.2. XRD pattern shows the formation of both $CsPbBr_3$ and Cs_4PbBr_6 phases when the molar ratio of Cs/Pb is 2.	38

Figure 3.3. (a) GA-oleate amount (mL) dependent ex-situ absorption spectra of the synthesized nanocrystals. A fixed amount of Cs-oleate was used for varying GA-oleate amounts in the synthesis. Increasing GA amount causes the formation of less quantum confined nanocrystals. (b) Comparison of the absorption spectra of the synthesized nanocrystals from bottom to top: the first absorption spectrum belongs to the synthesis, which does not contain both GA and extra OA, the second absorption spectrum belongs to the synthesis containing extra OA, and the last absorption spectrum belongs to the synthesis containing GA. (c) In-situ absorption spectra of the diluted GA-assisted synthesis (2 mL toluene, 6 μ L GA-oleate, 4 μ L Cs-oleate, 12.5 μ L PbBr₂ were used in the synthesis.). STEM image of the samples, which have molar ratios of GA/OLAM-Br as (d) 0.625/1, (e) 1.25/1, and (f) 5/1. In-situ (g) absorption and (h) PL spectra of the dense GA-assisted synthesis (2 mL GA-oleate, 170 μ L Cs-oleate, and 500 μ L PbBr₂ were used in the synthesis.). (i) PL maxima shift during the synthesis. The dashed line was drawn from 120 seconds. 39

Figure 3.4. In-situ absorption measurement of the synthesis of CsPbBr₃ nanocrystals without addition of GA-oleate (a) in hexane and (b) in toluene. 42

Figure 3.5. (a, b, c) STEM images of the CsPbBr₃, CsPb(Cl_{0.5}Br_{0.5})₃, and CsPbCl₃ nanocubes and (d, e, f) their related particle size distributions, respectively. 44

Figure 3.6. (a) PL and absorption spectra of CsPbBr₃, CsPb(Cl_{0.5}Br_{0.5})₃, and CsPbCl₃ nanocubes. (b) Digital images demonstrate nanocube colloids in front of the white background under the daylight (left), in front of the black background under the daylight (middle), and under the illumination of 365 nm UV light (right). In each digital image, CsPbCl₃, CsPb(Cl_{0.5}Br_{0.5})₃, and CsPbBr₃ nanocube colloids were arranged from left to right, respectively. (c) Time-resolved PL lifetime decays of the CsPbBr₃, CsPb(Cl_{0.5}Br_{0.5})₃, and CsPbCl₃ nanocubes. 45

Figure 3.7. (a) XRD patterns of the CsPbBr₃, CsPb(Cl_{0.5}Br_{0.5})₃, and CsPbCl₃ nanocubes. (b) FTIR spectra of the CsPbBr₃ nanocubes synthesized by

the LARP method, OLAM-Br solution, GA-oleate, and GA modified CsPbBr ₃ nanocubes synthesized in this work.	46
Figure 3.8. (a) demonstrates XRD patterns of the CsPbBr ₃ , CsPb(Cl _{0.5} Br _{0.5}) ₃ , and CsPbCl ₃ nanocubes. XRD diffractograms of the perovskite nanocubes indicate that the synthesized CsPbBr ₃ and CsPbCl ₃ nanocubes have orthorhombic and cubic crystal structures, respectively. As demonstrated in Figure. 3.8, we did not observe any difference at the peak positions in XRD patterns of GA-assisted synthesized CsPbBr ₃ nanocubes and a reference XRD pattern ⁵¹ , which indicates that GA cations did not dope to the 3D perovskite structure.....	46
Figure 3.9. Comparison of the XRD patterns of the GA-assisted synthesized CsPbBr ₃ nanocubes and reference XRD pattern.....	48
Figure 4.1. Optical and structural features of EAPbI ₃ NCs. (a) A colloidal NCs suspension under indoor and UV illumination. (b) Optical absorption and (c) photoluminescence spectra of EAPbI ₃ NCs of different sizes. (d) Bright field TEM image of EAPbI ₃ NCs. (e) HAADF HR-STEM image of an individual NC. Inset: Fourier transform of the lattice-resolved image, compatible with a pseudocubic perovskite structure seen along its [100] zone axis. Note that the sample was alloyed with ~12% Cs ⁺ to enhance the stability under the electron beam. (f) X-ray diffraction pattern of EAPbI ₃ NCs, fitted assuming an R-3c distorted perovskite structure (Le Bail method). (g) Representation of the pseudocubic EAPbI ₃ crystal structure, with the ethylammonium cation positioned at the center of the cage formed by six [PbI ₆] ⁴⁻ octahedra. (h) Goldschmidt tolerance factor for APbI ₃ perovskites with different A cations (MA = methylammonium, ¹³ AZ = aziridinium, ¹⁵ FA = formamidinium, ¹⁴ GA = guanidinium ^{19,24} and, AA = acetamidinium ¹⁹). Lead-iodide perovskites obtained experimentally to date are enclosed by the area shown in blue.	63
Figure 4.2. (a, b, c, d) TEM images of the EAPbI ₃ perovskite nanocrystals, which contain 0.4 M, 0.8 M, 1.4 M, and 1.6 M OA in the final solution, and (d, e, f, h) their related particle size distributions, respectively.	64
Figure 4.3. (a) PL intensity decay curve and (b) spectra recorded for PLQY measurement of EAPbI ₃ perovskite nanocrystals.	65

Figure 4.4. Comparison of the absorption, PL spectra, TEM images, and XRD patterns of the EAPbI ₃ NCs synthesized with two methods used in this study. XRD patterns, absorption, PL spectra, and morphology of the EAPbI ₃ NCs are very similar for both methods.	66
Figure 4.5. Experimental XRD data of the EAPbI ₃ perovskite fitted with cubic prototype.....	67
Figure 4.6. Histogram showing the energy distribution (meV/formula unit) of the 11 EAPbI ₃ configurations obtained through simulated annealing. Representative configurations are shown. the larger, left most one is the lowest-energy structure (putative structural ground state) obtained. Color code for atoms as follows. Pb= grey, I=violet, C=brown, N=blue, H=white.	67
Figure 4.7. Plots of the band gap vs various measures of Pb-I sublattice distortion for the 11 studied EAPbI ₃ configurations. For each plot, the function reported on the vertical axis is shown in black inside the plot. $\text{ang}_{\text{PbIPb}}$ is the angle formed by Pb with two bonded I atoms, and $l_{\text{Pb-I}}$ is the Pb-I bond length. The Pearson correlation coefficient squared (R^2) is reported in blue in each plot.	68
Figure 4.8. Density of states (DOS) and partial charge density for EAPbI ₃ (lowest-energy configuration). The top plot reports the total DOS, while the bottom plot shows the atomic orbital-projected contributions, color legend on the top left. The charge density corresponding to the valence band maximum (from -0.25 eV to Fermi level) and conduction band minimum (from Fermi level to + 1.5 eV) are reported in the insets as yellow and red isosurfaces (isovalues, in VASP units: $5 \cdot 10^{-5}$ and $5 \cdot 10^{-4}$ for valence and $1 \cdot 10^{-5}$ and $1 \cdot 10^{-4}$ for conduction). Color code same as in Figure 4.6.	69
Figure 4.9. Comparison of the 1D EAPbI ₃ crystals synthesized in this work and reference 1D EAPbI ₃ (CCDC-2077393) XRD patterns.....	70
Figure 4.10. (a, b) The time-dependent XRD measurements of the EAPbI ₃ perovskite nanocrystals. XRD analysis demonstrates that phase transformation starts after 2 hours in the drop-cast films of the EAPbI ₃ nanocrystals under ambient conditions. After 24 hours, the EAPbI ₃ perovskite phase completely transforms to δ – EAPbI ₃ phase.	

(b) It is obvious that peak intensities change even 10 hours later, and phase transformation was not complete. 70

Figure 4.11. (a) Transformation of the EAPbI₃ perovskite phase to both 2D structures and the 1D EAPbI₃ simultaneously. Repetitive peaks at the low angle indicate the formation of 2D structures. Further, peaks at 11° and 26° indicate the formation of 1D EAPbI₃ in the black line. The red line demonstrates pure 1D EAPbI₃. (b) Digital images of the drop cast films in the case of the transformation from 3D EAPbI₃ to 2D and 1D EAPbI₃. The film's color was changed from black to orange. Also, it is possible to see some yellow spots related to 1D EAPbI₃ formation in the digital image. 71

Figure 4.12. EAPbI₃ → PbI₂ degradation mechanism under the electron beam. (a) HAADF-STEM images of a pristine EAPbI₃:Cs⁺ NC. (b) Partially degraded (EA_xCs_{1-x})PbI₃/PbI₂ heterostructure, formed as an intermediate while EAI leaves the NC and Cs⁺ concentrates in the remaining pristine perovskite domains. (c) Fully transformed PbI₂ NC, still reminiscent of the initial cuboidal morphology of the perovskite NC. (d-g) Structure models of EAPbI₃ (d), PbI₂ (g) and of the (EA_xCs_{1-x})PbI₃/PbI₂ epitaxial interface in two different directions (e,f). The co-presence of Cs⁺ and EA⁺ cations represents the alloyed nature of perovskite domain (see Figure 4.14 for further discussion). 72

Figure 4.13. Interface supercells and relative orientation of the EAPbI₃ and PbI₂ lattices (in green and orange respectively) for the epitaxial interfaces shown in Figure 4.12e (left) and Figure 4.12f (right). The first interface occurs between the (110) plane of EAPbI₃ and the (10-8) plane of PbI₂, and is characterized by a supercell area of 116 Å² and 6 % strain. The second interface occurs between the (001) plane of EAPbI₃ and the (-114) plane of PbI₂, and is characterized by a supercell area of 82 Å² and 6 % strain. We note that this second epitaxial relation is equivalent to the one reported in Ref.²³ or the PbI₂/FAPbI₃ system. See Ref.³⁶ for details on the interpretation of these diagrams. 73

Figure 4.14. HAADF images of (a) (EA_xCs_{1-x})PbI₃ perovskite domains together with trigonal PbI₂ domain in the single NC. The formation of

(EA_xCs_{1-x})PbI₃/PbI₂ heterostructures can be explained by the instability of the EAPbI₃ phase under an electron beam. (c) Lower magnification image of the (EA_xCs_{1-x})PbI₃/PbI₂ heterostructures. Figure 2b shows an atomic resolution HAADF image of the interface between (EA_xCs_{1-x})PbI₃/PbI₂ domains. The upper part of the images corresponds to the trigonal PbI₂ lattice at [-22-3] projection; it is connected to the (EA_xCs_{1-x})PbI₃ domain. Due to the very high beam sensitivity of the material, this analysis was made only qualitatively based on the intensity of the corresponding atomic columns. In the HAADF image the brightest columns correspond to Pb/I due to the highest average Z number. The minimum contrast corresponds to higher EA containing (EA_xCs_{1-x}) columns. With an increase in Cs doping the contrast of (EA, Cs) columns is increased. The I columns in the ((EA_xCs_{1-x})PbI₃) have a contrast similar to the (EA, Cs) columns enriched in Cs, due to the little difference in Z numbers of I and Cs..... 74

Figure 4.15. Alloys with FA and Cs. Characterization of (EA_xFA_{1-x})PbI₃ NCs (left) and (EA_xCs_{1-x})PbI₃ NCs (right). From left to right and from top to bottom: optical absorption spectra (a,c); PL spectra (b,d); XRD patterns (e,f). The cation alloying ratios are extracted from XRD patterns in panels (e, f) by using Vegard's law.³⁵ The EA:FA ratios for (EA_xFA_{1-x})PbI₃ NCs were estimated to be 100:0 (violet), 60:30 (pink), and 55:45 (gray) (e). The EA:Cs ratios in (EA_xCs_{1-x})PbI₃ NCs were determined to be approximately 100:0 (violet), 75:25 (green), 60:40 (orange), and 30:70 (red) from bottom to top (f). 75

Figure 4.16. Spectra recorded for PLQY measurement of (a) EAPbI₃, (b) (Cs, EA)PbI₃, and (c) (FA, EA)PbI₃ perovskite NCs, respectively..... 76

Figure 4.17. EAPbI₃ nanoplatelets. (a, b) Optical absorption (a) and PL (b) spectra of EAPbI₃ samples obtained with different concentrations of EA-oleate in the synthesis. The samples prepared with low EA-oleate concentration show the onset of a sharp excitonic peak, attributed to EAPbI₃ nanoplatelets with a thickness as small as 2 PbI₆ octahedra (2ML in short). (c) TEM images of 2ML EAPbI₃, highlighting the characteristic face-to-face stacking. (d) Structure representation of a

stack of 2ML EAPbI ₃ nanoplatelets, constructed according to the structural parameters extracted from the multilayer diffraction fit. (e) XRD pattern of 2ML EAPbI ₃ analyzed via multilayer diffraction. The characteristic series of periodic peaks is a signature of the self-assembly of the nanoplatelets into flat and ordered stacks. ³⁹⁻⁴²	78
Figure 4.18. Low magnification and TEM images of the two monolayers EAPbI ₃ nanoplatelets.	79
Figure 4.19. (a, b) Bright field TEM images of the mixed thickness EAPbI ₃ nanoplatelets in different magnifications.	79
Figure 4.20. The pattern was prepared for the fit by performing a manual background subtraction (top), followed by the subtraction of residual peaks which do belong to EAPbI ₃ nanoplatelets, but distributed in the wrong orientation (i.e., not lying flat and parallel to the substrate, and therefore not taking part to the multilayer interference). The resulting XRD pattern has been used as an input for the multilayer diffraction analysis script from Ref. ⁴⁰	80
Figure 4.21. Multilayer diffraction simulation of the EAPbI ₃ nanoplatelets XRD Pattern. Although the quality of the pattern was insufficient for an accurate fit, the XRD profile is fully compatible with a thickness of 2 PbI ₆ octahedra, corresponding to a nominal stoichiometry of (OLAM) ₂ EAPb ₂ I ₇ . The multilayer periodicity was estimated from the fit to 39.5 Å, while the stacking disorder parameter is estimated to $\sigma_L = 0.8$ Å (see Ref. ⁴⁰ for a full description of the method and parameters). The intensity profile in Figure S16 appears different from both Figure S15 and Figure 4 of the Main Text (note the different intensity ratio of peaks in the 0.5 – 1.25 Å ⁻¹ and 1.5 – 2.25 Å ⁻¹ range) because the data analysis script adopted works by fitting the square module of the structure factor (shown here), and not the experimental intensity (shown in the main text). The two profiles can be interconverted via the Lorentz-Polarization correction factor. ⁴³	81
Figure 4.22. Optical absorbance and PL spectra of the 2 ML EAPbI ₃ nanoplatelets as prepared (black) and after 3 days of aging (red) under ambient conditions in a closed vial.	82

LIST OF TABLES

<u>Table</u>	<u>Page</u>
Table 2.1. Time-resolved photoluminescence lifetime profiles for $L_2[GA_xFA_{1-x}PbI_3]PbI_4$ NCs, which are fitted with a biexponential function.	19
Table 3.1. Time resolved photoluminescence life-time decays of $CsPbBr_3$, $CsPb(Cl_{0.5}Br_{0.5})_3$, and $CsPbCl_3$ nanocubes.	46
Table 4.1. Extracted lattice parameters from XRD patterns of the $EA_xFA_{(1-x)}PbI_3$ NCs. The corresponding composition (here indicating the fraction of EA^+ and FA^+ present in the alloy), was estimated by applying Vegard's law: $x = (d_x - d_B)/(d_A - d_B)$, where d_x , d_A , and d_B are the measured lattice constants of the alloy and of the pure materials A and B , respectively.	76
Table 4.2. Extracted lattice parameters from XRD patterns of the $EA_xFA_{(1-x)}PbI_3$ NCs. The corresponding composition (here indicating the fraction of EA^+ and FA^+ present in the alloy) was estimated by applying Vegard's law: $x = (d_x - d_B)/(d_A - d_B)$, where d_x , d_A , and d_B are the measured lattice constants of the alloy and of the pure materials A and B , respectively.	77

CHAPTER 1

INTRODUCTION TO COLLOIDAL SEMICONDUCTOR NANOCRYSTALS

Abstract

Semiconducting materials are of great importance due to their applications in areas such as light-emitting diodes (LEDs), solar cells, photodetectors, and quantum information technologies. Consequently, considerable effort has been made to discover new semiconducting materials and compositions. Furthermore, one of the most straightforward and scalable approaches is to synthesize these materials in colloidal form. This thesis aims to develop new colloidal synthesis routes and explore novel perovskite nanocrystal materials that incorporate large A-site cations. This chapter provides a brief overview of the optical and structural properties of colloidal nanocrystals and their synthesis techniques.

1.1. Definition of Semiconductor Nanocrystals

Materials that have at least one dimension between 1 and 100 nm are called nanomaterials. These nanomaterials can be classified into three categories: zero-dimensional, one-dimensional, and two-dimensional. Zero-dimensional materials have dimensions between 1 and 100 nanometers in all of the three dimensions. Examples of zero-dimensional materials are quantum dots and magic-size clusters. One-dimensional materials have nanoscale dimensions in only two dimensions, such as nanowires, nanotubes, and nanoribbons. Two-dimensional materials have nanoscale size in only one of their three dimensions, such as nanoplates, nanosheets, and ultra-thin films. Importantly, the size of semiconductor nanocrystals can be precisely controlled at the nanoscale, allowing the tuning of their optical properties.^{1,2} On the other hand, it is not possible to mention the size-dependent properties in bulk semiconductor materials. Decreasing the size of semiconductor nanocrystals leads to an increase in band gap energy

(see Figure 1.1). This size quantization effect was first observed and described by Brus and Ekimov.³⁻⁸ It should be noted that they successfully synthesized semiconductor quantum dots in the glass or solution media.⁴ With the advent of colloid chemistry, numerous types of semiconducting materials have been successfully synthesized in the form of nanocrystals. These nanocrystals are highly significant for various optoelectronic applications due to their tunable photoluminescence (PL) and absorption, high PL quantum yield, narrow emission linewidth, and ease of synthesis.

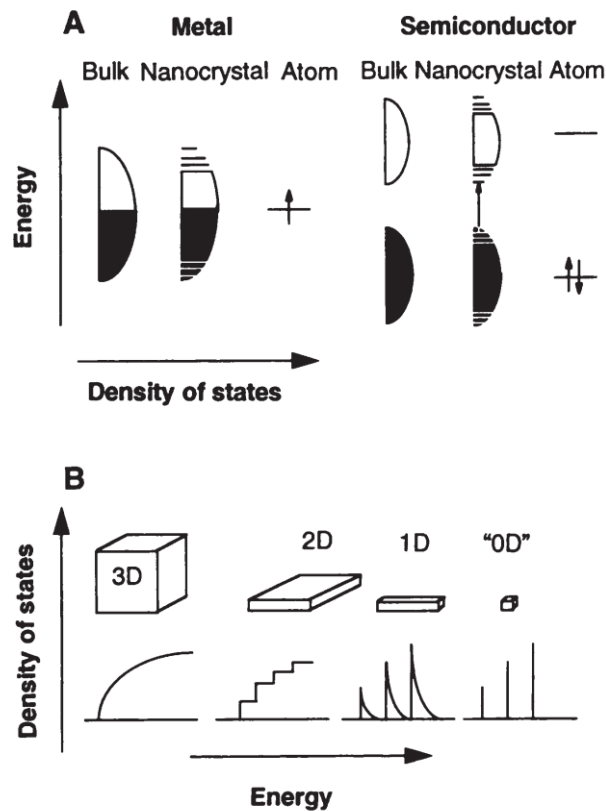


Figure 1.1. (a) The density of the states of bulk, nanocrystal, and atom of metal and semiconductor material, respectively. (b) Effect of dimensional confinement on the density of the states from 3D nanocrystals to 0D quantum dot.²

1.2. Quantum Confinement Effect

The size-dependent optical properties of semiconductor nanocrystals are caused by the quantum confinement effect. According to the Heisenberg uncertainty principle, as the uncertainty in the position of a particle decreases in a confined space, the uncertainty in its momentum increases. This increase in the particle's uncertainty of

momentum leads to higher kinetic energy. When this increase in kinetic energy becomes comparable to or exceeds the energy associated with the particle's thermal motion, quantum confinement effects become observable. As the size of a semiconductor nanocrystal decreases, the electron and hole wavefunctions become confined to a smaller space, leading to higher charge carrier energies than the bulk material. This size reduction transforms the material's band structure from continuous to discrete energy levels. The decrease in size reduces the number of atoms in the nanocrystal, increasing the energy of individual atomic orbitals and widening the band gap because of the quantum confinement effect (see Figure 1.2).^{2,4,7}

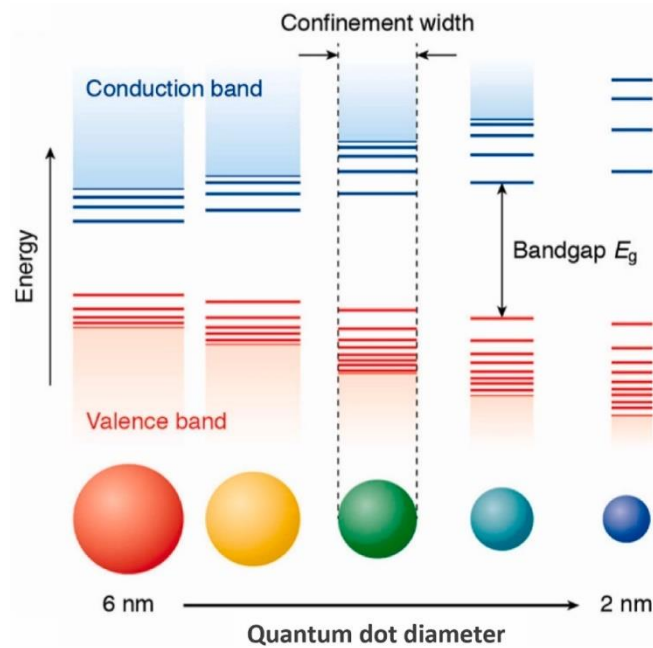


Figure 1.2. Schematic presentation of the quantum size effect in the semiconductor quantum dots.

Furthermore, the quantum confinement effect can be explained using the exciton Bohr radius of the material. When an electron is excited from the valence band to the conduction band, it leaves a hole behind in the valence band. This electron and hole are bound together by Coulombic forces and form an exciton. This space is covered by an exciton called an exciton Bohr radius (a_0) of the material, as is depicted in equation 1.

$$\text{Exciton Bohr radius } (a_0) = \frac{\hbar^2 \epsilon}{e^2} \left(\frac{1}{m_e^*} + \frac{1}{m_h^*} \right) \quad (1)$$

As shown in the equation, the exciton Bohr radius depends on the effective masses of the electron and the hole, which in turn depend on the material and vary from one material to another for example, InSb, PbS, CdSe and CsPbBr₃ have 61 nm, 21 nm, 4 nm, and 5 nm exciton Bohr radius, respectively.⁹ When the size of the nanocrystal becomes comparable to the exciton Bohr radius, the exciton can no longer move freely, unlike in bulk semiconductors. As the nanocrystal size decreases further, below the exciton Bohr radius, the exciton becomes more confined, resulting in an increase in its energy, like in the particle in a box. The band gap of a spherical nanocrystal can be calculated using the Brus equation, as demonstrated in Equation 2.

$$E_{QD} = E_{gap} + \frac{h^2}{8r^2} \left(\frac{1}{m_e^*} + \frac{1}{m_h^*} \right) \quad (2)$$

1.3. Chemistry of Colloidal Nanocrystals

Colloidal nanocrystals consist of two components: an inorganic semiconducting nanocrystal core and an organic ligand shell. The ligand shell influences the colloidal stability, surface passivation, shape, and size of the nanocrystal. Ligands contain both hydrophobic (tail) and hydrophilic (head) groups. The hydrophilic polar head can include amines, carboxylic acids, or phosphines, while the hydrophobic tail is composed of alkyl or alkenyl chains. Active head groups are attached to nanocrystal surfaces. Ligands can be divided into three types^{10,11}, depending on how they bind to the nanocrystal surface. L-type ligands are charge neutral Lewis bases that can donate lone pairs of electrons to metal atoms like amines and phosphines. X-type ligands are anionic ligands like carboxylates and thiolates. Lastly, Z-type ligands are cationic ligands, such as metal halides, that accept electrons from the nanocrystal, acting as Lewis acids. It is important to understand the binding types of ligands on the passivated surfaces of nanocrystals. Nanocrystals have a large surface area relative to their size, and surface atoms must be well-passivated. Uncoordinated surface atoms, also known as dangling bonds¹², can create trap states within the band gap, acting as nonradiative recombination centers that degrade the optical properties. For example, in CdSe nanocrystals, uncoordinated Cd atoms form trap states just below the conduction band. These Cd atoms can be passivated with L-type ligands such as amines or phosphines, which hybridize with the dangling bonds, leading to the formation of highest occupied molecular orbital (HOMO) and

lowest unoccupied molecular orbital (LUMO) levels within the valence and conduction bands. Furthermore, in some materials, dangling bonds do not form trap states within the band gap. Instead, trap states form within the conduction and valence bands. We call these materials defect-tolerant materials. A common example of such a material is CsPbBr₃.

1.4. Nucleation and Growth of Colloidal Nanocrystals

We can divide the colloidal synthesis of nanocrystals into three main stages: pre-nucleation, nucleation, and growth. In the pre-nucleation stage, monomers begin forming very small nuclei. Typically, precursors are prepared by complexing metal salts and non-metals with ligands. In the second step, stable nuclei form. Notably, the monomer concentration must reach at least the critical saturation concentration to initiate nucleation; below this level, monomers remain dissolved. At the same point above, the critical concentration system reaches supersaturation concentration, which means where the concentration exceeds equilibrium solubility. That concentration causes rapid nucleation and growth of nanocrystals. After that, the system reaches minimal concentration. In this stage, the formation of new nuclei is not possible; only the addition of monomers to existing nuclei occurs, leading to growth.

From a physical point of view, classical nucleation theory describes the nucleation and growth of nanocrystals. La Mer adopted this theory to explain the formation of solid nanocrystals in liquid media.¹³ In classical nucleation theory, two energy contributions are considered: bulk energy (ΔG_v , negative) and surface energy (ΔG_s , positive). Nucleation occurs when the Gibbs free energy contribution from the bulk becomes dominant (see Figure 1.3). The overall Gibbs free energy is expressed in equation 3 below:

$$\Delta G = \Delta G_v + \Delta G_s = \frac{4\pi}{3} r^3 \frac{-k_B T \ln(S)}{v} + 4\pi r^2 \gamma \quad (3)$$

In here, r is the radius of the nanocrystal, T is the temperature, S is the super saturation of the solution, k_B is the Boltzmann's constant, v is the molar volume, and γ is the surface area energy.

Critical Gibbs free energy (ΔG^*) is considered the energy barrier that must be overcome to initiate nucleation. The corresponding particle radius at this energy is called

critical size (r^*). Particles smaller than r^* dissolve into their monomers, while larger ones tend to grow. It should be noted that particles equal to r^* neither grow nor dissolve, as they are in a metastable equilibrium with the solution. r^* can be identified as the following equation:

$$r^* = \frac{2\gamma v}{\Delta\mu} \quad (4)$$

Here $\Delta\mu$ is the difference between the chemical potentials. Further, prolonged growth periods can lead to Ostwald ripening. At low temperatures or low monomer concentrations, the r^* becomes larger. This increase in r^* promotes Ostwald ripening, where larger particles grow at the expense of smaller ones.

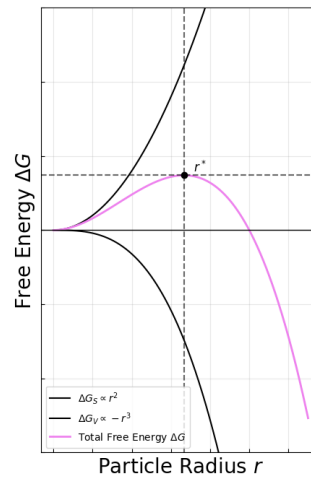


Figure 1.3. Total Gibbs free energy changes during the formation of solids from monomers. ΔG_v and ΔG_s represents the volume and surface Gibbs free energy, respectively.

1.5. Lead Halide Perovskite Nanocrystals

Halide perovskite nanocrystals have attracted significant attention in recent years due to their unique optical and optoelectronic properties. These materials show great promise for applications such as light-emitting diodes, photodetectors, and solar cells, owing to their narrow photoluminescent line widths, tunable bandgaps, high defect tolerance, and highly localized energy levels.¹⁴⁻¹⁶

The Goldschmidt tolerance factor¹⁷ is used to empirically determine the suitable A-site cations, B-site cations, and X-site anions that can form the perovskite structure based on a geometric approach. For halide perovskites, the tolerance factor t is calculated using the formula:

$$t = \frac{r_A + r_X}{[\sqrt{2}(r_B + r_X)]} \quad (5)$$

Where t is the tolerance factor, r_A is the effective radius of the A-site cation in 12-fold coordination, r_B is the radius of the B-site cation in 6-fold coordination, and r_X is the radius of the halide anion in 6-fold coordination. In general, tolerance factors between 0.8 and 1 are considered favorable for forming stable perovskite structures. Traditional A-site cations that support the formation of halide perovskite lattices include cesium (Cs), methylammonium (MA), and formamidinium (FA). The radii of these cations in 12-fold coordination are 188 pm, 217 pm, and 253 pm, respectively.^{18–20}

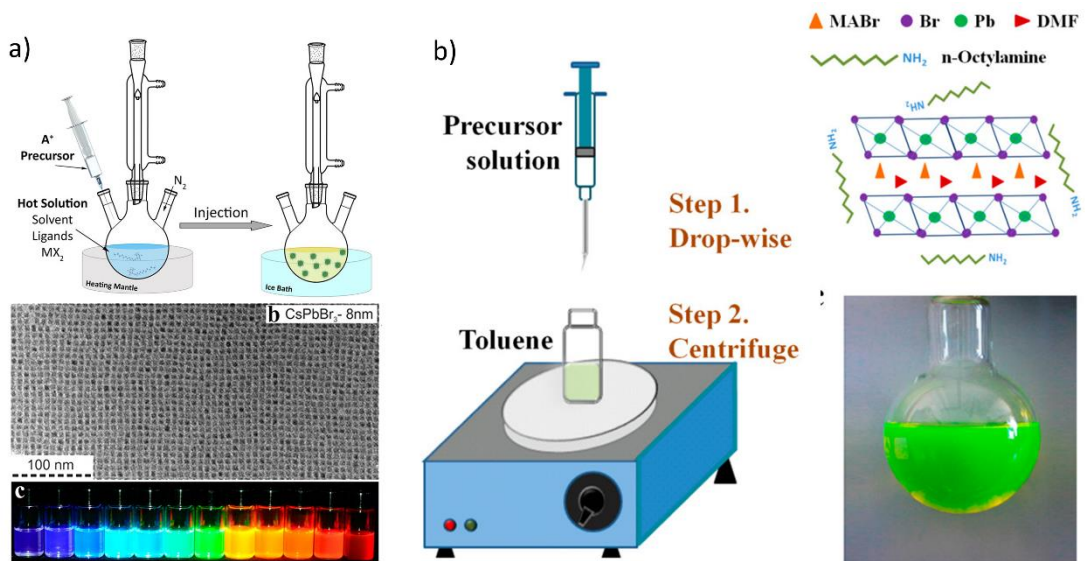


Figure 1.4. (a) Hot injection¹⁵ and (b) LARP²⁰ synthesis methods. Adapted with permission from reference (20). Copyright (2015) American Chemical Society

Generally, halide perovskite nanocrystals are synthesized using ligand-assisted reprecipitation (LARP) or hot-injection methods. In the hot-injection method, PbX_2 salt is dissolved in a high-boiling solvent with the help of ligands at elevated temperatures. Once the PbX_2 salt dissolves and the solution reaches the target temperature, the A-site

cation-oleate solution is injected into the reaction medium.¹⁹ The reaction is quickly quenched in an ice bath to halt further growth. In the LARP method²⁰, PbX_2 and A-site cation halide salts (AX) are dissolved in polar solvents like dimethyl sulfoxide or dimethylformamide and injected into a non-polar solvent (e.g., hexane or toluene) in the presence of ligands to form perovskite nanocrystals. Figure 1.4 illustrates both hot injection and LARP methods. In both approaches, surface passivation is achieved by metal carboxylate and alkylammonium halides.

It is worth noting that the defect tolerance of lead halide perovskites makes them unique among semiconductor materials. The quality of thin films or nanocrystals is crucial for optoelectronic and electronic applications, as traditional semiconductors require minimal defect concentrations for devices like photovoltaics. However, perovskites are highly tolerant of both material and surface defects. This tolerance arises from several factors: only vacancies appear as point defects, while interstitials and anti-site defects are rare due to the high energetic cost of ion misplacement. Additionally, as shown in Figure 1.5, vacancy-related states are typically shallow in character.^{14,21,22}

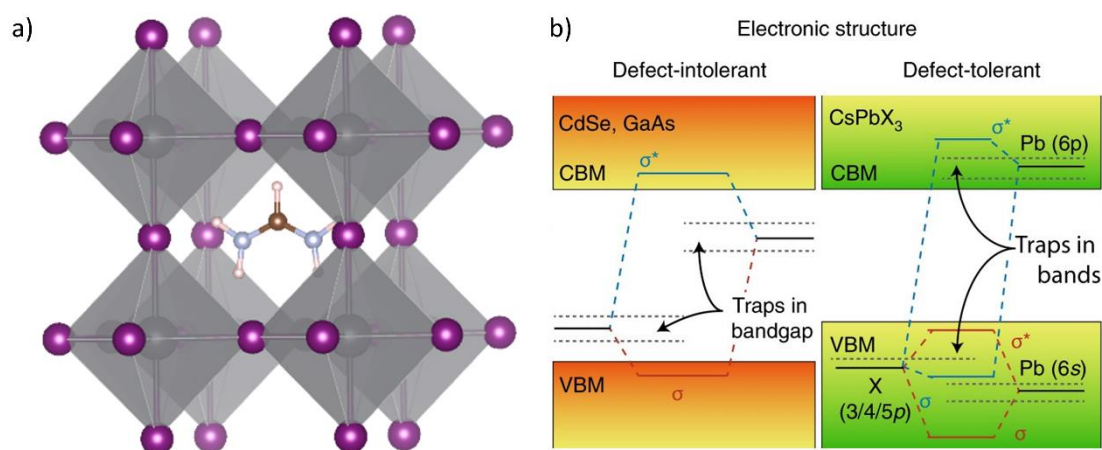


Figure 1.5. Schematic of the cubic perovskite unit cell and electronic band structure of the CdSe, GaAs, and CsPbX₃.¹⁴

1.6. References

1. Steigerwald, M. L.; Brus, L. E. Semiconductor Crystallites: A Class of Large Molecules. *Acc Chem Res* **1990**, *23* (6), 183–188.
2. Alivisatos, A. P. Semiconductor Clusters, Nanocrystals, and Quantum Dots. *Science (1979)* **1996**, *271* (5251), 933–937.

3. Brus, L. *Electronic Wave Functions In Semiconductor Clusters: Experiment and Theory*; **1986**; Vol. 90.
4. Ekimov, A. I.; Efros, Al. L.; Onushchenko, A. A. Quantum Size Effect in Semiconductor Microcrystals. *Solid State Commun* **1993**, *88* (11–12), 947–950.
5. Rossetti, R.; Nakahara, S.; Brus, L. E. Quantum Size Effects in the Redox Potentials, Resonance Raman Spectra, and Electronic Spectra of CdS Crystallites in Aqueous Solution. *J Chem Phys* **1983**, *79* (2), 1086–1088.
6. Brus, L. E. Electron-Electron and Electron-Hole Interactions in Small Semiconductor Crystallites: The Size Dependence of the Lowest Excited Electronic State. *J Chem Phys* **1984**, *80* (9), 4403–4409.
7. Bawendi, M. G.; Steigerwald, M. L.; Brus, L. E. *The Quantum Mechanics of Larger Semiconductor Clusters (“Quantum Dots”)*; **1990**; Vol. 41.
8. Brus, L. E. A Simple Model for the Ionization Potential, Electron Affinity, and Aqueous Redox Potentials of Small Semiconductor Crystallites. *J Chem Phys* **1983**, *79* (11), 5566–5571.
9. Krauss, T. D.; Peterson, J. J. Electronic Structure and Optical Transitions in Colloidal Semiconductor Nanocrystals. In *Colloidal Quantum Dot Optoelectronics and Photovoltaics*; Cambridge University Press, **2013**; pp 59–86.
10. De Roo, J.; De Keukeleere, K.; Hens, Z.; Van Driessche, I. From Ligands to Binding Motifs and Beyond; The Enhanced Versatility of Nanocrystal Surfaces. *Dalton Transactions* **2016**, *45* (34), 13277–13283.
11. Owen, J. The Coordination Chemistry of Nanocrystal Surfaces. *Science* **2015**, *347* (6222), 615–616.
12. Boles, M. A.; Ling, D.; Hyeon, T.; Talapin, D. V. The Surface Science of Nanocrystals. *Nat Mater* **2016**, *15* (2), 141–153.
13. Thanh, N. T. K.; Maclean, N.; Mahiddine, S. Mechanisms of Nucleation and Growth of Nanoparticles in Solution. *Chemical Reviews* **2014**, *114* (15) 7610–7630.
14. Akkerman, Q. A.; Rainò, G.; Kovalenko, M. V.; Manna, L. Genesis, Challenges and Opportunities for Colloidal Lead Halide Perovskite Nanocrystals. *Nat Mater* **2018**, *17* (5), 394–405.
15. Shamsi, J.; Urban, A. S.; Imran, M.; De Trizio, L.; Manna, L. Metal Halide Perovskite Nanocrystals: Synthesis, Post-Synthesis Modifications, and Their Optical Properties. *Chem Rev* **2019**, *119* (5), 3296–3348.

16. Dey, A.; Ye, J.; De, A.; Debroye, E.; Ha, S. K.; Bladt, E.; Kshirsagar, A. S.; Wang, Z.; Yin, J.; Wang, Y.; Quan, L. N.; Yan, F.; Gao, M.; Li, X.; Shamsi, J.; Debnath, T.; Cao, M.; Scheel, M. A.; Kumar, S.; Steele, J. A.; Gerhard, M.; Chouhan, L.; Xu, K.; Wu, X.; Li, Y.; Zhang, Y.; Dutta, A.; Han, C.; Vincon, I.; Rogach, A. L.; Nag, A.; Samanta, A.; Korgel, B. A.; Shih, C.-J.; Gamelin, D. R.; Son, D. H.; Zeng, H.; Zhong, H.; Sun, H.; Demir, H. V.; Scheblykin, I. G.; Mora-Seró, I.; Stolarczyk, J. K.; Zhang, J. Z.; Feldmann, J.; Hofkens, J.; Luther, J. M.; Pérez-Prieto, J.; Li, L.; Manna, L.; Bodnarchuk, M. I.; Kovalenko, M. V.; Roeffaers, M. B. J.; Pradhan, N.; Mohammed, O. F.; Bakr, O. M.; Yang, P.; Müller-Buschbaum, P.; Kamat, P. V.; Bao, Q.; Zhang, Q.; Krahne, R.; Galian, R. E.; Stranks, S. D.; Bals, S.; Biju, V.; Tisdale, W. A.; Yan, Y.; Hoye, R. L. Z.; Polavarapu, L. State of the Art and Prospects for Halide Perovskite Nanocrystals. *ACS Nano* **2021**, *15* (7), 10775–10981.
17. Goldschmidt, V. M. Die Gesetze Der Krystallochemie. *Naturwissenschaften* **1926**, *14* (21), 477–485.
18. Protesescu, L.; Yakunin, S.; Kumar, S.; Bär, J.; Bertolotti, F.; Masciocchi, N.; Guagliardi, A.; Grotevent, M.; Shorubalko, I.; Bodnarchuk, M. I.; Shih, C.-J.; Kovalenko, M. V. Dismantling the “Red Wall” of Colloidal Perovskites: Highly Luminescent Formamidinium and Formamidinium-Cesium Lead Iodide Nanocrystals. *ACS Nano* **2017**, *11* (3), 3119–3134.
19. Protesescu, L.; Yakunin, S.; Bodnarchuk, M. I.; Krieg, F.; Caputo, R.; Hendon, C. H.; Yang, R. X.; Walsh, A.; Kovalenko, M. V. Nanocrystals of Cesium Lead Halide Perovskites (CsPbX₃, X = Cl, Br, and I): Novel Optoelectronic Materials Showing Bright Emission with Wide Color Gamut. *Nano Lett* **2015**, *15* (6), 3692–3696.
20. Zhang, F.; Zhong, H.; Chen, C.; Wu, X.; Hu, X.; Huang, H.; Han, J.; Zou, B.; Dong, Y. Brightly Luminescent and Color-Tunable Colloidal CH₃NH₃PbX₃ (X = Br, I, Cl) Quantum Dots: Potential Alternatives for Display Technology. *ACS Nano* **2015**, *9* (4), 4533–4542.
21. Huang, H.; Bodnarchuk, M. I.; Kershaw, S. V.; Kovalenko, M. V.; Rogach, A. L. Lead Halide Perovskite Nanocrystals in the Research Spotlight: Stability and Defect Tolerance. *ACS Energy Letters*, American Chemical Society, **2017**, *2* (9), 2071–2083.

22. Kang, J.; Wang, L. W. High Defect Tolerance in Lead Halide Perovskite CsPbBr₃. *Journal of Physical Chemistry Letters* **2017**, *8* (2), 489–493.

CHAPTER 2

L₂[GA_xFA_{1-x}PbI₃]PbI₄ (0 ≤ x ≤ 1) RUDDLESDEN-POPPER PEROVSKITE NANOCRYSTALS FOR SOLAR CELLS AND LIGHT EMITTING DIODES

Reprinted with permission from *ACS Appl Nano Mater* **2022**, 5 (1), 1078–1085.
Copyright 2022 American Chemical Society.

Abstract

The main challenges to overcome for colloidal 2D Ruddlesden–Popper (RP) organo-lead iodide perovskite nanocrystals (NCs) are phase instability and low photoluminescence quantum yield (PLQY). Herein, we demonstrate colloidal synthesis of guanidinium (GA)-L₂[GAPbI₃]PbI₄, formamidinium (FA)-L₂[FAPbI₃]PbI₄, and GA and FA alloyed L₂[GA_{0.5}FA_{0.5}PbI₃]PbI₄ NCs without using polar or high boiling point nonpolar solvents. Importantly, we show that optical properties and phase stability of L₂[APbI₃]PbI₄ NCs can be affectively tuned by alloying with guanidinium and formamidinium cations. Additionally, the bandgap of NCs can be rapidly engineered by bromide ion exchange in L₂[GA_xFA_{1-x}PbI₃]PbI₄ (0 ≤ x ≤ 1) NCs. Our approach produces a stable dispersion of L₂[FAPbI₃]PbI₄ NCs with 12.6 % PLQY that is at least three times higher than the previously reported PLQY in the nanocrystals. Furthermore, L₂[GAPbI₃]PbI₄ and L₂[GA_{0.5}FA_{0.5}PbI₃]PbI₄ NC films exhibit improved ambient stability over ten days, which is significantly higher than L₂[FAPbI₃]PbI₄ NC films, which transform to undesired 1D phase within six days. The colloiddally synthesized guanidinium and formamidinium based 2D RP organo-lead iodide perovskite NCs with improved stability and high PLQY demonstrated in this study may find applications in solar cells, and light emitting diodes. Therefore, large A-site cation alloyed 2D RP perovskite NCs may provide a new way for rationalization of high-performance and stable perovskite solar cells, and light emitting diodes.

2.1. Introduction

Optical and structural properties of 2D Ruddlesden–Popper (RP) halide perovskite crystals with a general formula of $L_2[ABX_3]_{n-1}BX_4$ (L = ligand, A = monovalent cation, B = divalent cation, X = halide anion, n = number of the octahedral layer) were well studied in the past due to their enhanced oscillator strength, large exciton binding energies, and optical nonlinearities.¹⁻⁴ Recently, colloidal synthesis of 2D lead halide perovskite (LHP) nanocrystals have been demonstrated by a number of different research groups.⁵⁻¹¹ Colloidally synthesized 2D LHP NCs show significantly improved optical properties than their bulk crystals, and thus they have been attracting increasing attention in recent years. Most importantly, owing to their unique optical properties, they hold great promise for future optoelectronic, electronic, and photonic applications.^{7, 11-17} It should be noted that, 2D RP perovskite solar-cells have long term operational stability against light soaking and humidity in contrast to 3D perovskite devices.¹⁸ Also, The color purity and luminance of 2D RP perovskite LEDs are promising.^{19, 20}

The LHP crystal structure consists of eight corner-sharing PbX_6 octahedra arranged in a cuboid cage. A-site cation occupies 12-fold coordination within the cage. Geometric considerations of the empirical Goldschmidt tolerance factor (t) limits the possible A-site, B-site, and X-site cations and anions in the perovskite cages,²¹ $t = (r_A + r_X)/[\sqrt{2}(r_B + r_X)]$ where r_A is the radius of A-site cation, r_B is the radius of B-site cation, and r_X is the radius of anion in the perovskite structure. In fact, the values ranging from 0.8 to 1 are generally accepted as favorable tolerance factor values for perovskite structures. Furthermore, the tolerance factors of the synthesized LHP crystals range from 0.89 to 1.09. Obviously, these values confirm that the empirical and experimentally observed tolerance factors are very close approximation.²²⁻²⁶ $L_2[APbI_3]PbI_4$ NCs are typically synthesized by using A-site cations like cesium, methylammonium, and formamidinium. $CsPbI_3$, $MAPbI_3$, and $FAPbI_3$ have Goldschmidt tolerance factors of 0.89, 0.91, and 0.99, respectively. Recently, ligand-assisted reprecipitation technique has been used to synthesize 2D $L_2[APbI_3]PbI_4$ nanoplatelets with large organic A-site cations such as dimethylammonium (DMA), ethylammonium (EA), acetamidinium (AA), and guanidinium (GA).²⁷ Goldschmidt tolerance factors of perovskite structures are in between $1.03 \leq t \leq 1.05$. As a result, perovskites with large A-site cations are not in the favorable range of the Goldschmidt tolerance factor. However, these perovskite structures

are stable due to migrations of strain accumulation and self-adjustable strain balancing effects of the 2D RP phase.²⁸ $L_2[GAPbI_3]PbI_4$ has the highest PLQY among 2D RP LHP NPLs with large cations in the A-site.²⁷ Furthermore, single crystals of $L_2[GAPbI_3]PbI_4$ have higher photostability than $L_2[MAPbI_3]PbI_4$.²⁸

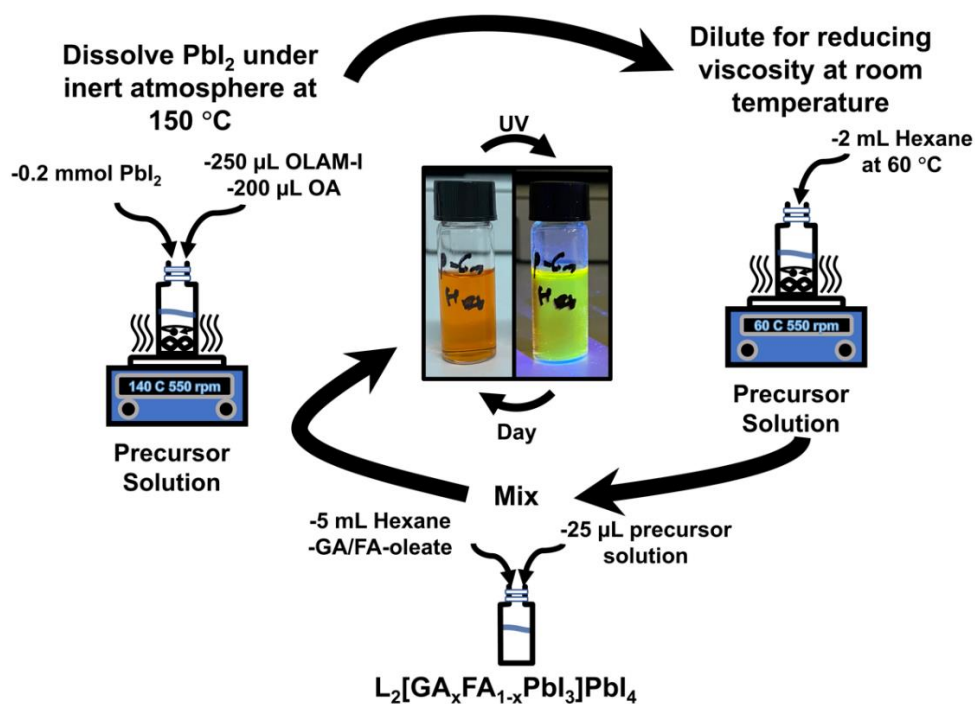


Figure 2.1. Schematic representation of the synthesis route of $L_2[GA_xFA_{1-x}PbI_3]PbI_4$ NCs. PbI_2 was dissolved in OA and OLAM-I solution at elevated temperatures. The prepared precursor solution was diluted with 2 mL of hexane for reducing viscosity of the liquid mixture at room temperature. Subsequently, a definite amount of PbI_2 precursor solution and a desired ratio of GA-oleate/FA-oleate solution were quickly injected into hexane for the synthesis of $L_2[GA_xFA_{1-x}PbI_3]PbI_4$ NCs.

The key factors to resolve for further development of colloidal 2D LHP are phase instability and low PLQYs.^{6, 10, 15, 27, 29, 30} Various strategies, such as A or B-site cation substitution, have been used in order to improve the stability and optical properties of LHP.³⁰⁻³⁵ A variety of organic or inorganic A-site cations are doped or alloyed to improve the stability and performance of LHP thin films and NCs.³⁶⁻⁴¹ For example, GA alloyed LHP solar cells exhibit longer charge carrier lifetimes, higher stability, and improved device performance.³⁷⁻⁴¹ In a recent work, GA doped $FAPbBr_3$ 3D LHP NCs have displayed improved stability, optical properties, and electroluminescence efficiency due

to the bulk entropy stabilization, surface stabilization, and improved electron-hole confinement effects of the GA cations.⁴² In fact, alloying traditional LHP NCs with large A-site cations is a new field that requires further research. Large A-site cations can indeed provide a new way to tune the optical and structural properties of the LHP NCs. We anticipate that our work provides further understanding of the RP LHP NCs.

2.2. Results and Discussion

In this study, we colloiddally synthesized 2D RP $L_2[GA_xFA_{1-x}PbI_3]PbI_4$ ($0 \leq x \leq 1$) ($n = 2$) NCs as schematically illustrated in Figure 2.1. We indeed used the seed mediated synthesis of perovskite NCs.⁴³ Different from the previous study, in this study, we used 0.4 M oleylammonium iodide (OLAM-I) in oleylamine (OLAM) instead of using OLAM. Halide defect concentration of NCs was affectively reduced by extra iodide ions from OLAM-I. Because of the decreased halide defect concentration, the PLQY of NCs increases.^{12, 44-47} Therefore, we observed that the PLQY of $L_2[FAPbI_3]PbI_4$ increased from 1.66 % to 12.6 %. To the best of our knowledge, the synthesized $L_2[FAPbI_3]PbI_4$ NCs have at least three times higher PLQY than the previously synthesized $L_2[FAPbI_3]PbI_4$ nanocrystals.^{6, 27} Additionally, we did not use 1-octadecene (ODE), a commonly used solvent in the synthesis of colloidal NCs. It should also be noted that we did not use ODE in the synthesis of FA-oleate and GA-oleate. Recently, Dhaene et al. have demonstrated that ODE can polymerize to poly(1-octadecene) at temperatures ranging from 120 °C to 320 °C.⁴⁸ Poly(1-octadecene) impurities cannot be separated from the NC product by using the commonly used separation techniques such as size exclusion chromatography or precipitation dispersion cycles. Noteworthily, chemical residues or reaction side-products in NC colloids are a significant detriment to nanocrystal-based optoelectronic device applications.⁴⁸ Therefore, our synthetic route produces NCs that are poly(1-octadecene) and polar solvent free. In order to colloiddally synthesize the NCs, the following main steps have been followed. We firstly dissolved 0.2 mmol PbI_2 in 200 μ L of oleic acid (OA) and 250 μ L of 0.4 M OLAM-I solution at elevated temperature. After complete dissolution of the PbI_2 , the prepared solution was diluted with hexane at 60 °C. GA-oleate was synthesized by reacting guanidinium carbonate with oleic acid in an inert atmosphere at an elevated temperature. Subsequently, the prepared GA-oleate was diluted with the proper amount of toluene and subsequently cooled down to room temperature.

FA-oleate was synthesized by using the same synthetic route with the GA-oleate synthesis. In order to synthesize $L_2[GA_xFA_{1-x}PbI_3]PbI_4$ NPLs, 25 μ L of PbI_2 precursor solution was injected into 5 mL of hexane. Subsequently, GA-oleate, FA-oleate or mixture of GA-oleate and FA oleate were injected into the reaction mixture. In fact, the crystallization of $L_2[GA_xFA_{1-x}PbI_3]PbI_4$ NCs spontaneously occurs in around five minutes.

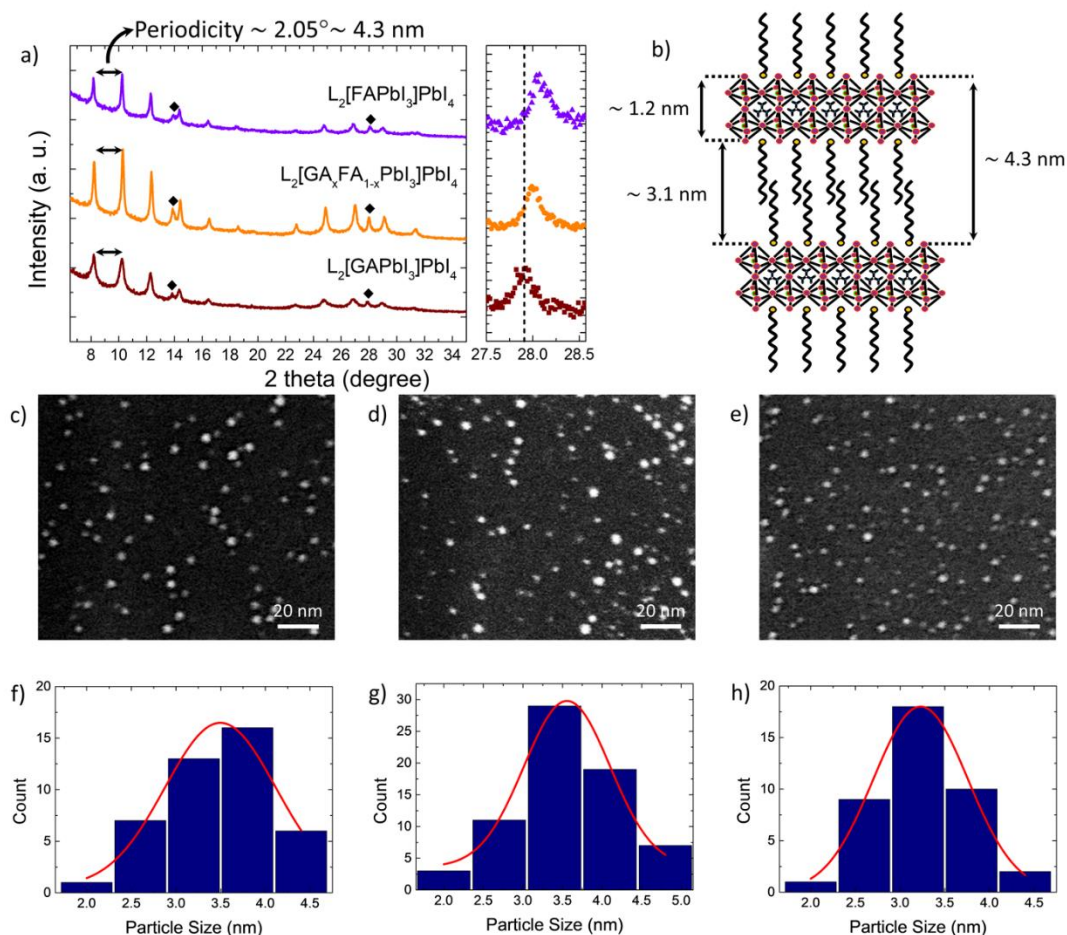


Figure 2.2. Structural characterization of NCs. (a) Powder XRD patterns of $L_2[GAPbI_3]PbI_4$, $L_2[GA_{0.5}FA_{0.5}PbI_3]PbI_4$, and $L_2[FAPbI_3]PbI_4$ NCs. (b) Schematic presentation of the stacking multiple NCs. Average thickness of the LHP unit cell and distance between LHP layers were shown. HAADF images of (c) $L_2[GAPbI_3]PbI_4$, (d) $L_2[GA_{0.5}FA_{0.5}PbI_3]PbI_4$, and (e) $L_2[FAPbI_3]PbI_4$ NCs. Particle size distributions of (f) $L_2[GAPbI_3]PbI_4$, (g) $L_2[GA_{0.5}FA_{0.5}PbI_3]PbI_4$, and (h) $L_2[FAPbI_3]PbI_4$ NCs.

Figure 2.2a demonstrates the obtained powder XRD patterns of $L_2[GAPbI_3]PbI_4$, $L_2[FAPbI_3]PbI_4$ and, alloyed $L_2[GA_{0.5}FA_{0.5}PbI_3]PbI_4$ NCs. Diffraction peaks at around 14° and 28° correspond to the (100) and (200) planes in the cubic perovskite lattice, respectively.⁴⁹ Furthermore, as the FA amount in the $L_2[GA_xFA_{x-1}PbI_3]PbI_4$ solid solution increases, the peak corresponding to the (200) plane shifts to higher angles. Note the ionic radii of FA and GA cations are 253 pm and 279 pm, respectively.^{27, 28} Increasing FA amount in the $L_2[GA_xFA_{x-1}PbI_3]PbI_4$ solid solution decreases the lattice parameters of the perovskite unit cell due to the smaller ionic radius of FA cation. Therefore, the designated XRD peaks shift to higher angles. On the other hand, repeating parallel peaks of around 2.05° in the diffraction pattern indicates the formation of the NC superstructure in the drop-cast films.^{46, 50, 51}

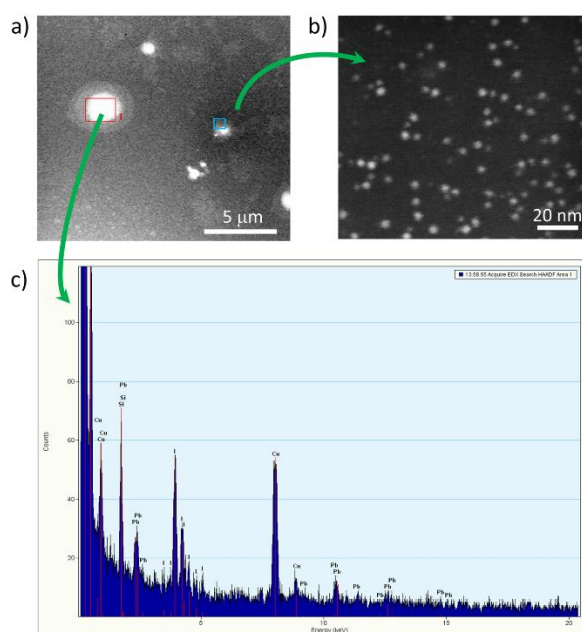


Figure 2.3. (a) Large area HAADF image of $L_2[GAPbI_3]PbI_4$ NCs. (b) High magnification HAADF image of the same sample. (c) Energy dispersive spectroscopy (EDS) area scan analysis of NCs which demonstrates $L_2[GAPbI_3]PbI_4$ NCs contain Pb and I atoms.

Schematic illustration of the stacked NCs was shown in Figure 2.2b. The center-to-center distance of the nanocrystals is close to 4.3 nm in the superstructure. The average thickness of a single PbI_6 octahedral layer is 0.6 nm.^{6, 46, 50, 51} A single oleylamine molecule on the NC surface has an average thickness of 2 nm.⁵² As a result, the average thickness of the oleylamine bilayers between NCs was calculated to be 3.1 nm, which is

very close to the previously shown oleylamine bilayer thickness.⁵⁰⁻⁵² In Figures 2.2c-e, HAADF images of $L_2[\text{GAPbI}_3]\text{PbI}_4$, $L_2[\text{GA}_{0.5}\text{FA}_{0.5}\text{PbI}_3]\text{PbI}_4$, and $L_2[\text{FAPbI}_3]\text{PbI}_4$ NCs were shown. Particle size distributions of $L_2[\text{GAPbI}_3]\text{PbI}_4$, $L_2[\text{GA}_{0.5}\text{FA}_{0.5}\text{PbI}_3]\text{PbI}_4$, and $L_2[\text{FAPbI}_3]\text{PbI}_4$ NCs are shown in the Figure 2.2f-h, respectively and they are very close to each other, around 3.5 nm. In our previous work, we demonstrated that the size of the PbI_2 seeds used in the seed mediated synthesis is around 3 nm.⁴³ In fact, the size of the LHP products obtained in this study is very close to the size of the seeds shown in our previous study. Additionally, the size of the synthesized particles is very close to the size of the particles previously reported RP MAPbI_3 NCs by Hassan et al.⁵³

Also, energy dispersive spectroscopy (EDS) area scan analysis demonstrates NCs contain Pb and I atoms (see Figure 2.3).

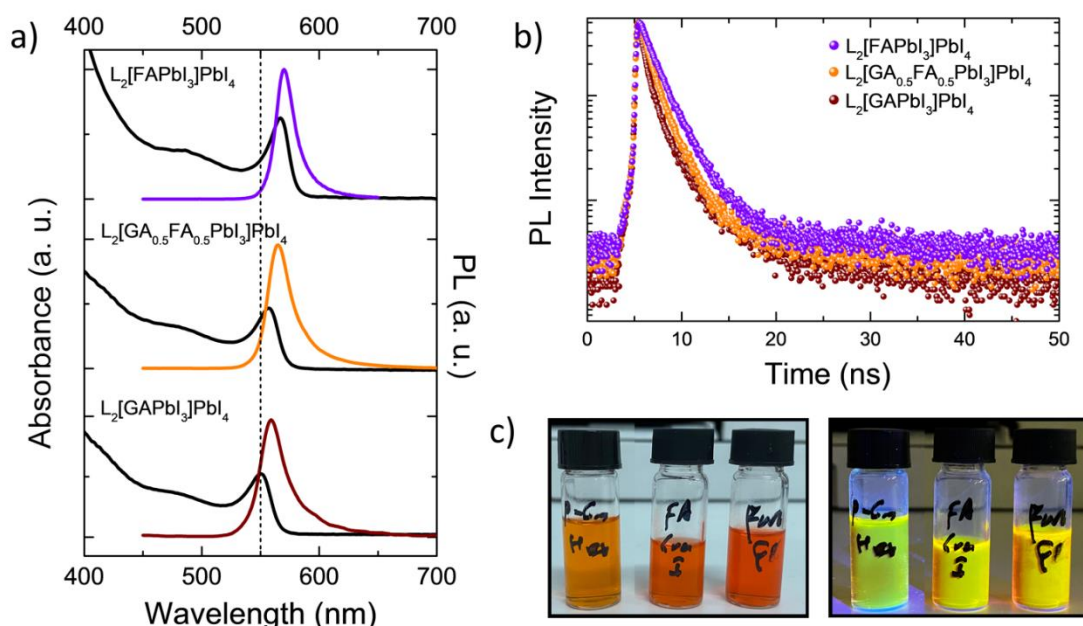


Figure 2.4. Optical properties of NCs. (a) Absorption and photoluminescence (PL) spectra of $L_2[\text{GAPbI}_3]\text{PbI}_4$, $L_2[\text{GA}_{0.5}\text{FA}_{0.5}\text{PbI}_3]\text{PbI}_4$, and $L_2[\text{FAPbI}_3]\text{PbI}_4$ NCs. (b) PL lifetime decays of the colloid samples and their photographs were taken under day light (left) and under illumination of 365 nm UV light (right). (c) From left-hand side to right-hand side, $L_2[\text{GAPbI}_3]\text{PbI}_4$, $L_2[\text{GA}_{0.5}\text{FA}_{0.5}\text{PbI}_3]\text{PbI}_4$, and $L_2[\text{FAPbI}_3]\text{PbI}_4$ NC colloids are placed, respectively.

Furthermore, optical properties of the 2D RP $L_2[\text{GA}_x\text{FA}_{1-x}\text{PbI}_3]\text{PbI}_4$ ($0 \leq x \leq 1$) NCs were characterized. All samples have excitonic peak due to the quantum well structure of layered perovskites.⁵⁴ With increasing FA amount, the absorbance peaks of

2D RP NCs red shift slightly. In addition, the PL peaks follow the same trend as the absorbance spectra (Figure 2.4a). A recent study demonstrates that the A-site cation size and band gap of the 2D LHPs are parabolically related.²⁷ For example, in $L_2[APbI_3]PbI_4$ NCs, the band gap energy decreases with increasing cation size, Cs (188 pm) to MA (217 pm) and further FA (253 pm).⁶ Conversely, the band gap of the $L_2[APbI_3]PbI_4$ NCs increases with increasing cations size from FA (253 pm) to GA (279 pm).²⁸ The size of the A-site cation stretches or tilts the perovskite lattice. Negative chemical pressure is indeed created in the lattice by small A-site cations such as Cs. Large A-site cations, on the other hand, such as GA, EA, and DMA cause positive chemical pressure in the lattice. Blue shifts in the absorbance and PL spectra are caused by large positive or negative chemical pressures on the perovskite lattice.²⁷ More precisely, the stretching of the Pb-I bonds reduces the amount of Pb 6s and I 5p antibonding combinations, causing the valence band to destabilize and thus increase the band gap energy.⁵⁵⁻⁵⁷ Photographs of the colloids under day light and 365 nm UV light illumination were demonstrated in Figure 2.4c. The band gap energy decreases as the FA amount increases. As a result, the color of the samples become more reddish in the daylight, and the emission of the samples change from greenish yellow to orange when illuminated with the UV light. Furthermore, the PL peaks for $L_2[GAPbI_3]PbI_4$, $L_2[GA_{0.5}FA_{0.5}PbI_3]PbI_4$, and $L_2[FAPbI_3]PbI_4$ NCs have a full width at half maxima (FWHM) of 71 meV, 91 meV, and 102 meV, respectively. The increase in FWHM of the NCs implies that; large GA cation increases exciton phonon coupling and causes broadening in the PL peaks.^{14, 58}

Table 2.1. Time-resolved photoluminescence lifetime profiles for $L_2[GA_xFA_{1-x}PbI_3]PbI_4$ NCs, which are fitted with a biexponential function.

Sample	τ_1 (ns)	τ_2 (ns)	A_1 (%)	A_2 (%)
$L_2[GAPbI_3]_2PbI_4$	0.78	3.35	58.43	41.57
$L_2[GA_{0.5}FA_{0.5}PbI_3]PbI_4$	1.30	3.96	76.98	23.02
$L_2[FAPbI_3]_2PbI_4$	1.88	5.43	87.70	12.30

Further, time-resolved photoluminescence measurements were performed for all the samples and shown in Figure 2.4b. PL lifetime decays were fitted with the biexponential function (See Table S2.1). Both slow and fast lifetime components of the samples decreased as the amount of GA in the solid solutions increases. It should be noted

here that halide perovskites with a larger band gap, a smaller nanocrystal size, or a lighter halide have faster charge carrier dynamics.⁵⁹ Furthermore, due to the large GA cation in the perovskite structure, lattice distortions and strains may increase the defect density of the NCs. As a result, higher defect concentrations in the perovskite NCs can reduce carrier lifetimes. Surface defects on the NCs have a significant impact on the carrier dynamics.⁶⁰

The application of perovskite nanocrystals into optoelectronic devices such as light emitting diodes, lasers, and solar cells require high stability (against light, heat, and humidity, etc.) and high PLQY of the NCs. Figure 5a and 4b show the PLQY versus FA content and stability of $L_2[GA_xFA_{1-x}PbI_3]PbI_4$ colloidal NCs under ambient conditions, respectively. The measured PLQY values and stabilities for $L_2[GAPbI_3]PbI_4$, $L_2[GA_{0.5}FA_{0.5}PbI_3]PbI_4$, and $L_2[FAPbI_3]PbI_4$ NCs are 0.9 % and 5 days, 6.5 % and 3 days, and 12.6 % and 2 days, respectively. Furthermore, as shown in Figure 2.5c, drop-cast films of $L_2[GAPbI_3]PbI_4$, $L_2[GA_{0.5}FA_{0.5}PbI_3]PbI_4$ NCs are stable at ambient conditions for at least ten days.

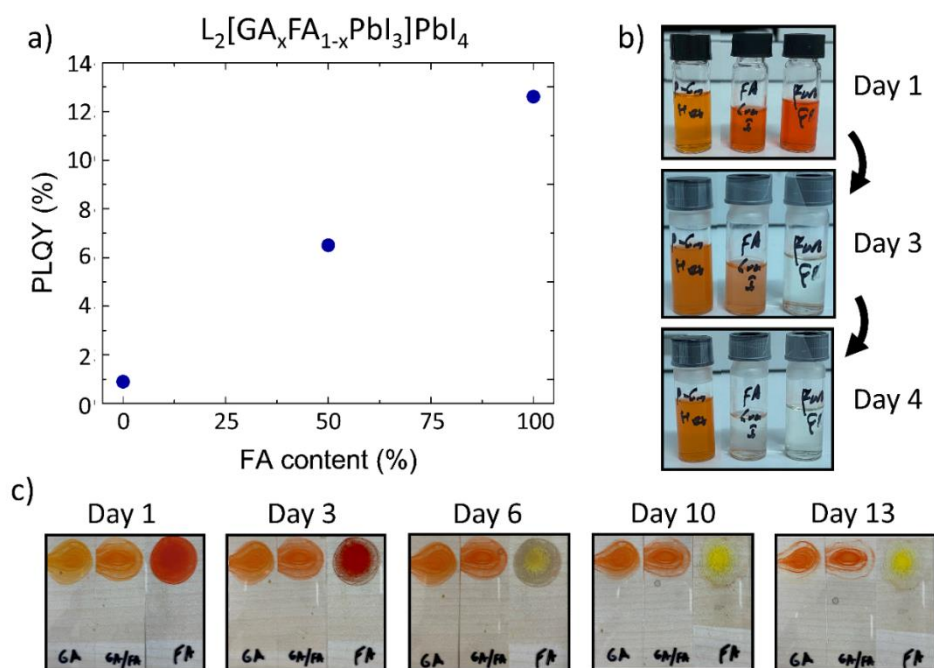


Figure 2.5. (a) PLQY versus FA content graph of $L_2[GA_xFA_{1-x}PbI_3]PbI_4$ NCs. (b, c) Time-dependent degradation of colloids and drop-cast films, respectively. The left-hand side to the right-hand side in the photographs are $L_2[GAPbI_3]PbI_4$, $L_2[GA_{0.5}FA_{0.5}PbI_3]PbI_4$, and $L_2[FAPbI_3]PbI_4$ NCs, respectively.

Similarly, in our work, $L_2[\text{GAPbI}_3]\text{PbI}_4$ NCs have the highest stability at ambient conditions. Additionally, in the previous study, GA doped FAPbBr_3 LHP NC LEDs showed improved device stability and optical properties than FAPbBr_3 LHP NC LEDs. For 3D LPH, low concentrations of GA can dissolve in the parent FAPbBr_3 phase until 12.5% due to the entropy stabilization. On the other hand, high GA concentration further increases the enthalpy and destabilize the 3D perovskite structure.⁴² Note 2D RP perovskite structures have unique strain accumulation mitigation and strain balancing properties, making them more flexible than 3D perovskite structures.²⁸ As a result, large A-site cations can be alloyed or substituted at all concentrations in 2D RP perovskites. Moreover, hydrogen bonds are crucial for the lattice stabilization of LHP. The higher number of hydrogen bonds in the LHP structure possibly further stabilize the LHP structure.^{37, 61} Therefore, we believe that a higher number of hydrogen bonds due to the GA cations in the NCs increases, the stability of the $L_2[\text{GAPbI}_3]\text{PbI}_4$, $L_2[\text{GA}_{0.5}\text{FA}_{0.5}\text{PbI}_3]\text{PbI}_4$ NCs demonstrated in this work.

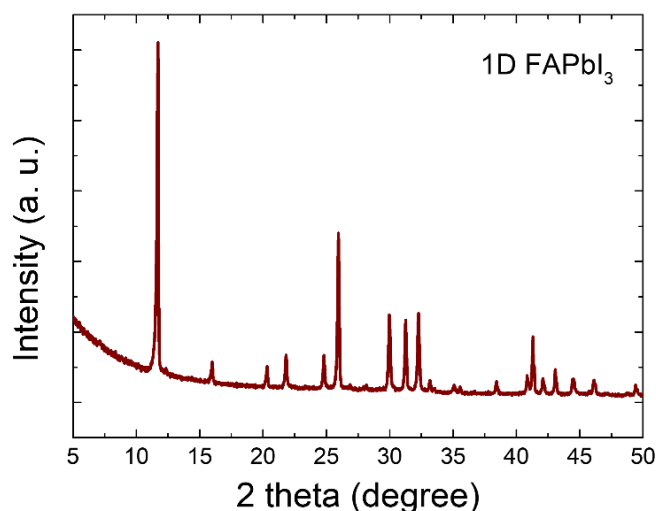


Figure 2.6. XRD pattern of 1D FAPbI_3 NCs. 1D hexagonal ($P6_3mc$) phase of FAPbI_3 was obtained after 6 days.

Finally, we would like to tune the band gap of NCs by halide exchange reactions. We apply halide exchange reaction in $L_2[\text{GAPbI}_3]\text{PbI}_4$, $L_2[\text{GA}_{0.5}\text{FA}_{0.5}\text{PbI}_3]\text{PbI}_4$, and $L_2[\text{FAPbI}_3]\text{PbI}_4$ NCs via bromide ion addition (Figure 5). Noteworthy, in organo-lead iodide perovskites, after the addition of bromide ions into the iodide host lattice, valence band composition changes from 5p to 4p.^{62, 63} Therefore, the band gap of NCs increases with bromide ion addition to the colloid. Absorption peaks shift to shorter wavelengths

with additional bromide ion, as shown in Figures 2.7a, 2.7e, and 2.7i. It should be noted that halide ion miscibility decreases with increasing thickness, particularly for $n = 1, 2$ RP phases.^{64, 65} For all A-site compositions, the halide exchange reaction works within a narrow range of the visible spectrum. This limited range could be attributed to $n = 2$ RP perovskites' decreased halide miscibility. Furthermore, the addition of bromide ions reduced the PL of the NCs for all A-site compositions (Figures 2.7c, 2.7g, 2.7k). $L_2[\text{GAPbI}_3]\text{PbI}_4$, $L_2[\text{GA}_{0.5}\text{FA}_{0.5}\text{PbI}_3]\text{PbI}_4$, and $L_2[\text{FAPbI}_3]\text{PbI}_4$ NCs emissions can be tuned from 532 nm to 559 nm, 525 nm to 566 nm, and 500 nm to 574 nm, respectively, without completely quenching the PL (Figure 7b, 7f, 7j). the reason of reduction in PL with addition bromide for all A-site compositions can be size mismatch between Br and I ions can affect lattice and surface defect of the crystals and causes trap states.⁶⁶ It is clear that increasing the GA concentration in the colloid reduces PL tunability of the nanocrystals. Reduction in the tunability range of PL in GA cation presence, may indicate already strained perovskite lattice by GA cation further distorted by the bromide ions.²⁷

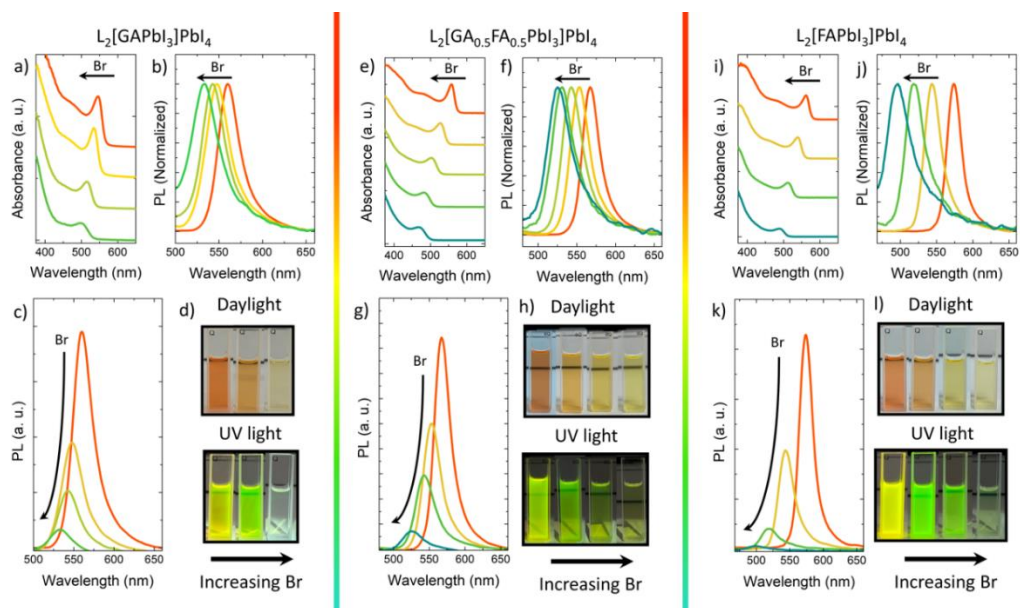


Figure 2.7. Halide exchange reaction of $L_2[\text{GAPbI}_3]\text{PbI}_4$, $L_2[\text{GA}_{0.5}\text{FA}_{0.5}\text{PbI}_3]\text{PbI}_4$, and $L_2[\text{FAPbI}_3]\text{PbI}_4$ NCs via bromide addition. Absorption spectra and normalized PL spectra of $L_2[\text{GAPbI}_3]\text{PbI}_4$ (a, b), $L_2[\text{GA}_{0.5}\text{FA}_{0.5}\text{PbI}_3]\text{PbI}_4$ (e, f), and $L_2[\text{FAPbI}_3]\text{PbI}_4$ (i, j) NCs, and their corresponding photographs under day light and UV light illumination (d, h, l). Bromide amount in the colloids increases from left-hand side to the right-hand side in the photographs. Bromide mediated PL quenching of $L_2[\text{GAPbI}_3]\text{PbI}_4$, $L_2[\text{GA}_{0.5}\text{FA}_{0.5}\text{PbI}_3]\text{PbI}_4$, and $L_2[\text{FAPbI}_3]\text{PbI}_4$ NCs (c, g, k).

2.3. Conclusion

The synthesis of stable and pure colloidal perovskite NCs is crucial for applications in LEDs, photovoltaics, lasers, and photodetectors. It is well known that residual polar solvents severely decrease the stability of perovskite NPLs.^{8,43} On the other hand synthesis by products and residuals decreases device performance of NC based applications.^{48,6748} Herein, for the first time, we demonstrate room temperature colloidal synthesis of $L_2[GA_xFA_{1-x}PbI_3]PbI_4$ NCs without using any polar and high boiling point non-polar solvent (ODE free). Additionally, we show that by alloying GA and FA cations in $L_2[GA_xFA_{1-x}PbI_3]PbI_4$ NCs, the stability and PLQY of the colloidal nanocrystals can be effectively tuned. Importantly, the highest PLQY of 12.6 % was measured in $L_2[FAPbI_3]PbI_4$ NPLs. To the best of our knowledge, the PLQY of the $L_2[FAPbI_3]PbI_4$ NCs synthesized in this study is at least three times higher than the previously reported values.^{6,27} $L_2[GAPbI_3]PbI_4$ and $L_2[GA_{0.5}FA_{0.5}PbI_3]PbI_4$ NCs shows increased ambient stability than $L_2[FAPbI_3]PbI_4$ NCs. However, $L_2[GAPbI_3]PbI_4$ and $L_2[GA_{0.5}FA_{0.5}PbI_3]PbI_4$ NCs have lower PLQY than $L_2[FAPbI_3]PbI_4$ NCs. Time resolved photoluminescence measurements show that the charge carrier dynamics in $L_2[GA_xFA_{1-x}PbI_3]PbI_4$ NCs become faster as the GA amount increases which is consistent with reduced PLQY values with increasing GA amount. More importantly, we investigated halide exchange reactions in $L_2[GA_xFA_{1-x}PbI_3]PbI_4$ NCs. Due to the reduced miscibility of the halide ions in RP perovskites, the halide exchange reaction can only be used in a limited range in the visible spectrum. Furthermore, increasing the amount of GA in the solid solution reduced the tunability of photoluminescence emission of NCs via halide exchange reaction. Owing the large GA cations and the small bromide anions, the lattice distortions in the NCs increased. We envision that the $L_2[GA_xFA_{1-x}PbI_3]PbI_4$ NCs shown in this study can be used in various optoelectronic applications such as light-emitting diodes and solar cells due to their prolonged stability, and increased PLQYs.

2.4. Experimental Section

2.4.1. Chemicals

Lead (II) iodide (PbI_2 , 99%), Lead(II) Bromide (PbBr_2 , $\geq 98\%$) Cesium carbonate (Cs_2CO_3 , 99.9%), Formamidine acetate salt (FA-acetate, $\text{HN}=\text{CHNH}_2 \cdot \text{CH}_3\text{COOH}$, 99.9%), guanidine carbonate salt (GA-carbonate, $\text{NH}_2\text{C}(=\text{NH})\text{NH}_2 \cdot \frac{1}{2}\text{H}_2\text{CO}_3$) 1-octadecene (ODE, 90%), oleylamine (OLAM, 70%), hydroiodic acid (HI, $\geq 57\%$ in water), oleic acid (OA, 90%) and Hexane (EMPLURA®) were all purchased from Sigma-Aldrich and used without any further purification.

2.4.2. Synthesis of OLAM-I

20 mL of OLAM and 1.10 mL of HI were loaded in a 100 mL three neck round bottomed flask. The mixture was heated to 130 °C for 2 hours under the flow of nitrogen. Subsequently, the reaction was cooled down to room temperature and transferred to a vial for further use.

2.4.3. Synthesis of FA-oleate

265 mg of FA-acetate or 230 mg GA-carbonate, and 2 mL of OA were mixed in a round bottom flask. The mixture was degassed at room temperature for 10 min, and then further degassed for 10 min at 100 °C. Temperature of the reaction vessel was set to 125 °C under the flow of nitrogen gas and kept at the same temperature until a clear solution was obtained. Afterwards, 8 mL of toluene was quickly injected into the reaction flask and the reaction mixture was cooled down to room temperature.

2.4.4. Synthesis of GA-oleate

230 mg of GA-carbonate, and 2 mL of OA were all mixed in a round bottom flask. The mixture was degassed at room temperature for 10 min and further degassed for 30 min at 100 °C. Temperature of the reaction vessel was set to 125 °C under the nitrogen atmosphere and the reaction mixture was kept at 125 °C until a clear solution was

obtained. Subsequently, 8 mL of toluene was injected into the reaction flask and then the flask was cooled down to room temperature.

2.4.5. Synthesis of PbI₂ Seeds

0.2 mmol PbI₂, 250 μL of OLAM-I, and 200 μL of OA were loaded in a glass tube and degassed at 80 °C and subsequently, heated to 140 °C under vigorous stirring until all PbI₂ solution became completely clear. Then, the solution was cooled down to 60 °C and 2 mL of hexane was added into the reaction mixture. In addition, the precursor solution was cooled down to room temperature and stored for further use.

2.4.6. Synthesis of PbBr₂ Seeds

0.2 mmol PbBr₂ salt, 200 μL of OLAM, and 200 μL of OA were loaded in a glass tube and degassed at 80 °C and subsequently, heated to 150 °C until the solution became completely clear. Then, the solution was cooled to 60 °C and 2 mL hexane was added. Further, precursor solution was cooled to room temperature and stored for further use.

2.4.7. L₂[GA_xFA_{1-x}PbI₃]PbI₄ NC Synthesis

1 μL of desired ratios of GA-oleate and FA-oleate was injected into 5 mL of hexane, and then 25 μL of PbI₂ NC seed solution was added into the reaction solution. The solution was inversion mixed, and the reaction was completed in around 5 minutes. Synthesis can be scaled up using the same precursor and solvent ratios. NCs were isolated by centrifuging at 15000 rpm for 40 min. and redispersion in hexane. On the other hand, dense NC colloids of L₂[FAPbI₃]PbI₄ and L₂[GA_{0.5}FA_{0.5}PbI₃]PbI₄ NCs can be synthesized by 50 μL PbI₂ solution with 4 μL FA-oleate or 2 μL FA-oleate and 2 μL GA-oleate mixture and centrifuged at 15000 rpm for 10 minutes. However, dense L₂[GAPbI₃]PbI₄ NC colloids could not be synthesized by mixing 50 μL PbI₂ and 4μL GA-oleate.

2.4.8. Halide Exchange Reactions

The mixed halide NCs were prepared by adding 3 μL of PbBr_2 seeds to 2 mL of NPL solution. After the halide exchange reaction was completed within 2 min, absorption and PL spectra of the colloid were acquired.

2.4.9. Characterization of NCs

Transmission electron microscopy (TEM) analysis of NCs were carried out in order to observe morphology of the nanocrystals (TEM, JEOL-2100F, Japan). The samples were prepared by drop-casting diluted NC suspensions onto 200 mesh carbon-coated copper grids. Absorption (Abs), Photoluminescence (PL), and time-resolved lifetime (LT) measurements were carried out by using a FS5 Spectrofluorometer (Edinburgh Instruments, UK). For PLQY, a Xenon lamp was employed with an excitation wavelength of 350 nm. PLQY of each sample was measured by utilizing an integrating sphere. Samples were diluted in hexane and the optical properties of the nanocrystals were measured in a cylindrical quartz cuvette. In LT measurements, the samples were excited by using a 350 nm laser with a pulse width of 100 ps and a repetition rate of 1 MHz. All of the characterization measurements were performed at room temperature.

2.5. References

1. Papavassiliou, G. C., Three- and low-dimensional inorganic semiconductors. *Prog. Solid State Chem.* **1997**, 25 (3-4), 125-270.
2. Papavassiliou, G. C.; Koutselas, I., Structural, optical and related properties of some natural three- and lower-dimensional semiconductor systems. *Synth. Met.* **1995**, 71 (1-3), 1713-1714.
3. Kamminga, M. E.; Fang, H.-H.; Filip, M. R.; Giustino, F.; Baas, J.; Blake, G. R.; Loi, M. A.; Palstra, T. T. M., Confinement Effects in Low-Dimensional Lead Iodide Perovskite Hybrids. *Chem. Mater.* **2016**, 28 (13), 4554-4562.
4. Ishihara, T.; Takahashi, J.; Goto, T., Optical properties due to electronic transitions in two-dimensional semiconductors $(\text{C}_n\text{H}_{2n+1}\text{NH}_3)_2\text{PbI}_4$. *Physical review B* **1990**, 42 (17), 11099.

5. Tyagi, P.; Arveson, S. M.; Tisdale, W. A., Colloidal organohalide perovskite nanoplatelets exhibiting quantum confinement. *The journal of physical chemistry letters* **2015**, *6* (10), 1911-1916.
6. Weidman, M. C.; Seitz, M.; Stranks, S. D.; Tisdale, W. A., Highly tunable colloidal perovskite nanoplatelets through variable cation, metal, and halide composition. *Acs Nano* **2016**, *10* (8), 7830-7839.
7. Sichert, J. A.; Tong, Y.; Mutz, N.; Vollmer, M.; Fischer, S.; Milowska, K. Z.; García Cortadella, R.; Nickel, B.; Cardenas-Daw, C.; Stolarczyk, J. K., Quantum size effect in organometal halide perovskite nanoplatelets. *Nano Lett.* **2015**, *15* (10), 6521-6527.
8. Huang, H.; Li, Y.; Tong, Y.; Yao, E. P.; Feil, M. W.; Richter, A. F.; Döblinger, M.; Rogach, A. L.; Feldmann, J.; Polavarapu, L., Spontaneous Crystallization of Perovskite Nanocrystals in Nonpolar Organic Solvents: A Versatile Approach for their Shape-Controlled Synthesis. *Angewandte Chemie International Edition* **2019**, *58* (46), 16558-16562.
9. Bekenstein, Y.; Koscher, B. A.; Eaton, S. W.; Yang, P.; Alivisatos, A. P., Highly Luminescent Colloidal Nanoplates of Perovskite Cesium Lead Halide and Their Oriented Assemblies. *Journal of the American Chemical Society* **2015**, *137* (51), 16008-16011.
10. Protesescu, L.; Yakunin, S.; Kumar, S.; Bar, J.; Bertolotti, F.; Masciocchi, N.; Guagliardi, A.; Grotevent, M.; Shorubalko, I.; Bodnarchuk, M. I.; Shih, C. J.; Kovalenko, M. V., Dismantling the "Red Wall" of Colloidal Perovskites: Highly Luminescent Formamidinium and Formamidinium-Cesium Lead Iodide Nanocrystals. *ACS Nano* **2017**, *11* (3), 3119-3134.
11. Schmidt, L. C.; Pertegás, A.; González-Carrero, S.; Malinkiewicz, O.; Agouram, S.; Minguez Espallargas, G.; Bolink, H. J.; Galian, R. E.; Pérez-Prieto, J., Nontemplate synthesis of CH₃NH₃PbBr₃ perovskite nanoparticles. *Journal of the American Chemical Society* **2014**, *136* (3), 850-853.
12. Zheng, X.; Hou, Y.; Sun, H.-T.; Mohammed, O. F.; Sargent, E. H.; Bakr, O. M., Reducing Defects in Halide Perovskite Nanocrystals for Light-Emitting Applications. *The Journal of Physical Chemistry Letters* **2019**, *10* (10), 2629-2640.

13. Guvenc, C. M.; Polat, N.; Balci, S., Strong plasmon–exciton coupling in colloidal halide perovskite nanocrystals near a metal film. *Journal of Materials Chemistry C* **2020**, *8* (46), 16520-16526.
14. Blancon, J.-C.; Even, J.; Stoumpos, C. C.; Kanatzidis, M. G.; Mohite, A. D., Semiconductor physics of organic–inorganic 2D halide perovskites. *Nature Nanotechnology* **2020**, *15* (12), 969-985.
15. Weidman, M. C.; Goodman, A. J.; Tisdale, W. A., Colloidal halide perovskite nanoplatelets: an exciting new class of semiconductor nanomaterials. *Chem. Mater.* **2017**, *29* (12), 5019-5030.
16. Xu, L.-J.; Worku, M.; He, Q.; Ma, B., Advances in light-emitting metal-halide perovskite nanocrystals. *MRS Bull.* **2020**, *45* (6), 458-466.
17. Luo, D.; Wang, L.; Qiu, Y.; Huang, R.; Liu, B., Emergence of Impurity-Doped Nanocrystal Light-Emitting Diodes. *Nanomaterials* **2020**, *10* (6), 1226.
18. Tsai, H.; Nie, W.; Blancon, J. C.; Stoumpos, C. C.; Asadpour, R.; Harutyunyan, B.; Neukirch, A. J.; Verduzco, R.; Crochet, J. J.; Tretiak, S.; Pedesseau, L.; Even, J.; Alam, M. A.; Gupta, G.; Lou, J.; Ajayan, P. M.; Bedzyk, M. J.; Kanatzidis, M. G., High-efficiency two-dimensional Ruddlesden-Popper perovskite solar cells. *Nature* **2016**, *536* (7616), 312-6.
19. Otero-Martínez, C.; Ye, J.; Sung, J.; Pastoriza-Santos, I.; Pérez-Juste, J.; Xia, Z.; Rao, A.; Hoye, R. L.; Polavarapu, L., Colloidal Metal-Halide Perovskite Nanoplatelets: Thickness-Controlled Synthesis, Properties and Application in Light-Emitting Diodes. *Adv. Mater.* **2021**, 2107105.
20. Vashishtha, P.; Ng, M.; Shivarudraiah, S. B.; Halpert, J. E., High Efficiency Blue and Green Light-Emitting Diodes Using Ruddlesden–Popper Inorganic Mixed Halide Perovskites with Butylammonium Interlayers. *Chem. Mater.* **2018**, *31* (1), 83-89.
21. Goldschmidt, V. M., Die gesetze der krystallochemie. *Naturwissenschaften* **1926**, *14* (21), 477-485.
22. Maculan, G.; Sheikh, A. D.; Abdelhady, A. L.; Saidaminov, M. I.; Haque, M. A.; Murali, B.; Alarousu, E.; Mohammed, O. F.; Wu, T.; Bakr, O. M., CH₃NH₃PbCl₃ Single Crystals: Inverse Temperature Crystallization and Visible-Blind UV-Photodetector. *The Journal of Physical Chemistry Letters* **2015**, *6* (19), 3781-3786.

23. Saidaminov, M. I.; Abdelhady, A. L.; Murali, B.; Alarousu, E.; Burlakov, V. M.; Peng, W.; Dursun, I.; Wang, L.; He, Y.; Maculan, G.; Goriely, A.; Wu, T.; Mohammed, O. F.; Bakr, O. M., High-quality bulk hybrid perovskite single crystals within minutes by inverse temperature crystallization. *Nature Communications* **2015**, *6* (1).
24. Travis, W.; Glover, E. N. K.; Bronstein, H.; Scanlon, D. O.; Palgrave, R. G., On the application of the tolerance factor to inorganic and hybrid halide perovskites: a revised system. *Chemical Science* **2016**, *7* (7), 4548-4556.
25. Saidaminov, M. I.; Abdelhady, A. L.; Maculan, G.; Bakr, O. M., Retrograde solubility of formamidinium and methylammonium lead halide perovskites enabling rapid single crystal growth. *Chem. Commun.* **2015**, *51* (100), 17658-17661.
26. Jang, D. M.; Kim, D. H.; Park, K.; Park, J.; Lee, J. W.; Song, J. K., Ultrasound synthesis of lead halide perovskite nanocrystals. *Journal of Materials Chemistry C* **2016**, *4* (45), 10625-10629.
27. Hautzinger, M. P.; Pan, D.; Pigg, A. K.; Fu, Y.; Morrow, D. J.; Leng, M.; Kuo, M.-Y.; Spitha, N.; Lafayette, D. P.; Kohler, D. D.; Wright, J. C.; Jin, S., Band Edge Tuning of Two-Dimensional Ruddlesden–Popper Perovskites by A Cation Size Revealed through Nanoplates. *ACS Energy Letters* **2020**, *5* (5), 1430-1437.
28. Fu, Y.; Hautzinger, M. P.; Luo, Z.; Wang, F.; Pan, D.; Aristov, M. M.; Guzei, I. A.; Pan, A.; Zhu, X.; Jin, S., Incorporating Large A Cations into Lead Iodide Perovskite Cages: Relaxed Goldschmidt Tolerance Factor and Impact on Exciton–Phonon Interaction. *ACS Central Science* **2019**, *5* (8), 1377-1386.
29. Dutta, A.; Pradhan, N., Phase-stable red-emitting CsPbI₃ nanocrystals: successes and challenges. *ACS Energy Letters* **2019**, *4* (3), 709-719.
30. Guvenc, C. M.; Yalcinkaya, Y.; Ozen, S.; Sahin, H.; Demir, M. M., Gd³⁺-Doped α -CsPbI₃ Nanocrystals with Better Phase Stability and Optical Properties. *The Journal of Physical Chemistry C* **2019**, *123* (40), 24865-24872.
31. Steele, J. A.; Prakasam, V.; Huang, H.; Solano, E.; Chernyshov, D.; Hofkens, J.; Roeffaers, M. B. J., Trojans That Flip the Black Phase: Impurity-Driven Stabilization and Spontaneous Strain Suppression in gamma-CsPbI₃ Perovskite. *J. Am. Chem. Soc.* **2021**, *143* (28), 10500-10508.
32. Ma, J.-P.; Chen, J.-K.; Yin, J.; Zhang, B.-B.; Zhao, Q.; Kuroiwa, Y.; Moriyoshi, C.; Hu, L.; Bakr, O. M.; Mohammed, O. F., Doping induces structural phase

- transitions in all-inorganic lead halide perovskite nanocrystals. *ACS Materials Letters* **2020**, *2* (4), 367-375.
33. Ahmed, G. H.; Yin, J.; Bakr, O. M.; Mohammed, O. F., Near-unity photoluminescence quantum yield in inorganic perovskite nanocrystals by metal-ion doping. *The Journal of chemical physics* **2020**, *152* (2), 020902.
34. Behera, R. K.; Dutta, A.; Ghosh, D.; Bera, S.; Bhattacharyya, S.; Pradhan, N., Doping the Smallest Shannon Radii Transition Metal Ion Ni (II) for Stabilizing α -CsPbI₃ Perovskite Nanocrystals. *The journal of physical chemistry letters* **2019**, *10* (24), 7916-7921.
35. Tang, Y.; Lesage, A.; Schall, P., CsPbI₃ nanocrystal films: towards higher stability and efficiency. *Journal of Materials Chemistry C* **2020**, *8* (48), 17139-17156.
36. Saliba, M.; Matsui, T.; Domanski, K.; Seo, J.-Y.; Ummadisingu, A.; Zakeeruddin, S. M.; Correa-Baena, J.-P.; Tress, W. R.; Abate, A.; Hagfeldt, A., Incorporation of rubidium cations into perovskite solar cells improves photovoltaic performance. *Science* **2016**, *354* (6309), 206-209.
37. Jodlowski, A. D.; Roldán-Carmona, C.; Grancini, G.; Salado, M.; Ralaifarisoa, M.; Ahmad, S.; Koch, N.; Camacho, L.; De Miguel, G.; Nazeeruddin, M. K., Large guanidinium cation mixed with methylammonium in lead iodide perovskites for 19% efficient solar cells. *Nature Energy* **2017**, *2* (12), 972-979.
38. Kubicki, D. J.; Prochowicz, D.; Hofstetter, A.; Sasaki, M.; Yadav, P.; Bi, D.; Pellet, N.; Lewiński, J.; Zakeeruddin, S. M.; Grätzel, M., Formation of Stable mixed guanidinium–methylammonium phases with exceptionally long carrier lifetimes for high-efficiency lead iodide-based perovskite photovoltaics. *Journal of the American Chemical Society* **2018**, *140* (9), 3345-3351.
39. De Marco, N.; Zhou, H.; Chen, Q.; Sun, P.; Liu, Z.; Meng, L.; Yao, E.-P.; Liu, Y.; Schiffer, A.; Yang, Y., Guanidinium: a route to enhanced carrier lifetime and open-circuit voltage in hybrid perovskite solar cells. *Nano Lett.* **2016**, *16* (2), 1009-1016.
40. Stoddard, R. J.; Rajagopal, A.; Palmer, R. L.; Braly, I. L.; Jen, A. K.-Y.; Hillhouse, H. W., Enhancing defect tolerance and phase stability of high-bandgap perovskites via guanidinium alloying. *ACS Energy Letters* **2018**, *3* (6), 1261-1268.

41. Huang, Z.; Chen, B.; Sagar, L. K.; Hou, Y.; Proppe, A.; Kung, H.-T.; Yuan, F.; Johnston, A.; Saidaminov, M. I.; Jung, E. H.; Lu, Z.-H.; Kelley, S. O.; Sargent, E. H., Stable, Bromine-Free, Tetragonal Perovskites with 1.7 eV Bandgaps via A-Site Cation Substitution. *ACS Materials Letters* **2020**, *2* (7), 869-872.
42. Kim, Y.-H.; Kim, S.; Kakekhani, A.; Park, J.; Park, J.; Lee, Y.-H.; Xu, H.; Nagane, S.; Wexler, R. B.; Kim, D.-H.; Jo, S. H.; Martínez-Sarti, L.; Tan, P.; Sadhanala, A.; Park, G.-S.; Kim, Y.-W.; Hu, B.; Bolink, H. J.; Yoo, S.; Friend, R. H.; Rappe, A. M.; Lee, T.-W., Comprehensive defect suppression in perovskite nanocrystals for high-efficiency light-emitting diodes. *Nature Photonics* **2021**, *15* (2), 148-155.
43. Guvenc, C. M.; Balci, S., Seed-Mediated Synthesis of Colloidal 2D Halide Perovskite Nanoplatelets. *ChemNanoMat* **2021**, *7* (11), 1249-1257.
44. Behera, R. K.; Das Adhikari, S.; Dutta, S. K.; Dutta, A.; Pradhan, N., Blue-Emitting CsPbCl₃ Nanocrystals: Impact of Surface Passivation for Unprecedented Enhancement and Loss of Optical Emission. *The Journal of Physical Chemistry Letters* **2018**, *9* (23), 6884-6891.
45. Wu, Y.; Li, X.; Zeng, H., Highly Luminescent and Stable Halide Perovskite Nanocrystals. *ACS Energy Letters* **2019**, *4* (3), 673-681.
46. Wu, Y.; Wei, C.; Li, X.; Li, Y.; Qiu, S.; Shen, W.; Cai, B.; Sun, Z.; Yang, D.; Deng, Z.; Zeng, H., In Situ Passivation of PbBr₆⁴⁻ Octahedra toward Blue Luminescent CsPbBr₃ Nanoplatelets with Near 100% Absolute Quantum Yield. *ACS Energy Letters* **2018**, *3* (9), 2030-2037.
47. Dutta, A.; Behera, R. K.; Pal, P.; Baitalik, S.; Pradhan, N., Near-Unity Photoluminescence Quantum Efficiency for All CsPbX₃(X=Cl, Br, and I) Perovskite Nanocrystals: A Generic Synthesis Approach. *Angew. Chem. Int. Ed.* **2019**, *58* (17), 5552-5556.
48. Dhaene, E.; Billet, J.; Bennett, E.; Van Driessche, I.; De Roo, J., The Trouble with ODE: Polymerization during Nanocrystal Synthesis. *Nano Lett.* **2019**, *19* (10), 7411-7417.
49. Huang, Y.; Li, L.; Liu, Z.; Jiao, H.; He, Y.; Wang, X.; Zhu, R.; Wang, D.; Sun, J.; Chen, Q.; Zhou, H., The intrinsic properties of FA(1-x)MAxPbI₃ perovskite single crystals. *Journal of Materials Chemistry A* **2017**, *5* (18), 8537-8544.
50. Parobek, D.; Dong, Y.; Qiao, T.; Son, D. H., Direct Hot-Injection Synthesis of Mn-Doped CsPbBr₃ Nanocrystals. *Chem. Mater.* **2018**, *30* (9), 2939-2944.

51. Mehetor, S. K.; Ghosh, H.; Pradhan, N., Acid–Amine Equilibria for Formation and Long-Range Self-Organization of Ultrathin CsPbBr₃ Perovskite Platelets. *The Journal of Physical Chemistry Letters* **2019**, *10* (6), 1300-1305.
52. Borges, J.; Ribeiro, J. A.; Pereira, E. M.; Carreira, C. A.; Pereira, C. M.; Silva, F., Preparation and characterization of DNA films using oleylamine modified Au surfaces. *J. Colloid Interface Sci.* **2011**, *358* (2), 626-634.
53. Hassan, Y.; Song, Y.; Pensack, R. D.; Abdelrahman, A. I.; Kobayashi, Y.; Winnik, M. A.; Scholes, G. D., Structure-Tuned Lead Halide Perovskite Nanocrystals. *Adv. Mater.* **2016**, *28* (3), 566-573.
54. Li, X.; Hoffman, J. M.; Kanatzidis, M. G., The 2D Halide Perovskite Rulebook: How the Spacer Influences Everything from the Structure to Optoelectronic Device Efficiency. *Chem. Rev.* **2021**, *121* (4), 2230-2291.
55. Prasanna, R.; Gold-Parker, A.; Leijtens, T.; Conings, B.; Babayigit, A.; Boyen, H.-G.; Toney, M. F.; McGehee, M. D., Band Gap Tuning via Lattice Contraction and Octahedral Tilting in Perovskite Materials for Photovoltaics. *Journal of the American Chemical Society* **2017**, *139* (32), 11117-11124.
56. Lee, J.-H.; Bristowe, N. C.; Lee, J. H.; Lee, S.-H.; Bristowe, P. D.; Cheetham, A. K.; Jang, H. M., Resolving the Physical Origin of Octahedral Tilting in Halide Perovskites. *Chem. Mater.* **2016**, *28* (12), 4259-4266.
57. Grote, C.; Berger, R. F., Strain Tuning of Tin–Halide and Lead–Halide Perovskites: A First-Principles Atomic and Electronic Structure Study. *The Journal of Physical Chemistry C* **2015**, *119* (40), 22832-22837.
58. Gong, X.; Voznyy, O.; Jain, A.; Liu, W.; Sabatini, R.; Piontkowski, Z.; Walters, G.; Bappi, G.; Nokhrin, S.; Bushuyev, O.; Yuan, M.; Comin, R.; McCamant, D.; Kelley, S. O.; Sargent, E. H., Electron–phonon interaction in efficient perovskite blue emitters. *Nature Materials* **2018**, *17* (6), 550-556.
59. Lignos, I.; Maceiczkyk, R. M.; Kovalenko, M. V.; Stavarakis, S., Tracking the Fluorescence Lifetimes of Cesium Lead Halide Perovskite Nanocrystals During Their Synthesis Using a Fully Automated Optofluidic Platform. *Chem. Mater.* **2019**, *32* (1), 27-37.
60. Dai, J.; Fu, Y.; Manger, L. H.; Rea, M. T.; Hwang, L.; Goldsmith, R. H.; Jin, S., Carrier Decay Properties of Mixed Cation Formamidinium–Methylammonium Lead Iodide Perovskite [HC(NH₂)₂]_{1-x}[CH₃NH₃]_xPbI₃ Nanorods. *The Journal of Physical Chemistry Letters* **2016**, *7* (24), 5036-5043.

61. Lee, J. H.; Lee, J.-H.; Kong, E.-H.; Jang, H. M., The nature of hydrogen-bonding interaction in the prototypic hybrid halide perovskite, tetragonal $\text{CH}_3\text{NH}_3\text{PbI}_3$. *Scientific reports* **2016**, *6* (1), 1-12.
62. Walsh, A., Principles of Chemical Bonding and Band Gap Engineering in Hybrid Organic–Inorganic Halide Perovskites. *The Journal of Physical Chemistry C* **2015**, *119* (11), 5755-5760.
63. Mosconi, E.; Amat, A.; Nazeeruddin, M. K.; Grätzel, M.; De Angelis, F., First-Principles Modeling of Mixed Halide Organometal Perovskites for Photovoltaic Applications. *The Journal of Physical Chemistry C* **2013**, *117* (27), 13902-13913.
64. Roy, C. R.; Pan, D.; Wang, Y.; Hautzinger, M. P.; Zhao, Y.; Wright, J. C.; Zhu, Z.; Jin, S., Anion Exchange of Ruddlesden–Popper Lead Halide Perovskites Produces Stable Lateral Heterostructures. *Journal of the American Chemical Society* **2021**, *143* (13), 5212-5221.
65. Cho, J.; DuBose, J. T.; Le, A. N. T.; Kamat, P. V., Suppressed Halide Ion Migration in 2D Lead Halide Perovskites. *ACS Materials Letters* **2020**, *2* (6), 565-570.
66. Bi, C.; Wang, S.; Wen, W.; Yuan, J.; Cao, G.; Tian, J., Room-Temperature Construction of Mixed-Halide Perovskite Quantum Dots with High Photoluminescence Quantum Yield. *The Journal of Physical Chemistry C* **2018**, *122* (9), 5151-5160.
67. Tisdale, W. A.; Williams, K. J.; Timp, B. A.; Norris, D. J.; Aydil, E. S.; Zhu, X.-Y., Hot-electron transfer from semiconductor nanocrystals. *Science* **2010**, *328* (5985), 1543-1547.

CHAPTER 3

POLAR SOLVENT FREE ROOM TEMPERATURE SYNTHESIS OF CsPbX₃ (X = Br, Cl) PEROVSKITE NANOCUBES

The following chapter is published in *J Mater Chem C Mater* **2023**, *11* (8), 3039–3049.

Abstract

Conventionally, the colloidal lead halide perovskite nanocubes have been synthesized by the hot-injection or ligand-assisted reprecipitation (LARP) methods. We herein demonstrate a polar solvent-free room temperature method for the synthesis of CsPbX₃ (X=Br, Cl) nanocubes. In addition to the commonly used ligand pair of oleylamine and oleic acid, guanidinium (GA) has been used to passivate the surface of the nanocrystals. Our study demonstrates that GA inhibits the formation of low dimensional structures such as nanowires and nanoplatelets and further supports the formation of perovskite nanocubes. In fact, GA diminishes the restricted monomer-addition effect of long-chain oleylammonium (OLAM) ions to the nanocrystal. We show that above a critical GA/OLAM molar ratio, the synthesis yields homogeneous CsPbX₃ (X=Br, Cl) nanocubes. Importantly, we observe the nucleation and growth kinetics of the GA-assisted CsPbBr₃ nanocube formation by using in-situ absorption and photoluminescence (PL) measurements. Small nanocrystals with excitonic absorption peak at around 435 nm and photoluminescence (PL) maxima at 447 nm were nucleated and continuously shifted to longer wavelengths during the growth period. Crucially, our method allows the synthesis of CsPbCl₃ nanocubes at room temperature without using polar organic solvents. The synthesized CsPbBr₃, CsPb(Cl_{0.5}Br_{0.5})₃, CsPbCl₃ nanocubes have PL peaks at 508 nm, 443 nm, and 405 nm, photoluminescence quantum yields (PLQY) of 85%, 58% and 5 %, and lifetimes of 18.98 ns, 18.97 ns, and 14.74 ns, respectively.

3.1. Introduction

Lead halide perovskite nanocrystals have attracted great attention due to their extraordinary optical properties, such as narrow PL line widths, high PLQYs, and tunable band gaps in the visible light spectrum.^{1,2} The hot injection and LARP methods have been commonly used methods to synthesize cesium lead halide perovskite nanocrystals.^{1,3-7} In the hot injection method, lead halide precursor is dissolved by coordinating ligands in a high boiling point nonpolar solvent at an elevated temperature. Following the dissolution of the lead halide salt, an A-site cation precursor is injected into the reaction vessel at temperatures ranging from 140 to 200 °C.^{6,8-10} Then, the reaction was quenched by immersing the reaction vessel in an ice bath. In fact, the hot injection method provides precise control of the particle size and distribution. However, the hot injection method faces many challenges for the large-scale synthesis. For example, rapid injection of a large quantity of precursor solution at once is very difficult. Furthermore, immediately and homogeneously reducing the reaction temperature can be very cumbersome for the large volumes.¹¹

On the other hand, in the LARP method, lead halide, and A-site cation salts are dissolved in the polar organic solvents such as dimethylformamide or dimethyl sulfoxide, and these precursors are injected into an anti-solvent (hexane and toluene, etc.) with coordinating ligands. Nanocrystal formation immediately occurs when the precursors are injected into the anti-solvent.³ It should be noted that these polar organic solvents used in the LARP technique, such as dimethylformamide, are not suitable for industrial-scale synthesis because of their toxicity.^{12,13} In addition, the amount of these polar solvent residues can affect the perovskite nanocrystal stability and morphology.¹⁴ Furthermore, polar solvents may cause degradation or aggregation due to the susceptible nature of the perovskite nanocrystals against polar solvents.¹³

Therefore, in recent years, new perovskite nanocrystal synthesis procedures taking into account of these concerns have been successfully developed.^{11-13,15-17} Wei et al.¹⁵ developed a polar solvent-free CsPbBr₃ nanocube synthesis method at room temperature and in an air atmosphere. In their study, they dissolved PbBr₂ in toluene with the help of tetraoctylammonium bromide (TOAB), and they reacted the PbBr₂ solution with Cs-oleate solution and hence they obtained high-quality CsPbBr₃ nanocubes. Moreover, Song et al.¹⁶ have modified the synthesis developed by Wei et al.¹⁵ for using the nanocrystals in the perovskite light-emitting diode (LED) application. They have

changed oleic acid with an octanoic acid, a shorter ligand than oleic acid, to increase the charge injection and transportation properties of the perovskite nanocrystal layer. Additionally, they have used didodecyldimethylammonium bromide (DDAB) to provide better surface passivation for the nanocrystals and the increased PL features, and thus they have demonstrated highly efficient perovskite LEDs. On the other hand, Almeida et al.¹² developed a phosphine oxide route for the synthesis of CsPbBr₃ nanocubes. In their study, they dissolved PbBr₂ in toluene in the presence of trioctylphosphine oxide (TOPO) at 75 °C. Subsequently, they reacted PbBr₂ precursor solution with Cs-oleate at the desired reaction temperature ranging from 25 °C to 140 °C. Furthermore, Brown et al.¹¹ reported a synthesis method that allowed tuning the nanocrystals size at room temperature. In their work, TOPO was used to dissolve PbBr₂ salt in toluene, and the PbBr₂ solution was reacted with Cs-octanoate in the presence of octylphosphonic acid (OPA). They successfully modulated the size of CsPbBr₃ nanocrystals by varying the concentration of OPA or the reaction time. They terminated the CsPbBr₃ growth reaction by incorporating the ligand didodecyldimethylammonium bromide into the synthesis solution. In addition, Akkerman et al.¹⁷ reported a room-temperature synthesis method where they prepared an A-site precursor solution by reacting diisooctylphosphinic acid (DOPA) with Cs₂CO₃. They used TOPO to dissolve PbBr₂ salt in toluene. Therefore, at room temperature, the Cs-DOPA solution was reacted with the PbBr₂ precursor. In fact, they successfully altered the nanocrystal size by varying the amount of precursor used in the synthesis.

Herein, we demonstrate polar solvent-free room temperature synthesis of CsPbX₃ (X = Br, Cl) nanocubes by using GA. Primarily, the smaller diffusion coefficient and higher steric hindrance of oleylammonium molecules prevent the addition of monomeric species to the nanocrystal and cause the formation of anisotropic nanostructures such as nanowires and nanoplatelets. The synthesis yields monodisperse perovskite nanocubes when we use 4-5-fold higher concentrations of GA than oleylammonium. We propose that the higher diffusion coefficient of GA molecules, impairs the restricted monomer-addition effect of oleylammonium to the nanocrystal. It should be noted that the amino groups of GA molecules interact more favorably with the surface bromides and reduce the binding affinity of the surface ligands.¹⁸ The oleylammonium population on the surface of the nanocrystals is insufficient to form perovskite nanowire and nanoplatelet, and hence perovskite nanocube formation occurs. Moreover, we investigate GA-assisted nucleation and growth kinetics of perovskite nanocubes by performing in-situ PL and

absorption measurements. We observe the nucleation of small nanocrystals with excitonic absorption peak around 435 nm and PL maxima at 447 nm. Additionally, continuous PL and absorption red shift is observed during the growth of these nanocrystals. Moreover, STEM images demonstrate that the high GA concentration reaction yields only CsPbX₃ nanocubes. In the powder X-ray diffraction (XRD) patterns, we do not observe any peak shifting to lower angles and hence, large GA cations may not be doped to the perovskite structure. Complementarily, Fourier transform infrared (FTIR) spectroscopy analysis shows that OLAM and GA are attached to the surface of the perovskite nanocubes. Importantly, our method is the only method that enables the polar solvent-free synthesis of the CsPbCl₃ nanocrystals at room temperature. We believe that the synthesized perovskite nanocubes with our facile method can be used in future optoelectronic devices.

3.2. Results and Discussion

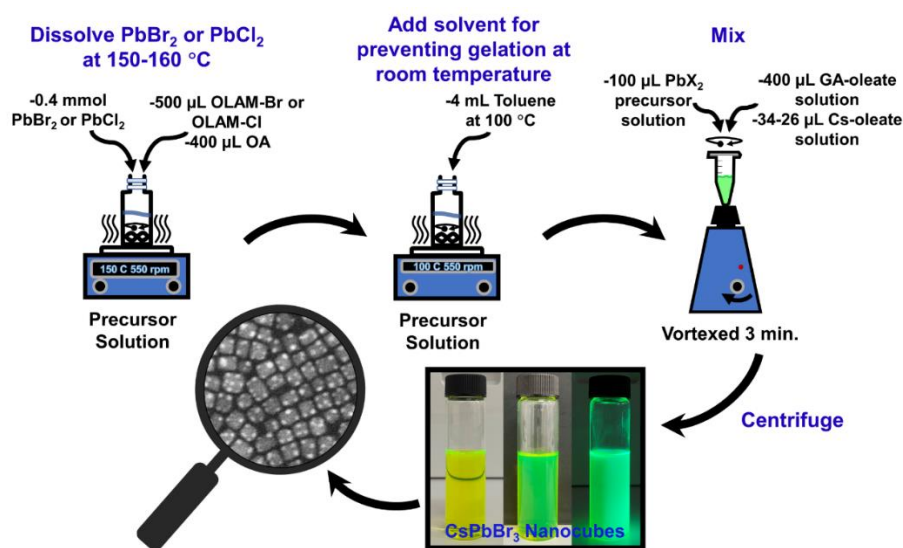


Figure 3.1. Schematic representation of GA assisted polar solvent free synthesis of the CsPbX₃ (X=Br, Cl) nanocubes at room-temperature.

Figure. 3.1 demonstrates the schematic presentation of the GA-oleate assisted synthesis of the CsPbX₃ nanocubes. Firstly, PbBr₂ or PbCl₂ salts were dissolved in OA and OLAM-Br or OLAM-Cl solution at elevated temperatures. An amount of toluene was added to the prepared PbX₂ solution to prevent the gelation of this mixture at room temperature. Cs-oleate was synthesized with a similar procedure reported by Protesescu et al. with a slight modification.⁶ We did not use 1-octadecene (ODE), a high boiling point

nonpolar solvent, in the synthesis of the Cs-oleate because the synthesis reported in this study occurs at room temperature. It should be noted that polymerization of 1-octadecene to poly(1-octadecene) at high temperatures was reported in a previous work.¹⁹ Removing poly(1-octadecene) with standard separation procedures such as precipitation dispersion cycles or size exclusion chromatography is cumbersome and costly. In fact, the presence of poly(1-octadecene) in nanocrystal colloids has a negative impact on the performance of nanocrystal-based devices.¹⁹ Therefore, in our synthesis, Cs_2CO_3 was reacted with oleic acid at an elevated temperature. Subsequently, the solution was removed from the oil bath, and an amount of toluene was injected into the Cs-oleate solution (0.25 M). Additionally, a similar procedure was applied for GA-oleate (0.25 M) synthesis (for further information about Cs-oleate and GA-oleate synthesis, see the Materials and Methods section). Further, PbX_2 (100 μL) and Cs-oleate (34-26 μL) solutions were reacted in the GA-oleate solution (400 μL). The crude solution was centrifuged and redispersed in hexane for further experiments. Importantly, the addition sequence of precursors is very vital for obtaining perovskite nanocubes reported in this study. Firstly, GA and Cs oleate solutions should be mixed.

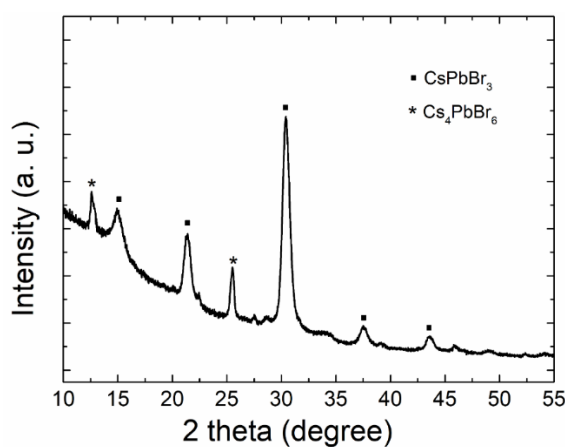


Figure 3.2. XRD pattern shows the formation of both CsPbBr_3 and Cs_4PbBr_6 phases when the molar ratio of Cs/Pb is 2.

Secondly, the PbX_2 solution should be added to this solution combination. Most probably, the addition sequence of precursors has influenced the nucleation and growth mechanism of nanocrystals. However, these variations in nanocrystal's nucleation and growth will be investigated in detail in a future study. Nucleation of nanocrystals immediately occurred, and the nanocrystal solution was vortexed to the growth of nanocrystals. Synthesis of nanocrystal occurs in Cs rich (the molar ratio of Cs/Pb is 1.7)

environment unlike the hot injection method (the molar ratio of Cs/Pb is 0.27).⁶ The higher Cs amount (the molar ratio of Cs/Pb is 2) can cause the formation of the Cs₄PbX₆ phase (see Figure 3.2).

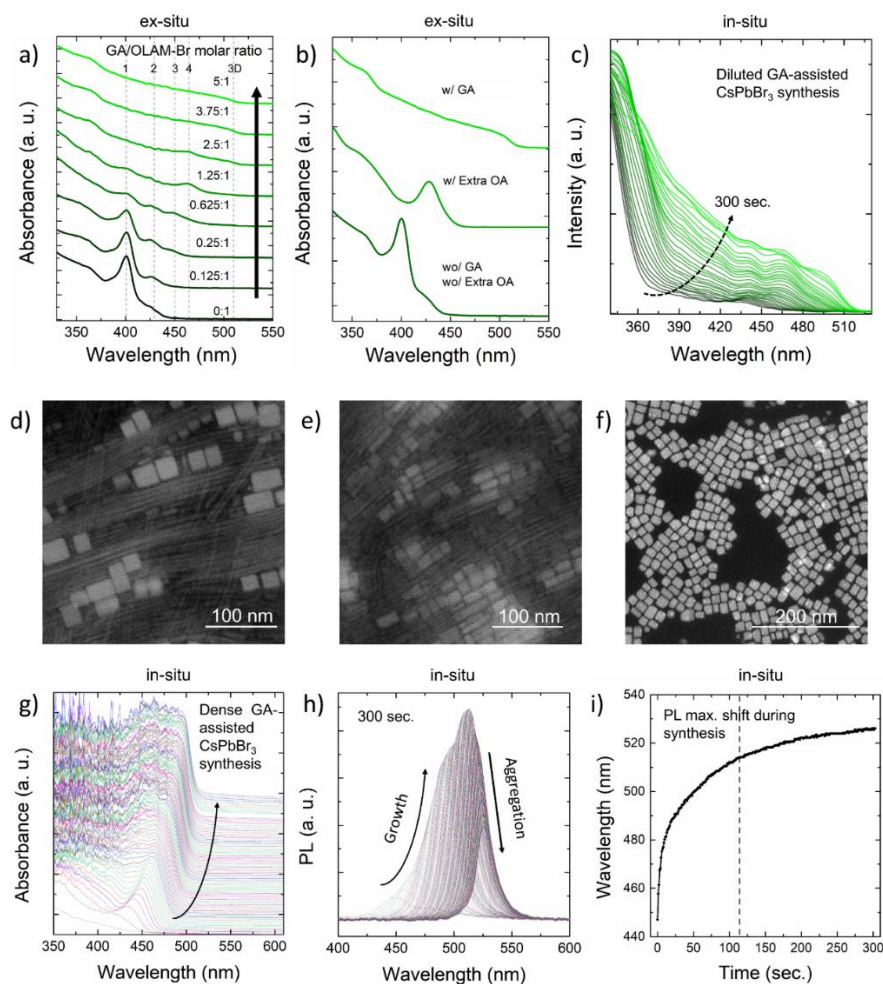


Figure 3.3. (a) GA-oleate amount (mL) dependent ex-situ absorption spectra of the synthesized nanocrystals. A fixed amount of Cs-oleate was used for varying GA-oleate amounts in the synthesis. (b) Comparison of the absorption spectra of the synthesized nanocrystals from bottom to top: the first absorption spectrum belongs to the synthesis, which does not contain both GA and extra OA, the second absorption spectrum belongs to the synthesis containing extra OA, and the last absorption spectrum belongs to the synthesis containing GA. (c) In-situ absorption spectra of the diluted GA-assisted synthesis. STEM image of the samples, which have molar ratios of GA/OLAM-Br as (d) 0.625/1, (e) 1.25/1, and (f) 5/1. In-situ (g) absorption and (h) PL spectra of the dense GA-assisted synthesis (i) PL maxima shift during the synthesis.

The GA amount used in the synthesis of the CsPbBr₃ nanocrystals increases from bottom to top in Figure 3.3a. Ex-situ absorption measurements clearly show the formation of Ruddlesden Popper (R-P) phases since the quantized energies of these layered R-P phases depend on the number of octahedral layers (n) in a confined dimension. As a result, excitonic peaks are observed at specific energies, indicating L₂[CsPbBr₃]_{n-1}PbBr₄ (n = 1, 2, 3, 4) type structures.²⁰⁻²³ The first absorption spectra at the bottom in Fig. 2a correspond to nanoparticles synthesized without using GA. A sharp excitonic peak at around 400 nm and an absorption edge at 428 nm were observed in the absorption spectra of the GA free nanocrystals. The excitonic peak at 400 nm may indicate the formation of L₂PbBr₄ (n = 1) R-P phase or CsPbBr₃ clusters.²²⁻²⁶ The absorption peak at 428 nm corresponds to L₂[CsPbBr₃]PbBr₄ (n = 2) nanocrystals.²²⁻²⁴ The third absorption peak at around 450 nm was observed in the synthesis where the molar ratio of GA/OLAM-Br was 0.25/1. The peak at 450 nm belongs to L₂[CsPbBr₃]₂PbBr₄ (n = 3) perovskite nanocrystals.^{23,24} An apparent absorption peak at 465 nm was observed when the molar ratio of GA/OLAM-Br was 1.25/1 in the synthesis, indicating the formation of L₂[CsPbBr₃]₃PbBr₄ (n = 4) nanocrystals.²³ Upon further increase of the molar ratio of GA/OLAM-Br to 2.5/1, an absorption edge at around 510 nm appears. Lastly, all other peaks lower than 510 nm wavelength, which belong to the low dimensional perovskite nanocrystals, disappeared when the molar ratios of GA/OLAM-Br are 3.75/1 and 5/1 in the synthesis, and only a single absorption edge at around 510 nm was observed in the absorption spectra. The absorption edge at around 510 nm shows the formation of weakly quantum confined nanocrystals.²³ Furthermore, the dashed lines in the ex-situ absorption spectra demonstrate "n" values from left to right. The layer number increases from 1 to 4 for the first four dashed lines, and the last dashed line at 510 nm indicates the 3D perovskite structure. In figure. 3.3a, when GA amount increases in the reaction, the thickness of the 2D R-P perovskite increases, and this growth occurs with a jump from one specific energy to another.²⁷ The figure 3.3d, e, and f show STEM images of the CsPbBr₃ nanocrystals, which have the molar ratio of GA/OLAM-Br as 0.625/1 (Fig. 2d), 1.25/1 (Fig. 3.3e), and 5/1 (Fig. 3.3f), respectively. These STEM images were consistent with the ex-situ absorption data. It is clear that at the low molar ratios of GA/OLAM-Br, very thin nanowires and nanoplatelet were all successfully synthesized. Moreover, figure 3.3f demonstrates that homogenous nanocube morphology was obtained when the molar ratio of GA/OLAM-Br was 5/1 in the synthesis.

Further, in Figure 3.3b, we have investigated the effect of addition of an extra amount of oleic acid in order to understand whether only oleic acid addition is enough for the nanocube formation. It should be noted that we used GA oleate as a GA precursor in the synthesis, it contained an excess amount of oleic acid. Therefore, 0.63 M oleic acid solution in toluene (400 μ L) was used as a reaction medium. Similarly, Cs-oleate and PbBr₂ amounts were kept constant as in the case of GA-modified synthesis. Extra amount of oleic acid causes the instant formation of L₂[CsPbBr₃]PbBr₄ (n = 2) R-P nanocrystals, which have an absorption peak at around 428 nm. When the synthesis was performed without addition of extra OA and GA-oleate, an excitonic peak at around 400 nm and a second absorption peak at around 428 nm were observed. Instant formation of L₂[CsPbBr₃]PbBr₄ (n = 2) R-P nanocrystals may be related to maintaining the protonation of Cs in the solution with the addition of extra oleic acid.²⁸ It is clearly shown that only extra amount of oleic acid addition into the synthesis is not enough for the formation of CsPbBr₃ nanocubes at room temperature. Similarly, Mehetor et al. have recently reported that extra oleic acid addition into the parent perovskite solution increases the polarity of the solution and oleylammonium ion formation, and hence they have demonstrated that oleic acid addition increases the formation of L₂PbBr₄ and L₂[CsPbBr₃]PbBr₄ type nanoplatelets.²⁸

In previous studies, influence of alkylamine chain length on the perovskite nanocrystals size was extensively studied.^{29–32} Cho et al.²⁹ showed modulation of thickness of MAPbBr₃ nanoplatelets by varying the chain length of alkyl amines in the synthesis. They have clearly demonstrated that increasing chain length of alkyl amines also causes the formation of thinner nanoplatelets. Moreover, in another study, Kumar et al.³⁰ have observed similar trend in the nanocrystal size by variation of the alkylamine chain length. In this work, addition of GA in the synthesis increases the nanocrystal size, which is very similar to the addition of small chain length alkyl amines in the synthesis. It should be noted that long chain alkylammonium molecules have lower diffusion coefficients, resulting in higher steric hindrance, increased aggregation enthalpy, and obstructing monomeric species addition to the nanocrystal.²⁹ As a result, long-chain alkylammonium molecules cause the formation of thinner perovskite nanoplatelets. In this work, the synthesis method contains 0.1 mmol GA, and 0.021 mmol oleylammonium halide. Therefore, we hypothesize that when the concentration of GA molecules exceeds a critical threshold, the restriction of the monomer addition effect of oleylammonium molecules deteriorates due to the higher diffusion coefficient of GA molecules. As a

result, there aren't enough oleylammonium molecules on the nanocrystal surface to generate R-P phases. This could also explain why a high concentration of GA-oleate is required to synthesize CsPbX₃ nanocubes. Also, Kim et al. have recently demonstrated via density functional theory (DFT) calculations that GA tends to migrate to the surface of the FAPbBr₃ nanocrystals and stabilize nanocrystals surfaces due to the increased number of hydrogen bonds and hence GA molecules slightly weaken the binding ability of other ligands to the nanocrystal surface.¹⁸

In order to track the formation perovskite nanocubes, in-situ absorption and PL measurements were used. It should be noted that, in our earlier work, we, for the first time, investigated the formation of 2D R-P perovskites by in-situ absorption measurements.²¹ Here, we monitored the nanocrystal nucleation and growth of nanocrystals in the presence of GA in toluene. Additionally, we investigated nanocrystal nucleation and growth without using GA in toluene and hexane (see Figure 3.4).

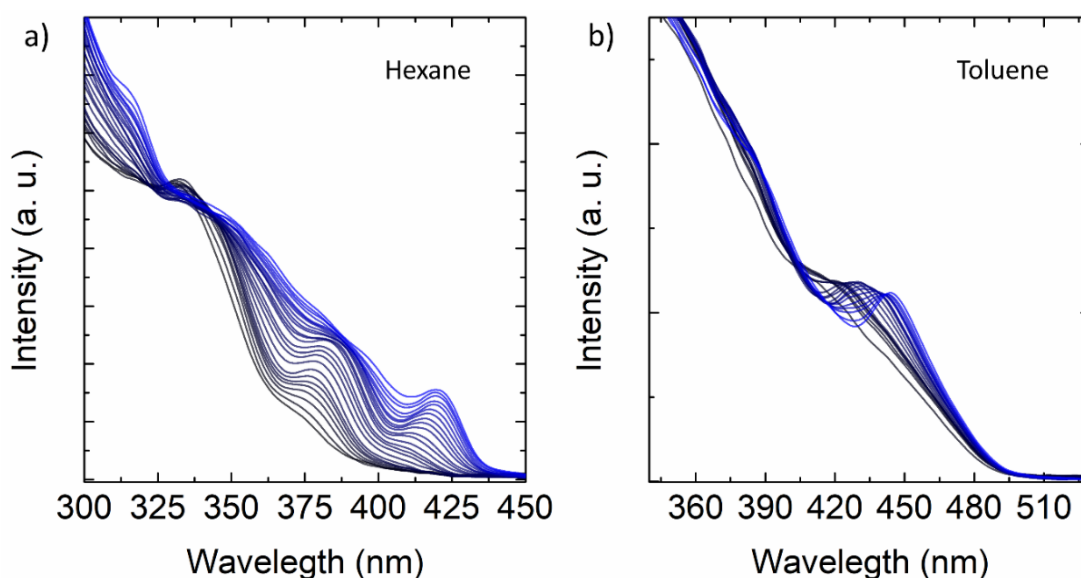


Figure 3.4. In-situ absorption measurement of the synthesis of CsPbBr₃ nanocrystals without the addition of GA-oleate (a) in hexane and (b) in toluene.

In Figure. 3.3c and g, an apparent shift to higher wavelengths and enhancement in absorption spectra were all observed during both diluted and dense forms of GA-assisted CsPbBr₃ nanocube synthesis. It should be noted that when GA was diluted in toluene for in situ absorption measurements, synthesis could not be performed using the ratios specified above. Therefore, we re-optimized the used precursor amounts (2 mL

toluene, 6 μL GA-oleate, 4 μL Cs-oleate, and 12.5 μL PbBr_2) for the diluted synthesis. Moreover, we used five times higher precursor amounts during in-situ absorption and PL measurements in order to avoid diluting the GA in toluene. Figure 3.3g and h show in-situ absorption and PL measurements of the dense GA-assisted CsPbBr_3 synthesis. We observe that at the beginning of the synthesis an excitonic absorption peak was observed at around 435 nm. While the reaction continues, the excitonic features of the absorption peak decreases gradually and absorption peak shifts to the longer wavelengths. Similar to the diluted synthesis, in the dense synthesis, continuous red shift was observed in the in-situ absorption and PL measurements. It should be noted that, during the growth of nanocrystals, continuous shift to longer wavelengths was observed in quantum dots and three dimensional nanocrystals (cubes, spheres, etc.).^{17,27,33} In the case of the low dimensional nanocrystal morphologies (nanoplatelets, and magic size clusters), the growth of nanocrystals occurs via discrete size jumps.²⁷ These jumps can be observed in the absorption and PL spectra as a decrease in the peak intensity of one specific energy and the formation and the increase in the intensity of a new peak in a lower energy region.²⁷ ¹⁸ Therefore, the observed continuous shift in the absorbance and PL spectra confirms that synthesis was conducted without the formation of nanowires and nanoplatelets. On the other hand, the PL intensity increases during the first 120 seconds of synthesis, and after that, it gradually decreases until 300 seconds. As the concentration of the nanocrystals increases, nanocrystals begin to interact with each other and form larger clusters and aggregates. The PL maxima shift to 525 nm during the synthesis, as shown in Fig. 3.3i. However, when the nanocrystal colloid is precipitated and redispersed in hexane, it has an emission at around 510 nm. We believe that this small red shift in the crude solution is due to the aggregation of the nanocrystals. In fact, it is known that the increased interaction between nanocrystals in clusters, aggregates, or superlattices causes a red shift in the spectrum.^{34,35} Moreover, Di Stasio et al. have demonstrated that aggregation and self-absorption induce a decrease in the PLQY, and a red shift in the PL maxima has been observed in the concentrated CsPbBr_3 colloids.³⁴

The morphology of the CsPbX_3 nanocrystals, which were synthesized by using a molar ratio of GA/OLAM-X as 5/1, was analyzed by using the scanning transmission electron microscopy (STEM) mode of TEM. Cube-shaped perovskite nanocrystals have been observed in Figure 3.5a, b, and c. The average particle sizes of CsPbBr_3 , $\text{CsPb}(\text{Cl}_{0.5}\text{Br}_{0.5})_3$, and CsPbCl_3 nanocubes are 14.18 nm, 12.17 nm, and 10.40 nm with standard deviations of 0.22 nm, 0.32 nm, 0.17 nm, respectively. As can be seen from the

STEM images, the CsPbX_3 nanocubes have truncated vertices. It should be noted that truncation of vertices indicates the formation of the (110) facets of the CsPbX_3 nanocubes. In previous studies, truncation of vertices and edges was observed in halide-deficient conditions or when perovskite nanocrystal surfaces were passivated with alkyl phosphonic acids.^{36–38} Moreover, the low PLQY of the CsPbCl_3 nanocrystals may be related to the truncated vertices since the newly created and halide deficient (110) facets cause the formation of trap states and hence decrease the PLQY of the nanocrystals.^{36,39}

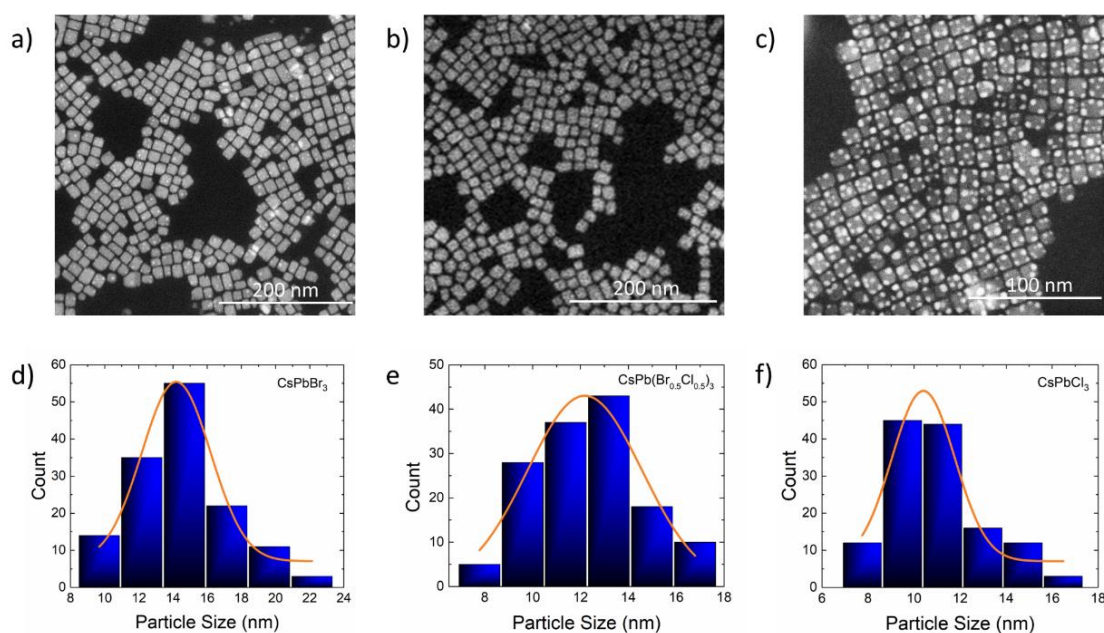


Figure 3.5. (a, b, c) STEM images of the CsPbBr_3 , $\text{CsPb}(\text{Cl}_{0.5}\text{Br}_{0.5})_3$, and CsPbCl_3 nanocubes and (d, e, f) their related particle size distributions, respectively.

PL and absorption spectra of CsPbBr_3 , $\text{CsPb}(\text{Cl}_{0.5}\text{Br}_{0.5})_3$, and CsPbCl_3 nanocubes are shown in Figure 3.6a. The synthesized CsPbBr_3 , $\text{CsPb}(\text{Cl}_{0.5}\text{Br}_{0.5})_3$, and CsPbCl_3 nanocubes have absorption edges at around 400 nm, 440 nm, and 503 nm, respectively. Furthermore, the PL peak maxima of the nanocubes are observed at 405 nm, 443 nm, and 508 nm for CsPbCl_3 , $\text{CsPb}(\text{Cl}_{0.5}\text{Br}_{0.5})_3$, and CsPbBr_3 , respectively. The band gap energy of the perovskite nanocrystals increases with increasing chloride concentration in the composition from CsPbBr_3 to $\text{CsPb}(\text{Cl}_{0.5}\text{Br}_{0.5})_3$, and further CsPbCl_3 .⁶ Indeed, the increase in the band gap energy is caused by the change in the valence band composition from 4p to 3p with increasing chloride concentration.^{40,41} The full width at half maxima (FWHM) of PL peaks range from 72 meV for the CsPbCl_3 nanocubes to 106 meV for the CsPbBr_3 nanocubes. It has been well-known that changing the anion composition from

Cl to Br broadens the linewidth of the PL peaks in perovskite nanocrystals. The PLQY values of the synthesized nanocubes are 85.6%, 58.8%, 5.7% for CsPbBr₃, CsPb(Cl_{0.5}Br_{0.5})₃, and CsPbCl₃, respectively. Similar to the previous studies, in our study, we have observed that increasing chloride amount in the perovskite composition reduces the PLQY. The low PLQY values in the CsPbCl₃ nanocrystals can be described by the abundant surface defects (chloride vacancies).^{42–44} Figure 3.6b shows digital images of GA-modified perovskite nanocube colloids taken under the daylight and the UV light.

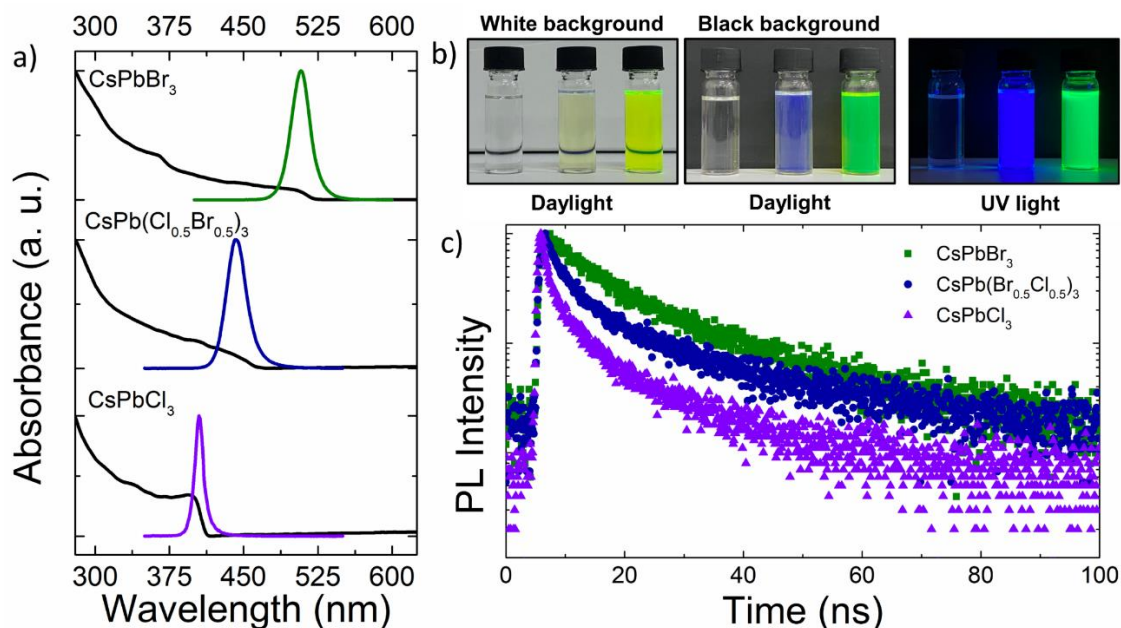


Figure 3.6. (a) PL and absorption spectra of CsPbBr₃, CsPb(Cl_{0.5}Br_{0.5})₃, and CsPbCl₃ nanocubes. (b) Digital images demonstrate nanocube colloids in front of the white background under the daylight (left), in front of the black background under the daylight (middle), and under the illumination of 365 nm UV light (right). In each digital image, CsPbCl₃, CsPb(Cl_{0.5}Br_{0.5})₃, and CsPbBr₃ nanocube colloids were arranged from left to right, respectively. (c) Time-resolved PL lifetime decays of the CsPbBr₃, CsPb(Cl_{0.5}Br_{0.5})₃, and CsPbCl₃ nanocubes.

Moreover, the PL lifetime decays of GA-modified nanocubes have been demonstrated in Figure 3.6c. The average lifetime of the nanocubes decreases with increasing bandgap from CsPbBr₃ to CsPbCl₃. It should be noted that, in previous works, the faster charge carrier dynamics have been reported with increasing band gap energy in the perovskite nanocrystals.^{45–47} Time resolved PL life-time decay of CsPbBr₃,

CsPb(Cl_{0.5}Br_{0.5})₃ nanocrystals were fitted with biexponential function and CsPbCl₃ nanocrystals with triexponential function (see Table 3.1). Average life time of the CsPbBr₃, CsPb(Cl_{0.5}Br_{0.5})₃, and CsPbCl₃ nanocubes are 18.98 ns, 18.97 ns, and 14.74 ns, respectively. In a previous study, Imran et al. have reported average PL lifetime values of 7.36 ns and 12.52 ns for CsPbCl₃ and CsPbBr₃ nanocrystals synthesized by using the benzoyl halide route.⁴⁸ In another study, Dutta et al. observed 1.18 ns and 6.43 ns average lifetime values for CsPbCl₃ and CsPbBr₃ nanocrystals.⁴⁹ In these studies, synthesized nanocrystals are well passivated with oleylammonium ions. Importantly, the average lifetime values reported in this study are higher than the average lifetime values reported in the previous reports. Prolonged lifetime values may indicate the well-passivated surfaces of our perovskite nanocrystals. Moreover, increasing in average PL lifetime was reported in the CsPbI₃ nanocrystals via the exchange of oleylammonium with GA.⁵⁰

Table 3.1. Time resolved photoluminescence life-time decays of CsPbBr₃, CsPb(Cl_{0.5}Br_{0.5})₃, and CsPbCl₃ nanocubes.

Sample	τ_1 (ns)	τ_2 (ns)	τ_3 (ns)	A_1 (%)	A_2 (%)	A_3 (%)	τ_{avg} (ns)
CsPbBr ₃	5.98	20.35	-	26.34	73.66	-	18.98
CsPb(Cl _{0.5} Br _{0.5}) ₃	3.12	20.10	-	31.50	68.50	-	18.97
CsPbCl ₃	0.77	4.29	17.33	15.94	40.11	43.95	14.74

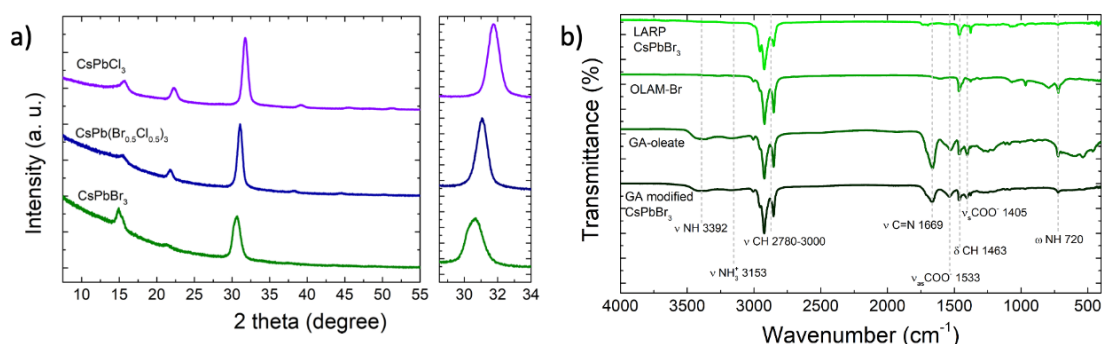


Figure 3.7.(a) XRD patterns of the CsPbBr₃, CsPb(Cl_{0.5}Br_{0.5})₃, and CsPbCl₃ nanocubes. (b) FTIR spectra of the CsPbBr₃ nanocubes synthesized by the LARP method, OLAM-Br solution, GA-oleate, and GA modified CsPbBr₃ nanocubes synthesized in this work.

Figure 3.8a demonstrates XRD patterns of the CsPbBr₃, CsPb(Cl_{0.5}Br_{0.5})₃, and CsPbCl₃ nanocubes. XRD diffractograms of the perovskite nanocubes indicate that the synthesized CsPbBr₃ and CsPbCl₃ nanocubes have orthorhombic and cubic crystal structures, respectively. As demonstrated in Figure. 3.8, we did not observe any difference at the peak positions in XRD patterns of GA-assisted synthesized CsPbBr₃ nanocubes and a reference XRD pattern⁵¹, which indicates that GA cations did not dope to the 3D perovskite structure.

Additionally, in a recent study, Yuan et al. have demonstrated the synthesis of the CsPbI₃ nanocrystals with GA-anchored surfaces. In this synthesis, they did not observe any peak shifting to lower angles in the XRD patterns due to the replacing of the GA cation with the Cs cation in the CsPbI₃ nanocrystals. It should be noted that the CsPbI₃ crystal structure has larger lattice constants than the CsPbBr₃ crystal structure; therefore, doping of the GA cation into the A site of the CsPbBr₃ perovskite crystals is much less possible than CsPbI₃ crystal structure.^{51,52} In fact, the high concentrations of GA tend to migrate to the surface of nanocrystals, which may be why GA cations were not able to dope the CsPbBr₃ nanocrystals.¹⁸ Further, GA cation has a 279 pm ionic radius, which is too large for the formation of the 3D APbBr₃ type perovskite structure.⁴¹ Even in the case of 2D R-P perovskite phases, which have self-adjustable strain balancing effects, no one has yet reported L₂[GAPbBr₃]PbBr₄ type structure because these structures are far beyond the Goldschmidt tolerance factor.^{53,54} On the other hand, obvious peak shifting can be seen in the XRD diffractograms upon increasing the Cl amount in the perovskite nanocubes. This peak shifting to higher angles with increasing Cl content in the composition of the perovskite nanocubes from CsPbBr₃ to CsPbCl₃ indicates shrinkage of the perovskite lattice. Note that the Cl (167 pm) anion site is much smaller than the Br (182 pm) anion in the 6 coordination.⁵⁵

The presence of ligands on the surface of CsPbBr₃ nanocube was investigated by using FTIR spectroscopy. Figure 3.7b shows FTIR spectra of CsPbBr₃ nanocrystals synthesized by using the LARP method, OLAM-Br solution, GA-oleate, and GA-oleate modified CsPbBr₃ nanocubes, respectively. The observed bands at 3392 and 3153 cm⁻¹ correspond to N-H stretching modes of guanidinium or oleylammonium molecules.⁵⁶⁻⁵⁹ The absorption peak observed at around 1668 cm⁻¹ demonstrates $\nu_{C=N}$ of guanidinium groups.^{56,59} Also, the observed signals at around 1533 and 1405 cm⁻¹ indicate asymmetric and symmetric stretching modes of the COO⁻ group of oleate species, respectively.^{57,58} The absorption peaks between 2780-3000 cm⁻¹ show stretching of C-H bonds in the long

alkyl chains of the oleate or oleylammonium molecules. In a recent work, the spontaneous replacement of the oleylammonium with GA at the surface of CsPbI₃ nanocrystals was demonstrated in the hot injection method.⁵⁰ Moreover, the GA molecule has extra amino groups, and hence GA molecules can more favorably interact with the surface bromides.¹⁸ We believe that this is the main reason for the spontaneous exchange of some of OLAM with GA on the nanocrystal surface. In fact, the FTIR spectra indicate that the synthesized nanocubes are passivated with GA, oleates, and oleylammonium.

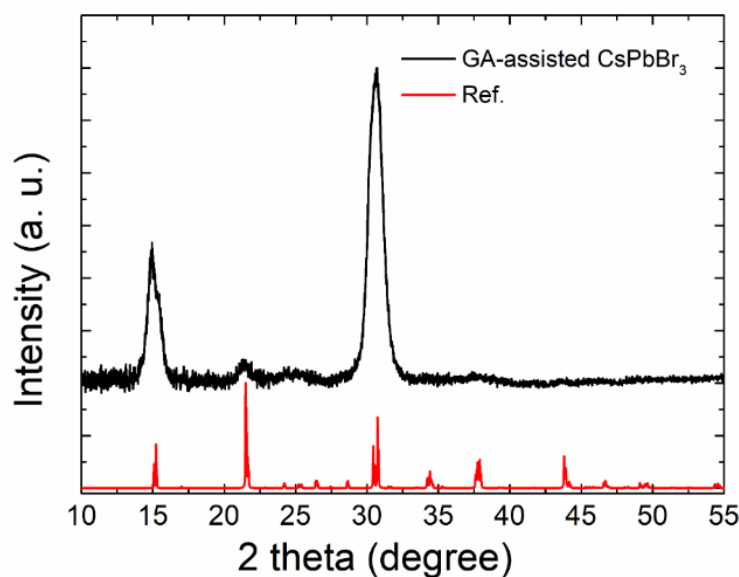


Figure 3.9. Comparison of the XRD patterns of the GA-assisted synthesized CsPbBr₃ nanocubes and reference XRD pattern.

3.3. Conclusion

In this work, we report room temperature polar solvent-free synthesis of CsPbX₃ (X = Cl, Br) nanocubes. We use GA and widely used oleylamine and oleic acid ligands in the perovskite nanocube synthesis. We demonstrate that GA concentration strongly affects the morphology of the synthesized nanocrystals. At the low molar ratio of GA/OLAM, nanoplatelets and very thin nanowires have been observed. On the other hand, synthesis yields homogenous nanocubes for the high molar ratio of GA/OLAM. When the GA concentration exceeds a critical threshold, the restricted monomer-addition effect of oleylammonium molecules is deteriorated due to the larger diffusion coefficient of GA molecules. Therefore, oleylammonium molecules do not have enough population

on the nanocrystal surface to produce low dimensional structures. Further, in-situ absorption and PL measurements support the conclusions. In fact, we observe continuous absorption and PL shift to the lower energetic region without any discrete jump from one specific energy to another in in-situ absorption and PL measurements. It has been well-known that low dimensional nanocrystals such as nanoplatelets and magic size clusters grow with discrete size jumps.²⁷ The GA molecules can more favorably interact with the surface bromides since the GA molecules have extra amino groups.¹⁸ Therefore, the spontaneous exchange of the oleylammonium with GA on the nanocrystal surface was observed. Moreover, XRD patterns indicated GA cation was not incorporated into the perovskite lattice. Further, FTIR analysis demonstrates that GA is attached to the surface of the CsPbX₃ (X = Cl, Br) nanocrystal. The method demonstrated in this study is the only method that allows the synthesis of CsPbCl₃ nanocubes at room temperature without using a polar solvent. Further, CsPbBr₃, CsPb(Cl_{0.5}Br_{0.5})₃, CsPbCl₃ nanocubes synthesized here in this study have the PLQY of 85.6 %, 58.8 %, 5.7 %, and average lifetimes of 18.98 ns, 18.97 ns, 14.74 ns, respectively. We envision that the perovskite nanocubes synthesized in this study can be used for future light-emitting devices (LED), photodiodes, or other perovskite-based optoelectronic devices and applications in the visible region of the electromagnetic spectrum.

3.4. Materials and Methods

3.4.1. Chemicals

Lead (II) iodide (PbI₂, 99%), Lead(II) Bromide (PbBr₂, ≥98%) Cesium carbonate (Cs₂CO₃, 99.9%), Formamidine acetate salt (FA-acetate, HN=CHNH₂·CH₃COOH, 99.9%), guanidine carbonate salt (GA-carbonate, NH₂C(=NH)NH₂·½H₂CO₃) 1-octadecene (ODE, 90%), oleylamine (OLAM, 70%), hydroiodic acid (HI, 57 wt. % in water), hydrobromic acid (HBr, 48% in water), hydrochloric acid (HCl, ≥ 37% in water), oleic acid (OA, 90%) and Hexane (EMPLURA®) were all purchased from Sigma-Aldrich and used without any further purification.

3.4.2. Synthesis of OLAM-X

10 mL of OLAM reacted with 1.6 mL HI, 1.4 mL HBr or 1 mL HCl in a 100 mL three neck round bottomed flask for the synthesis of OLAM-I, OLAM-Br, or OLAM-Cl solutions, respectively. First, OLAM was added to the flask; after that, HX solution was added dropwise. OLAM-X stock solutions have concentrations of 1.2 mmol/ml. The mixture was heated to 130 °C for 2 hours under the nitrogen flow. Subsequently, the reaction was cooled down to room temperature and transferred to a vial. Lastly, the prepared solution was diluted with 12 mL OLAM to have a 0.5 mmol/mL concentration.

3.4.3. Synthesis of Cs-oleate

407 mg of Cs₂CO₃, and 2 mL of OA were mixed in a round bottom flask. The mixture was degassed at room temperature for 10 min, and then further degassed for 30 min at 120 °C. Temperature of the reaction vessel was set to 135 °C under the flow of nitrogen gas and kept at the same temperature until a clear solution was obtained. Afterwards, 8 mL of toluene was quickly injected into the reaction flask and the reaction mixture was cooled down to room temperature. Cs-oleate often precipitate at room temperature. Cs-oleate was heated at 100 °C until all precipitate was dissolved prior to use. The Cs-oleate solution was stored at dark and 2-8 °C. Do not use Cs-oleate solution for more than 15 days and be sure used oleic acid in the reaction was appropriately stored at 2-8 °C because it affects the reaction product.

3.4.4. Synthesis of GA-oleate

230 mg of GA-carbonate and 2 mL of OA were loaded in a round bottom flask. The mixture was degassed and mixed at room temperature for 10 minutes and further degassed at 95 °C until a clear solution was obtained. Subsequently, 8 mL of toluene was injected into the reaction flask, and then the flask was cooled down to room temperature. Sometimes with the addition of the toluene some unreacted GA-carbonate was precipitated at the bottom of the flask. If GA-carbonate precipitates, heat the prepared solution at 50 °C and further degas the solution under mild stirring until no precipitate was observed. Some toluene may evaporate during the extra degassing process. The GA-

oleate solution should have a total volume of 10 mL. If not, add toluene to make the total volume of GA-oleate solution 10 mL. Also, GA-carbonate precipitates spontaneously dissolved when precursor solution stored at room temperature overnight. The GA-oleate solution was stored at dark and 2-8 °C. Do not use GA-oleate solution for more than 15 days and be sure used oleic acid in the reaction was appropriately stored at 2-8 °C because it affects the reaction product.

3.4.5. Synthesis of PbBr₂ and PbCl₂ Solution

0.4 mmol of PbBr₂, 500 μL of OLAM-Br, and 400 μL of OA were loaded in a glass tube. This glass tube was placed in an oil bath, degassed at 120 °C, and heated to 150 °C under vigorous stirring until all PbBr₂ solution became completely clear. Then, the solution was cooled down to 100 °C, and 4 mL of toluene was added to the reaction mixture. It should be noted that prepared PbX₂ solution quickly gels if toluene is not added while it is hot. In addition, the precursor solution was cooled down to room temperature and stored at 2-8 °C for further use. Do not use the prepared PbBr₂ solution for more than ten days.

For the synthesis of the PbCl₂ solution, PbCl₂ and OLAM-Cl were used rather than PbBr₂ and OLAM-Br. Also, the reaction temperature was increased from 150 °C to 160 °C. Except for these, all used precursor amounts were kept the same.

3.4.6. CsPbX₃ Nanocube Synthesis

CsPbBr₃ and CsPbCl₃ nanocubes were synthesized using the same amount of precursors. 400 μL of GA-oleate and 34 μL of Cs-oleate were mixed, and then 100 μL of PbBr₂ or PbCl₂ solution was added to the reaction solution. The prepared reaction solution was vortexed for 3 minutes. After that, the crude solution was centrifuged at 15000 rpm for 10 minutes Supernatant discarded, and precipitate dispersed in 400 μL hexane. This solution was centrifuged at 8500 rpm for 5 minutes, the precipitate was removed, and the supernatant stored for further use. For the synthesis of CsPb(Cl_{0.5}Br_{0.5})₃, 26 μL Cs-oleate was used rather than 34 μL Cs-oleate and also 50 μL PbBr₂ solution and 50 μL PbCl₂ solution mixed in a separate vial and then 100 μL of this PbBr₂ and PbCl₂ solution mixture was added. Except for these, all procedure was kept the same for the synthesis of

CsPb(Cl_{0.5}Br_{0.5})₃ nanocubes. This synthesis protocol can be scaled up using the same precursor ratios for all synthesized halide compositions. In the largest batch we tried, 20 times larger volumes of precursors were used. More precisely, 8 mL GA-oleate and 680 μ L Cs-oleate were mixed. After that, 2 mL PbX₂ precursor solution was added to GA-oleate and Cs-oleate mixture. This solution was vortexed for 3 minutes. The prepared solution was purified using the same procedures applied for smaller batches. For the synthesis of the mixed halide nanocrystals, 520 μ L of Cs-oleate was added rather than 680 μ L.

3.4.7. Characterization of NCs

Transmission electron microscopy (TEM) analysis of NCs were carried out in order to observe morphology of the nanocrystals (TEM, JEOL-2100F, Japan). The samples were prepared by drop-casting diluted NC suspensions onto 200 mesh carbon-coated copper grids. The surface of the nanocrystals was characterized by attenuated total reflectance Fourier-transform infrared spectroscopy (Spectrum Two FT-IR Spectrometer, PerkinElmer, USA) in a range of 400-4000 cm⁻¹ with Universal ATR accessory equipment. Absorption (Abs), Photoluminescence (PL), and time-resolved lifetime (LT) measurements were carried out by using a FS5 Spectrofluorometer (Edinburgh Instruments, UK). For PLQY, a Xenon lamp was employed with an excitation wavelength of 350 nm. PLQY of each sample was measured by utilizing an integrating sphere. Samples were diluted in hexane and the optical properties of the nanocrystals were measured in a cylindrical quartz cuvette. In LT measurements, the samples were excited by using a 350 nm laser with a pulse width of 50 ns and a repetition rate of 1 MHz. All of the characterization measurements were performed at room temperature.

3.4.8. In-situ Absorbance and PL Measurements of NCs

In-situ absorption measurements of colloids were performed by using a balanced deuterium–tungsten halogen light source (DH2000-BAL, Ocean Optics) and a fiber-coupled spectrometer (USB4000, Ocean Optics). All the characterization measurements were performed at room temperature. PL measurements were performed by using a

collimated LED light source (M365L2-C1, Thorlabs) and a fiber-coupled spectrometer (USB4000, Ocean Optics).

3.5. References

1. Dey, A.; Ye, J.; De, A.; Debroye, E.; Ha, S. K.; Bladt, E.; Kshirsagar, A. S.; Wang, Z.; Yin, J.; Wang, Y.; Quan, L. N.; Yan, F.; Gao, M.; Li, X.; Shamsi, J.; Debnath, T.; Cao, M.; Scheel, M. A.; Kumar, S.; Steele, J. A.; Gerhard, M.; Chouhan, L.; Xu, K.; Wu, X.; Li, Y.; Zhang, Y.; Dutta, A.; Han, C.; Vincon, I.; Rogach, A. L.; Nag, A.; Samanta, A.; Korgel, B. A.; Shih, C.-J.; Gamelin, D. R.; Son, D. H.; Zeng, H.; Zhong, H.; Sun, H.; Demir, H. V.; Scheblykin, I. G.; Mora-Seró, I.; Stolarczyk, J. K.; Zhang, J. Z.; Feldmann, J.; Hofkens, J.; Luther, J. M.; Pérez-Prieto, J.; Li, L.; Manna, L.; Bodnarchuk, M. I.; Kovalenko, M. V.; Roeffaers, M. B. J.; Pradhan, N.; Mohammed, O. F.; Bakr, O. M.; Yang, P.; Müller-Buschbaum, P.; Kamat, P. V.; Bao, Q.; Zhang, Q.; Krahne, R.; Galian, R. E.; Stranks, S. D.; Bals, S.; Biju, V.; Tisdale, W. A.; Yan, Y.; Hoye, R. L. Z.; Polavarapu, L. State of the Art and Prospects for Halide Perovskite Nanocrystals. *ACS Nano* **2021**, *15* (7), 10775–10981.
2. Bai, S.; Yuan, Z.; Gao, F. Colloidal Metal Halide Perovskite Nanocrystals: Synthesis, Characterization, and Applications. *J Mater Chem C Mater* **2016**, *4* (18), 3898–3904.
3. Zhang, F.; Zhong, H.; Chen, C.; Wu, X.; Hu, X.; Huang, H.; Han, J.; Zou, B.; Dong, Y. Brightly Luminescent and Color-Tunable Colloidal CH₃NH₃PbX₃ (X = Br, I, Cl) Quantum Dots: Potential Alternatives for Display Technology. *ACS Nano* **2015**, *9* (4), 4533–4542.
4. Shamsi, J.; Urban, A. S.; Imran, M.; De Trizio, L.; Manna, L. Metal Halide Perovskite Nanocrystals: Synthesis, Post-Synthesis Modifications, and Their Optical Properties. *Chem Rev* **2019**, *119* (5), 3296–3348.
5. Chen, J.-K.; Zhao, Q.; Shirahata, N.; Yin, J.; Bakr, O. M.; Mohammed, O. F.; Sun, H.-T. Shining Light on the Structure of Lead Halide Perovskite Nanocrystals. *ACS Mater Lett* **2021**, *3* (6), 845–861.
6. Protesescu, L.; Yakunin, S.; Bodnarchuk, M. I.; Krieg, F.; Caputo, R.; Hendon, C. H.; Yang, R. X.; Walsh, A.; Kovalenko, M. V. Nanocrystals of Cesium Lead Halide Perovskites (CsPbX₃, X = Cl, Br, and I): Novel Optoelectronic Materials

- Showing Bright Emission with Wide Color Gamut. *Nano Lett* **2015**, *15* (6), 3692–3696.
- Davis, A. H.; Li, S.; Lin, H.; Chu, C.; Franck, J. M.; Leem, G.; Maye, M. M.; Zheng, W. Ligand-Mediated Synthesis of Chemically Tailored Two-Dimensional All-Inorganic Perovskite Nanoplatelets under Ambient Conditions. *J Mater Chem C Mater* **2021**, *9* (40).
 - Otero-Martínez, C.; García-Lojo, D.; Pastoriza-Santos, I.; Pérez-Juste, J.; Polavarapu, L. Dimensionality Control of Inorganic and Hybrid Perovskite Nanocrystals by Reaction Temperature: From No-Confinement to 3D and 1D Quantum Confinement. *Angewandte Chemie International Edition* **2021**, *60* (51), 26677–26684.
 - Guvenc, C. M.; Yalcinkaya, Y.; Ozen, S.; Sahin, H.; Demir, M. M. Gd³⁺-Doped α -CsPbI₃ Nanocrystals with Better Phase Stability and Optical Properties. *Journal of Physical Chemistry C* **2019**, *123* (40), 24865–24872.
 - Mir, W. J.; Alamoudi, A.; Yin, J.; Yorov, K. E.; Maity, P.; Naphade, R.; Shao, B.; Wang, J.; Lintangpradipto, M. N.; Nematulloev, S.; Emwas, A.-H.; Genovese, A.; Mohammed, O. F.; Bakr, O. M. Lecithin Capping Ligands Enable Ultrastable Perovskite-Phase CsPbI₃ Quantum Dots for Rec. 2020 Bright-Red Light-Emitting Diodes. *J Am Chem Soc* **2022**, *144* (29), 13302–13310.
 - Brown, A. A. M.; Vashishtha, P.; Hooper, T. J. N.; Ng, Y. F.; Nutan, G. v.; Fang, Y.; Giovanni, D.; Tey, J. N.; Jiang, L.; Damodaran, B.; Sum, T. C.; Pu, S. H.; Mhaisalkar, S. G.; Mathews, N. Precise Control of CsPbBr₃ Perovskite Nanocrystal Growth at Room Temperature: Size Tunability and Synthetic Insights. *Chemistry of Materials* **2021**, *33* (7), 2387–2397.
 - Almeida, G.; Ashton, O. J.; Goldoni, L.; Maggioni, D.; Petralanda, U.; Mishra, N.; Akkerman, Q. A.; Infante, I.; Snaith, H. J.; Manna, L. The Phosphine Oxide Route toward Lead Halide Perovskite Nanocrystals. *J Am Chem Soc* **2018**, *140* (44), 14878–14886.
 - Brown, A. A. M.; Damodaran, B.; Jiang, L.; Tey, J. N.; Pu, S. H.; Mathews, N.; Mhaisalkar, S. G. Lead Halide Perovskite Nanocrystals: Room Temperature Syntheses toward Commercial Viability. *Adv Energy Mater* **2020**, *10* (34), 2001349.
 - Huang, H.; Li, Y.; Tong, Y.; Yao, E.; Feil, M. W.; Richter, A. F.; Döblinger, M.; Rogach, A. L.; Feldmann, J.; Polavarapu, L. Spontaneous Crystallization of

- Perovskite Nanocrystals in Nonpolar Organic Solvents: A Versatile Approach for Their Shape-Controlled Synthesis. *Angewandte Chemie International Edition* **2019**, *58* (46), 16558–16562.
15. Wei, S.; Yang, Y.; Kang, X.; Wang, L.; Huang, L.; Pan, D. Homogeneous Synthesis and Electroluminescence Device of Highly Luminescent CsPbBr₃ Perovskite Nanocrystals. *Inorg Chem* **2017**, *56* (5), 2596–2601.
 16. Song, J.; Li, J.; Xu, L.; Li, J.; Zhang, F.; Han, B.; Shan, Q.; Zeng, H. Room-Temperature Triple-Ligand Surface Engineering Synergistically Boosts Ink Stability, Recombination Dynamics, and Charge Injection toward EQE-11.6% Perovskite QLEDs. *Advanced Materials* **2018**, *30* (30), 1800764.
 17. Akkerman, Q. A.; Nguyen, T. P. T.; Boehme, S. C.; Montanarella, F.; Dirin, D. N.; Wechsler, P.; Beiglböck, F.; Rainò, G.; Erni, R.; Katan, C.; Even, J.; Kovalenko, M. V. Controlling the Nucleation and Growth Kinetics of Lead Halide Perovskite Quantum Dots. *Science* **2022**, *377* (6613), 1406–1412.
 18. Kim, Y.-H.; Kim, S.; Kakekhani, A.; Park, J.; Park, J.; Lee, Y.-H.; Xu, H.; Nagane, S.; Wexler, R. B.; Kim, D.-H.; Jo, S. H.; Martínez-Sarti, L.; Tan, P.; Sadhanala, A.; Park, G.-S.; Kim, Y.-W.; Hu, B.; Bolink, H. J.; Yoo, S.; Friend, R. H.; Rappe, A. M.; Lee, T.-W. Comprehensive Defect Suppression in Perovskite Nanocrystals for High-Efficiency Light-Emitting Diodes. *Nat Photonics* **2021**, *15* (2), 148–155.
 19. Dhaene, E.; Billet, J.; Bennett, E.; van Driessche, I.; de Roo, J. The Trouble with ODE: Polymerization during Nanocrystal Synthesis. *Nano Lett* **2019**, *19* (10), 7411–7417.
 20. Papavassiliou, G. C. Three- and Low-Dimensional Inorganic Semiconductors. *Progress in Solid State Chemistry* **1997**, *25* (3–4), 125–270.
 21. Guvenc, C. M.; Balci, S. Seed-Mediated Synthesis of Colloidal 2D Halide Perovskite Nanoplatelets. *ChemNanoMat* **2021**, *7* (11).
 22. Weidman, M. C.; Seitz, M.; Stranks, S. D.; Tisdale, W. A. Highly Tunable Colloidal Perovskite Nanoplatelets through Variable Cation, Metal, and Halide Composition. *ACS Nano* **2016**, *10* (8), 7830–7839.
 23. Otero-Martínez, C.; Ye, J.; Sung, J.; Pastoriza-Santos, I.; Pérez-Juste, J.; Xia, Z.; Rao, A.; Hoyer, R. L. Z.; Polavarapu, L. Colloidal Metal-Halide Perovskite Nanoplatelets: Thickness-Controlled Synthesis, Properties, and Application in Light-Emitting Diodes. *Advanced Materials* **2022**, *34* (10), 2107105.

24. Guvenc, C. M.; Balci, S. Seed-Mediated Synthesis of Colloidal 2D Halide Perovskite Nanoplatelets. *ChemNanoMat* **2021**, *7* (11), 1249–1257.
25. Peng, L.; Dutta, A.; Xie, R.; Yang, W.; Pradhan, N. Dot–Wire–Platelet–Cube: Step Growth and Structural Transformations in CsPbBr₃ Perovskite Nanocrystals. *ACS Energy Lett* **2018**, *3* (8), 2014–2020.
26. Zhang, B.; Altamura, D.; Caliandro, R.; Giannini, C.; Peng, L.; de Trizio, L.; Manna, L. Stable CsPbBr₃ Nanoclusters Feature a Disk-like Shape and a Distorted Orthorhombic Structure. *J Am Chem Soc* **2022**, *144* (11), 5059–5066.
27. Pun, A. B.; Mazzotti, S.; Mule, A. S.; Norris, D. J. Understanding Discrete Growth in Semiconductor Nanocrystals: Nanoplatelets and Magic-Sized Clusters. *Acc Chem Res* **2021**, *54* (7), 1545–1554.
28. Mehetor, S. K.; Ghosh, H.; Pradhan, N. Acid–Amine Equilibria for Formation and Long-Range Self-Organization of Ultrathin CsPbBr₃ Perovskite Platelets. *J Phys Chem Lett* **2019**, *10* (6), 1300–1305.
29. Cho, J.; Choi, Y. H.; O’Loughlin, T. E.; de Jesus, L.; Banerjee, S. Ligand-Mediated Modulation of Layer Thicknesses of Perovskite Methylammonium Lead Bromide Nanoplatelets. *Chemistry of Materials* **2016**, *28* (19).
30. Kumar, S.; Jagielski, J.; Marcato, T.; Solari, S. F.; Shih, C.-J. Understanding the Ligand Effects on Photophysical, Optical, and Electroluminescent Characteristics of Hybrid Lead Halide Perovskite Nanocrystal Solids. *J Phys Chem Lett* **2019**, *10* (24), 7560–7567.
31. Pan, A.; He, B.; Fan, X.; Liu, Z.; Urban, J. J.; Alivisatos, A. P.; He, L.; Liu, Y. Insight into the Ligand-Mediated Synthesis of Colloidal CsPbBr₃ Perovskite Nanocrystals: The Role of Organic Acid, Base, and Cesium Precursors. *ACS Nano* **2016**, *10* (8), 7943–7954.
32. Bhosale, S. S.; Narra, S.; Jokar, E.; Manikandan, A.; Chueh, Y. L.; Diao, E. W. G. Functionalized Hybrid Perovskite Nanocrystals with Organic Ligands Showing a Stable 3D/2D Core/Shell Structure for Display and Laser Applications. *J Mater Chem C Mater* **2021**, *9* (48), 17341–17348.
33. Murray, C. B.; Norris, D. J.; Bawendi, M. G. Synthesis and Characterization of Nearly Monodisperse CdE (E = Sulfur, Selenium, Tellurium) Semiconductor Nanocrystallites. *J Am Chem Soc* **1993**, *115* (19), 8706–8715.
34. di Stasio, F.; Imran, M.; Akkerman, Q. A.; Prato, M.; Manna, L.; Krahne, R. Reversible Concentration-Dependent Photoluminescence Quenching and Change

- of Emission Color in CsPbBr₃ Nanowires and Nanoplatelets. *Journal of Physical Chemistry Letters* **2017**, *8* (12), 2725–2729.
35. Krieg, F.; Sercel, P. C.; Burian, M.; Andrusiv, H.; Bodnarchuk, M. I.; Stöferle, T.; Mahrt, R. F.; Naumenko, D.; Amenitsch, H.; Rainò, G.; Kovalenko, M. v. Monodisperse Long-Chain Sulfobetaine-Capped CsPbBr₃ Nanocrystals and Their Superfluorescent Assemblies. *ACS Cent Sci* **2021**, *7* (1), 135–144.
 36. Nasipuri, D.; Patra, A.; Bera, S.; Dutta, S. K.; Pradhan, N. Nucleophile-Controlled Halide Release from the Substitution Reaction of Haloketone for Facet Tuning and Manganese Doping in CsPbCl₃ Nanocrystals. *J Phys Chem Lett* **2022**, *13* (20), 4506–4512.
 37. Zhang, B.; Goldoni, L.; Zito, J.; Dang, Z.; Almeida, G.; Zaccaria, F.; de Wit, J.; Infante, I.; de Trizio, L.; Manna, L. Alkyl Phosphonic Acids Deliver CsPbBr₃ Nanocrystals with High Photoluminescence Quantum Yield and Truncated Octahedron Shape. *Chemistry of Materials* **2019**, *31* (21), 9140–9147.
 38. Hudait, B.; Dutta, S. K.; Pradhan, N. Isotropic CsPbBr₃ Perovskite Nanocrystals beyond Nanocubes: Growth and Optical Properties. *ACS Energy Lett* **2020**, *5* (2), 650–656.
 39. Nenon, D. P.; Pressler, K.; Kang, J.; Koscher, B. A.; Olshansky, J. H.; Osowiecki, W. T.; Koc, M. A.; Wang, L.-W.; Alivisatos, A. P. Design Principles for Trap-Free CsPbX₃ Nanocrystals: Enumerating and Eliminating Surface Halide Vacancies with Softer Lewis Bases. *J Am Chem Soc* **2018**, *140* (50), 17760–17772.
 40. Ravi, V. K.; Markad, G. B.; Nag, A. Band Edge Energies and Excitonic Transition Probabilities of Colloidal CsPbX₃ (X = Cl, Br, I) Perovskite Nanocrystals. *ACS Energy Letters* **2016**, *1* (4), 665–671.
 41. Kumawat, N. K.; Tripathi, M. N.; Waghmare, U.; Kabra, D. Structural, Optical, and Electronic Properties of Wide Bandgap Perovskites: Experimental and Theoretical Investigations. *J Phys Chem A* **2016**, *120* (22), 3917–3923.
 42. Imran, M.; Caligiuri, V.; Wang, M.; Goldoni, L.; Prato, M.; Krahne, R.; de Trizio, L.; Manna, L. Benzoyl Halides as Alternative Precursors for the Colloidal Synthesis of Lead-Based Halide Perovskite Nanocrystals. *J Am Chem Soc* **2018**, *140* (7).
 43. Ahmed, G. H.; El-Demellawi, J. K.; Yin, J.; Pan, J.; Velusamy, D. B.; Hedhili, M. N.; Alarousu, E.; Bakr, O. M.; Alshareef, H. N.; Mohammed, O. F. Giant

- Photoluminescence Enhancement in CsPbCl₃ Perovskite Nanocrystals by Simultaneous Dual-Surface Passivation. *ACS Energy Lett* **2018**, *3* (10), 2301–2307.
44. Zhang, C.; Wan, Q.; Ono, L. K.; Liu, Y.; Zheng, W.; Zhang, Q.; Liu, M.; Kong, L.; Li, L.; Qi, Y. Narrow-Band Violet-Light-Emitting Diodes Based on Stable Cesium Lead Chloride Perovskite Nanocrystals. *ACS Energy Lett* **2021**, *6* (10), 3545–3554.
45. Lignos, I.; MacEiczyk, R. M.; Kovalenko, M. v.; Stavrakis, S. Tracking the Fluorescence Lifetimes of Cesium Lead Halide Perovskite Nanocrystals during Their Synthesis Using a Fully Automated Optofluidic Platform. *Chemistry of Materials* **2020**, *32* (1), 27–37.
46. Guvenc, C. M.; Tunc, I.; Balci, S. L₂[GAXFA1–XPbI₃]PbI₄ (0 ≤ x ≤ 1) Ruddlesden–Popper Perovskite Nanocrystals for Solar Cells and Light-Emitting Diodes. *ACS Appl Nano Mater* **2022**, *5* (1), 1078–1085.
47. Guvenc, C. M.; Polat, N.; Balci, S. Strong Plasmon-Exciton Coupling in Colloidal Halide Perovskite Nanocrystals near a Metal Film. *J Mater Chem C Mater* **2020**, *8* (46), 16520–16526.
48. Imran, M.; Caligiuri, V.; Wang, M.; Goldoni, L.; Prato, M.; Krahne, R.; de Trizio, L.; Manna, L. Benzoyl Halides as Alternative Precursors for the Colloidal Synthesis of Lead-Based Halide Perovskite Nanocrystals. *J Am Chem Soc* **2018**, *140* (7), 2656–2664.
49. Dutta, A.; Behera, R. K.; Pal, P.; Baitalik, S.; Pradhan, N. Near-Unity Photoluminescence Quantum Efficiency for All CsPbX₃ (X=Cl, Br, and I) Perovskite Nanocrystals: A Generic Synthesis Approach. *Angewandte Chemie* **2019**, *131* (17), 5608–5612.
50. Yuan, L.; Sun, X.; Zhang, X.; Li, F.; Liu, Y.; Gao, Y.; Qian, H.; Liu, Z.; Ma, W. Targeted Design of Surface Configuration on CsPbI₃ Perovskite Nanocrystals for High-Efficiency Photovoltaics. *ACS Energy Lett* **2023**, *8*, 241–249.
51. Stoumpos, C. C.; Malliakas, C. D.; Peters, J. A.; Liu, Z.; Sebastian, M.; Im, J.; Chasapis, T. C.; Wibowo, A. C.; Chung, D. Y.; Freeman, A. J.; Wessels, B. W.; Kanatzidis, M. G. Crystal Growth of the Perovskite Semiconductor CsPbBr₃: A New Material for High-Energy Radiation Detection. *Cryst Growth Des* **2013**, *13* (7), 2722–2727.

52. Straus, D. B.; Guo, S.; Cava, R. J. Kinetically Stable Single Crystals of Perovskite-Phase CsPbI₃. *J Am Chem Soc* **2019**, *141* (29), 11435–11439.
53. Fu, Y.; Hautzinger, M. P.; Luo, Z.; Wang, F.; Pan, D.; Aristov, M. M.; Guzei, I. A.; Pan, A.; Zhu, X.; Jin, S. Incorporating Large A Cations into Lead Iodide Perovskite Cages: Relaxed Goldschmidt Tolerance Factor and Impact on Exciton-Phonon Interaction. *ACS Cent Sci* **2019**, *5* (8), 1377–1386.
54. Goldschmidt, V. M. Die Gesetze Der Krystallochemie. *Naturwissenschaften* **1926**, *14* (21), 477–485.
55. Shannon, R. D. Revised Effective Ionic Radii and Systematic Studies of Interatomic Distances in Halides and Chalcogenides. *Acta Crystallographica Section A* **1976**, *32* (5), 751–767.
56. Guodong, F.; Mingming, G.; Qi, L.; Hongyu, M.; Guanghua, L.; Qiang, M.; Qiang, F.; Yanfu, H.; Zhiguang, S. One-Pot Synthesis and Application of Novel Amino-Functionalized Silica Nanoparticles Using Guanidine as Amino Group. *New Journal of Chemistry* **2016**, *40* (10), 8444–8450.
57. Erazo, E. A.; Sánchez-Godoy, H. E.; Gualdrón-Reyes, A. F.; Masi, S.; Mora-Seró, I. Photo-Induced Black Phase Stabilization of CsPbI₃ QDs Films. *Nanomaterials* **2020**, *10* (8), 1586.
58. Liu, Q.; Yin, J.; Zhang, B. bin; Chen, J. K.; Zhou, Y.; Zhang, L. M.; Wang, L. M.; Zhao, Q.; Hou, J.; Shu, J.; Song, B.; Shirahata, N.; Bakr, O. M.; Mohammed, O. F.; Sun, H. T. Theory-Guided Synthesis of Highly Luminescent Colloidal Cesium Tin Halide Perovskite Nanocrystals. *J Am Chem Soc* **2021**, *143* (14), 5470–5480.
59. Shi, Y.; Yuan, L.; Liu, Z.; Lu, Y.; Yuan, B.; Shen, W.; Xue, B.; Zhang, Y.; Qian, Y.; Li, F.; Zhang, X.; Liu, Y.; Wang, Y.; Wang, L.; Yuan, J.; Liao, L. S.; Yang, B.; Yu, Y.; Ma, W. In Situ Growth of Strained Matrix on CsPbI₃ Perovskite Quantum Dots for Balanced Conductivity and Stability. *ACS Nano* **2022**, *16* (7), 10534–10544.

CHAPTER 4

BREAKING THE BOUNDARIES OF THE GOLDSCHMIDT TOLERANCE FACTOR WITH ETHYLAMMONIUM LEAD IODIDE PEROVSKITE NANOCRYSTALS

The following chapter is written in the format of a manuscript and has been accepted by
ACS Nano.

Abstract

We report the synthesis of ethylammonium lead iodide (EAPbI₃) colloidal nanocrystals as a new member of the lead halide perovskites family. The insertion of an unusually large A-cation (274 pm in diameter) in the perovskite structure, hitherto considered unlikely due to the unfavorable Goldschmidt tolerance factor, results in a significantly larger lattice parameter compared to the Cs-, methylammonium- and formamidinium-based lead halide perovskite homologues. As a consequence, EAPbI₃ nanocrystals are remarkably unstable, evolving to a non-perovskite EAPbI₃ polymorph within one day. Also, EAPbI₃ nanocrystals are very sensitive to electron beams and quickly degrade to PbI₂ upon exposure to the electron beam, following a mechanism similar to that of other hybrid lead iodide perovskites (the degradation can be reduced by partially replacing the EA⁺ ions with Cs⁺ ions). Interestingly, in some cases during this degradation the formation of an epitaxial interface between (EA_xCs_{1-x})PbI₃ and PbI₂ is observed. The photoluminescence emission of the EAPbI₃ perovskite nanocrystals, albeit being characterized by a low quantum yield (~1%), can be tuned in the 664-690 nm range by regulating their size during the synthesis. The emission efficiency can be improved upon partial alloying at the A site with Cs⁺ or formamidinium cations. Furthermore, the morphology of the EAPbI₃ nanocrystals can be chosen to be either nanocube or nanoplatelet, depending on the synthesis conditions.

4.1. Introduction

Lead halide perovskites are a family of direct-gap semiconductors widely investigated as low-cost and high efficiency materials for light emission and harvesting applications.¹⁻⁴ For the latter applications, the most promising compositions are the iodine-based APbI₃ perovskites, where the A site can be occupied by a variety of organic or inorganic monovalent cations. Despite offering high carrier mobility and a nearly ideal gap for solar cells, real-world applications of iodine-based perovskites are hindered by their intrinsic lability, which prompted research into improving the stability of these materials via either cation- or halide-alloying.³⁻⁷

Following this lead, different A⁺ cations have been investigated in the attempt to modulate the stability and the properties of lead-iodide perovskites by leveraging the size of cations to influence the Goldschmidt tolerance factor.^{5,7-9} The APbI₃ perovskite structure can form with the A⁺ cation being Cs⁺ (ionic radius = 188 pm),¹⁰ methylammonium (MA⁺ = 217)¹¹, formamidinium (FA⁺ = 253 pm)¹², and the recently reported aziridinium (AZ⁺ = 227 pm).^{13,14} All these APbI₃ perovskite phases are generally unstable under ambient conditions and tend to transform into non-perovskite polymorphs or to degrade (for example to PbI₂ and MAI in the case of MAPbI₃) over time.^{12,15} While some of these phases, like CsPbI₃ and FAPbI₃, are reasonably durable, the use of significantly smaller or larger cations than MA⁺ results in more labile phases.¹² Indeed, recent synthesis attempts with dimethylammonium (272 pm), guanidinium (279 pm), and acetamidinium (284 pm) have resulted in the formation of Ruddlesden-Popper phases instead of the perovskite one.¹⁶⁻¹⁸

Materials that are unattainable in bulk form can however be at times synthesized as nanocrystals, even if only transiently, by exploiting the relaxed structural constraints guaranteed by the finite size of the crystalline domains.¹⁹ Here, we demonstrate the colloidal synthesis of ethylammonium based lead iodide (EAPbI₃) perovskite NCs, which display a remarkably high lattice parameter (6.43 Å), and a Goldschmidt factor (1.03) that is outside the boundaries generally considered tolerable for a perovskite phase. Like other lead-halide perovskites, EAPbI₃ NCs adopt a cuboidal morphology and display photoluminescence in the 664 - 690 nm range depending on the NCs size. As expected, these EAPbI₃ NCs were found to be rather unstable, with their recrystallization to a non-

perovskite polymorph starting within ~2h and generally becoming complete within one day, similar to what observed for other APbI₃ perovskite phases.^{12,15} The low quantum yield values of these EAPbI₃ NCs compared to other APbI₃ perovskite NCs¹³ are likely a consequence of such lability, which might foster the formation of defects and hence trap states. The EAPbI₃ perovskite NCs are also extremely sensitive to an electron beam and can degrade to PbI₂ even at small irradiation doses, making their characterization challenging. This stability issue can be mitigated by partially replacing EA⁺ with Cs⁺. Remarkably, this replacement also leads to the formation of (EA_xCs_{1-x})PbI₃ heterostructures, similar to those found for FAPbI₃ thin films.^{20,21} Partial alloying of EA⁺ ions with Cs⁺ or FA cations increases the PL quantum yield of the NCs and induces a spectral red shift, compatible with a band gap narrowing. Notably, the EAPbI₃ NCs become more stable when prepared in the form of ultrathin, highly confined nanoplatelets, an effect that is likely due to the relaxation of structural constraints due to their finite thickness, which allows the lattice to cope with the distortions induced by the large size of the EA⁺ cation.

4.2. Results and Discussion

The EAPbI₃ NCs were synthesized at room temperature by reacting a PbI₂ solution with EA-oleate. In short, PbI₂ was dissolved in a mixture of oleylamine and oleic acid in the presence of oleylammonium iodide at 140 °C. Upon cooling, toluene was added to prevent a gel formation at room temperature. Thereafter, EAPbI₃ NCs were synthesized by injecting EA-oleate and oleic acid in the PbI₂ solution at room temperature. Alternatively, PbI₂ could be dissolved in trioctylphosphine oxide (TOPO) at 140 °C,^{23,24} It should be noted that TOPO is solid at room temperature, and melts only above 70 °C. This limitation can be circumvented by adding toluene to prevent solidification upon cooling the reaction to room temperature. Similarly, to synthesize EAPbI₃ perovskite NCs oleylammonium iodide, oleylamine, and oleic acid should be added to TOPO-PbI₂ solution. (see the Methods section for detailed synthetic protocols). The size of the colloidal EAPbI₃ perovskite NCs could be tuned between 7.1 nm and 17.5 nm depending on the amount of oleic acid added in the synthesis, resulting in tunable photoluminescence (PL) in the 664 – 690 nm range (Figure 4.1a-c and Figure 4.2). It should be noted that the EAPbI₃ perovskite NCs had weak PL (quantum yield ~1%) and multiexponential PL decay with 1/e lifetime of 37 ns (see Figure 4.3). We note that

EAPbI₃ NCs obtained by the two methods described above displayed comparable optical, structural, and morphological properties (see Figure 4.4). Low-magnification transmission electron microscopy (TEM) images of EAPbI₃ NCs evidenced a generally irregular morphology for the NCs, although many of them had cuboidal shape, similar to that of more conventional lead halide perovskite NCs (Figure 1d).

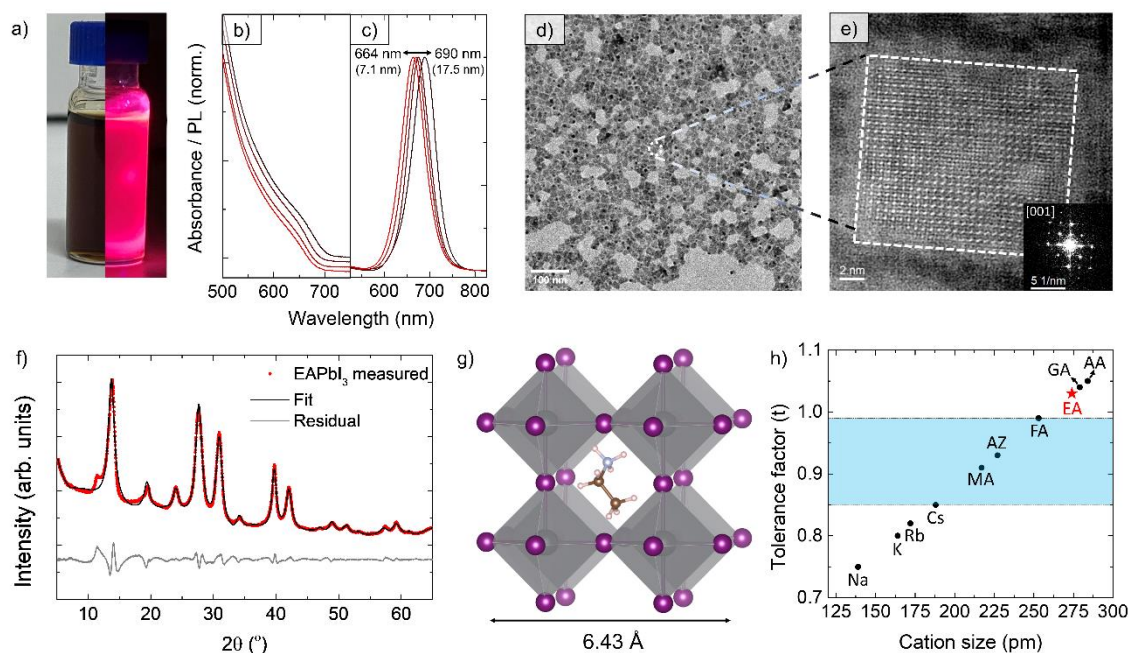


Figure 4.1. Optical and structural features of EAPbI₃ NCs. (a) A colloidal NCs suspension under indoor and UV illumination. (b) Optical absorption and (c) photoluminescence spectra of EAPbI₃ NCs of different sizes. (d) Bright field TEM image of EAPbI₃ NCs. (e) HAADF HR-STEM image of an individual NC. Inset: Fourier transform of the lattice-resolved image, compatible with a pseudocubic perovskite structure seen along its [100] zone axis. Note that the sample was alloyed with $\sim 12\%$ Cs⁺ to enhance the stability under the electron beam. (f) X-ray diffraction pattern of EAPbI₃ NCs, fitted assuming an R-3c distorted perovskite structure (Le Bail method). (g) Representation of the pseudocubic EAPbI₃ crystal structure, with the ethylammonium cation positioned at the center of the cage formed by six [PbI₆]⁴⁻ octahedra. (h) Goldschmidt tolerance factor for APbI₃ perovskites with different A cations (MA = methylammonium,¹¹ AZ = aziridinium,¹³ FA = formamidinium,¹² GA = guanidinium^{17,22} and, AA = acetamidinium¹⁷). Lead-iodide perovskites obtained experimentally to date are enclosed by the area shown in blue.

High-angle annular dark-field scanning TEM (HAADF-STEM) imaging supported the assignment of a perovskite crystal structure, with the Fourier transform of the lattice displaying a 4-fold symmetry compatible with a perovskite lattice (Figure 4.1e). In agreement with electron microscopy, the XRD pattern of the EAPbI₃ NCs was compatible with a pseudocubic perovskite structure with a lattice constant of 6.43 Å (Figure 4.1e-g). This makes EAPbI₃ the lead halide perovskite with the largest lattice constant reported to date, despite a Goldschmidt tolerance factor of 1.03, which is well outside the expected stability range (Figure 4.1h).^{12,16,17}

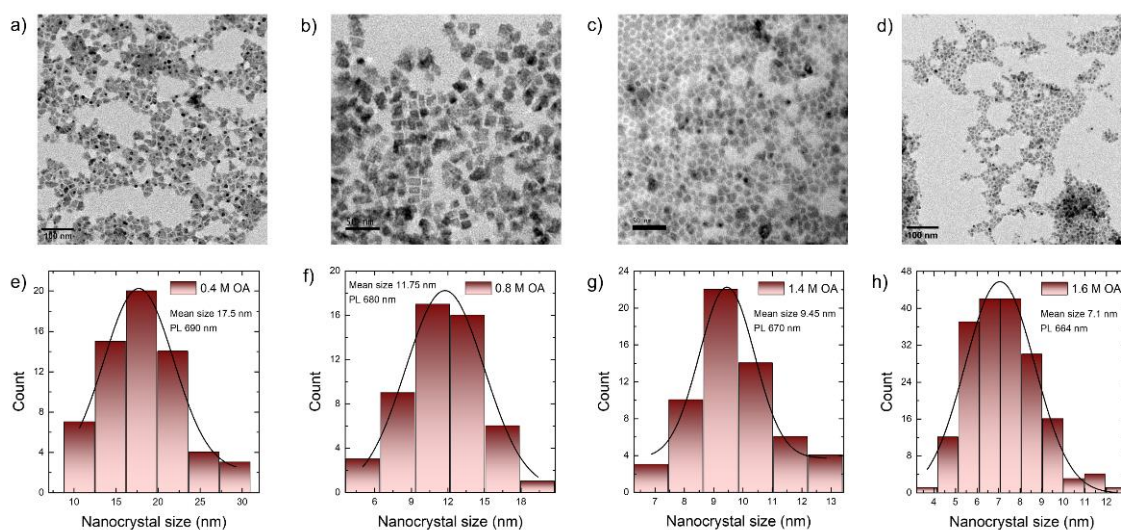


Figure 4.2. (a, b, c, d) TEM images of the EAPbI₃ perovskite nanocrystals, which contain 0.4 M, 0.8 M, 1.4 M, and 1.6 M OA in the final solution, and (d, e, f, h) their related particle size distributions, respectively.

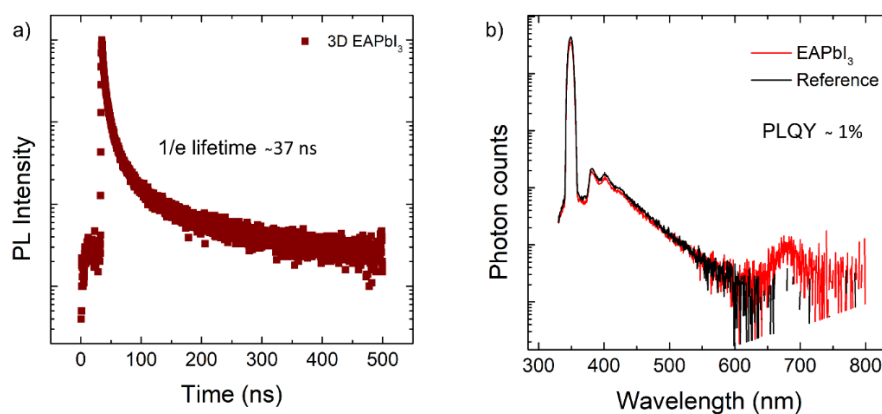


Figure 4.3. (a) PL intensity decay curve and (b) spectra recorded for PLQY measurement of EAPbI₃ perovskite nanocrystals.

In-depth analysis of the XRD pattern highlighted small discrepancies between the position of the peaks and the cubic indexing, while the ideal perovskite structure provides a close fit to the observed XRD profile, a lower-symmetry R-3c structure provides a better fit, suggesting a mild distortion from the cubic structure (Figure 4.1e). We note that such deviation is quite minor, and the peak broadening due to the nano-size of particles prevents a definitive identification of the space group. Here, our choice of fitting with the R-3c group involves using a proxy structure to qualitatively understand the effect of lattice distortions on the XRD profile (see Figure 4.5). The shoulder at a 2θ value of 11.5° is likely due to the presence of an unidentified byproduct, albeit in small amounts.

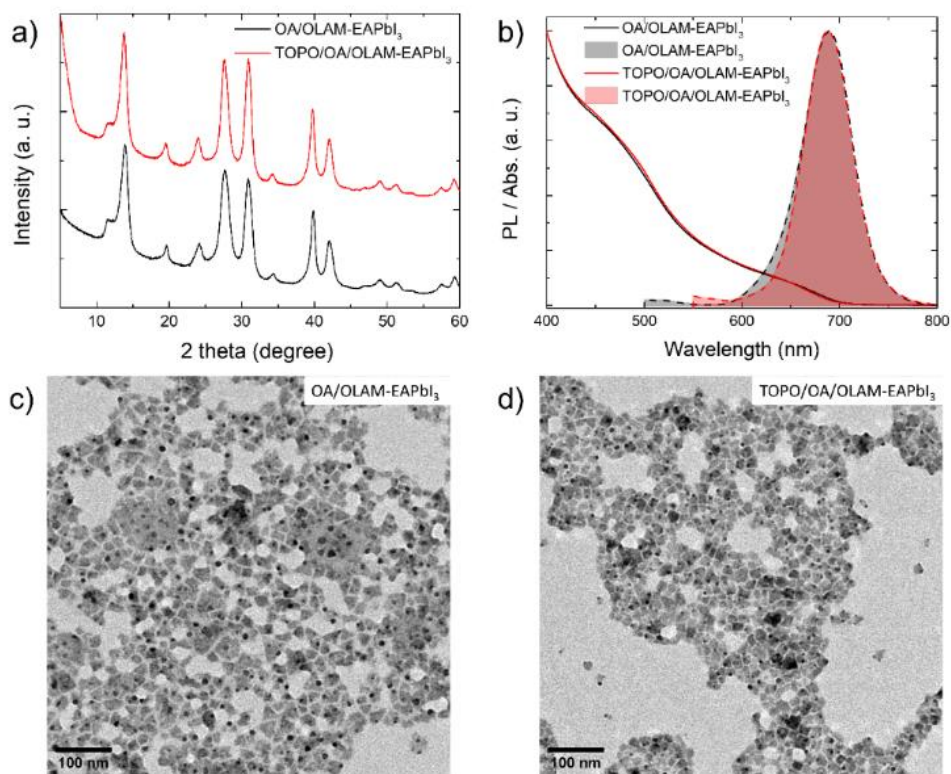


Figure 4.4. Comparison of the absorption, PL spectra, TEM images, and XRD patterns of the EAPbI₃ NCs synthesized with two methods used in this study. XRD patterns, absorption, PL spectra, and morphology of the EAPbI₃ NCs are very similar for both methods.

In the attempt to further investigate such distortions and gain insights into the electronic structure of EAPbI₃ we resorted to density functional theory (DFT) calculations. First, we exploited simulated annealing molecular dynamics to generate 11 low-energy configurations that differed by the position of EA cations, and consequently by the degree of distortion of the Pb-I scaffold (representative examples shown in Figure 4.6).

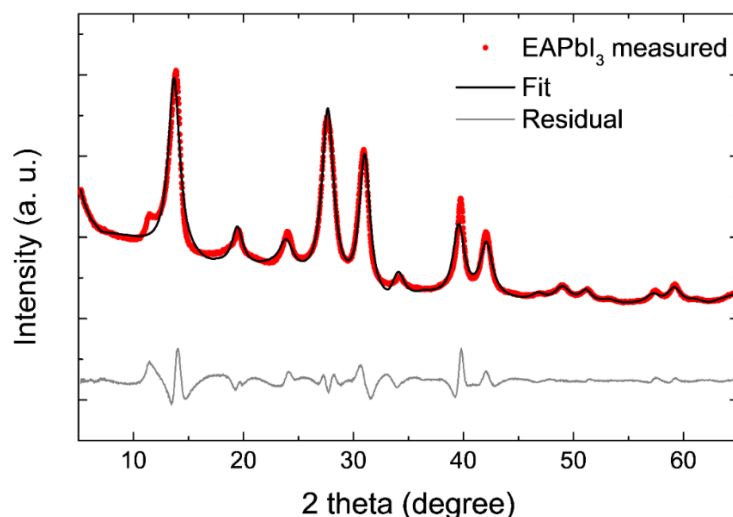


Figure 4.5. Experimental XRD data of the EAPbI₃ perovskite fitted with the cubic prototype.

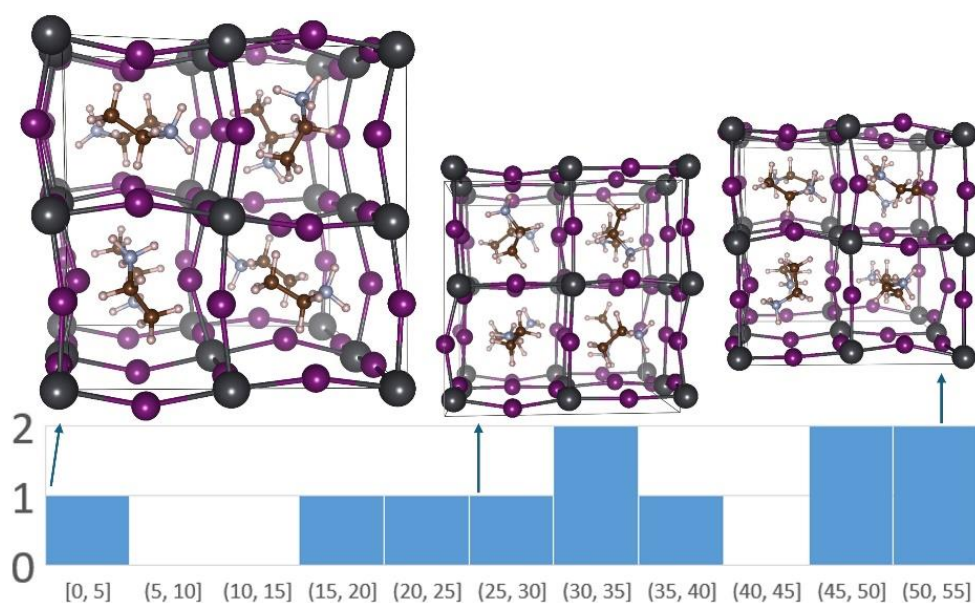


Figure 4.6. Histogram showing the energy distribution (meV/formula unit) of the 11 EAPbI₃ configurations obtained through simulated annealing. Representative configurations are shown. the larger, left most one is the lowest-energy structure (putative structural ground state) obtained. Color code for atoms as follows. Pb= grey, I=violet, C=brown, N=blue, H=white.

All of the obtained configurations lie within a fairly narrow energy range of 55 meV/formula unit (f.u.), 36% of them being within 26 meV/f.u. (that is, $k_B T$ at 298 K,

see Figure 6). Given that there is a vast number of possible ways in which EA cations can be arranged, the small energy difference among the configurations sampled by DFT suggests that many configurations will be populated at room temperature. Within this scenario, we interpret the pseudocubic structure of EAPbI₃ as a dynamic average of many local configurations, similarly to what has been reported for methylammonium lead halide perovskites.²⁷ Such dynamic variability likely has a wide impact on the band gap of EAPbI₃, with up to 0.44 eV difference among the configurations inspected. This possibly contributes to the broadening of the excitonic features seen in Figure 4.1b. Various works on other lead-iodide perovskite phases have reported that the degree of distortion of the Pb-X sublattice can be adopted, in principle, to predict the band gap^{28,26,27}. On the other hand, we did not find significant correlations (*i.e.* $R^2 \leq 0.32$) between the band gap and any of the tested measures of distortion, including those commonly adopted in the literature (Figure 4.7).

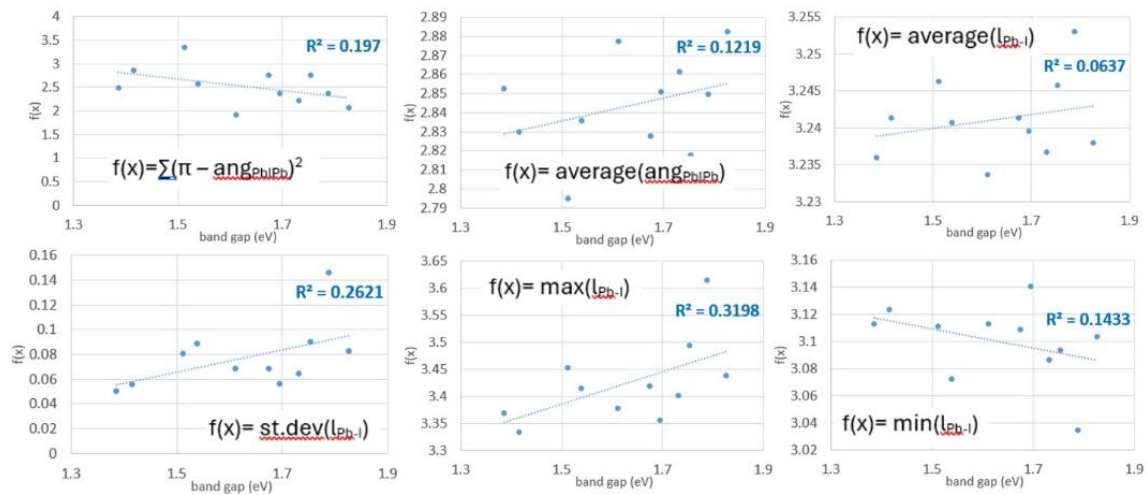


Figure 4.7. Plots of the band gap vs various measures of Pb-I sublattice distortion for the 11 studied EAPbI₃ configurations. For each plot, the function reported on the vertical axis is shown in black inside the plot. $\text{ang}_{\text{PbI}_2}$ is the angle formed by Pb with two bonded I atoms, and $l_{\text{Pb-I}}$ is the Pb-I bond length. The Pearson correlation coefficient squared (R^2) is reported in blue in each plot.

Finally, we note that the electronic structure of EAPbI₃ is typical of a lead halide perovskite phase, with valence and conduction bands formed by Pb(6s)-I(5p) and Pb(6p)-I(5p) antibonding orbitals, respectively (Figure 4.8).^{25,28,29}

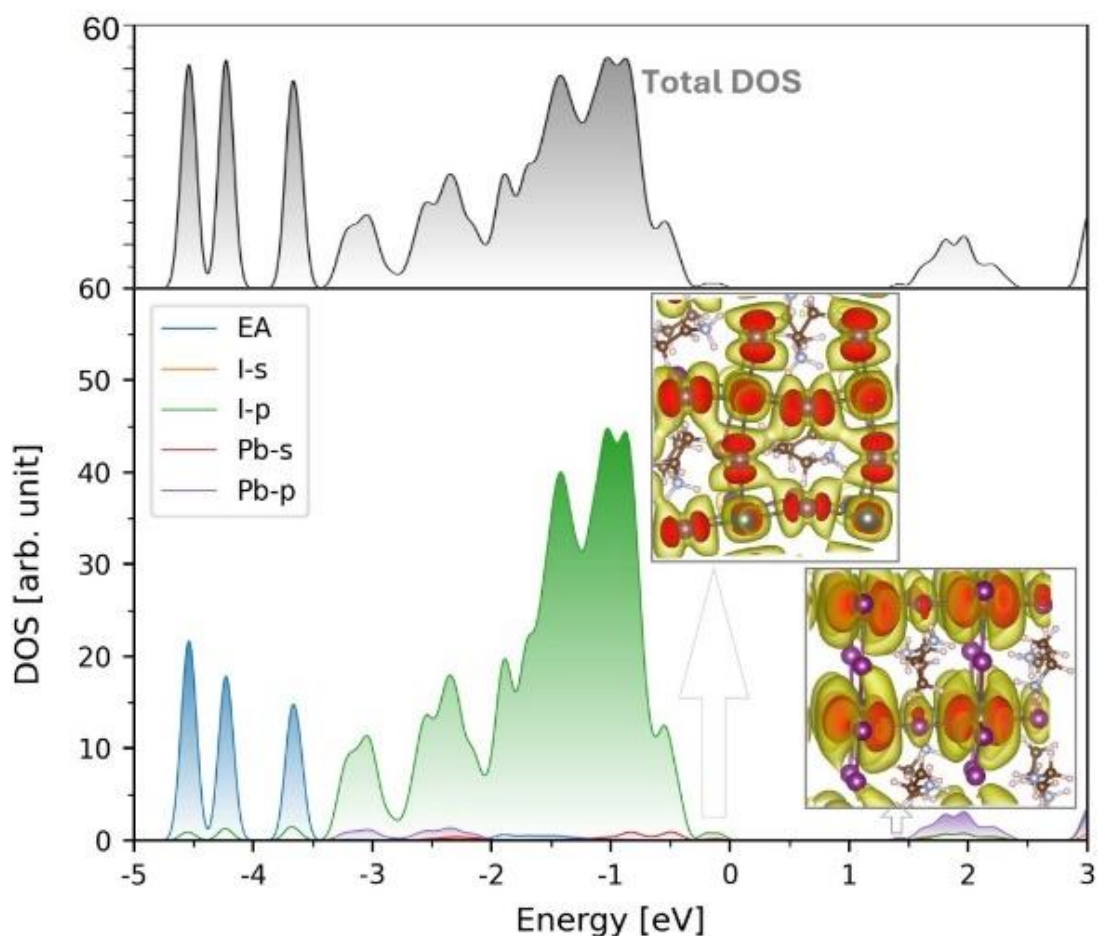


Figure 4.8. Density of states (DOS) and partial charge density for EAPbI₃ (lowest-energy configuration). The top plot reports the total DOS, while the bottom plot shows the atomic orbital-projected contributions, color legend on the top left. The charge density corresponding to the valence band maximum (from -0.25 eV to Fermi level) and conduction band minimum (from Fermi level to +1.5 eV) are reported in the insets as yellow and red isosurfaces (isovalues, in VASP units: 5×10^{-5} and 5×10^{-4} for valence and 1×10^{-5} and 1×10^{-4} for conduction). Color code same as in Figure 4.6.

As mentioned above, the large ionic radius of EA (274 pm) makes EAPbI₃ NCs quite unstable, possibly more than previously reported APbI₃ phases (A = Cs⁺, MA, FA, AZ, see Figure 1g).^{20,30} Indeed, the EAPbI₃ NCs spontaneously converted to a non-perovskite polymorph, here denoted as δ -EAPbI₃ (Figure 4.9) in analogy with the nomenclature adopted for CsPbI₃^{1,12,15,31,32}.

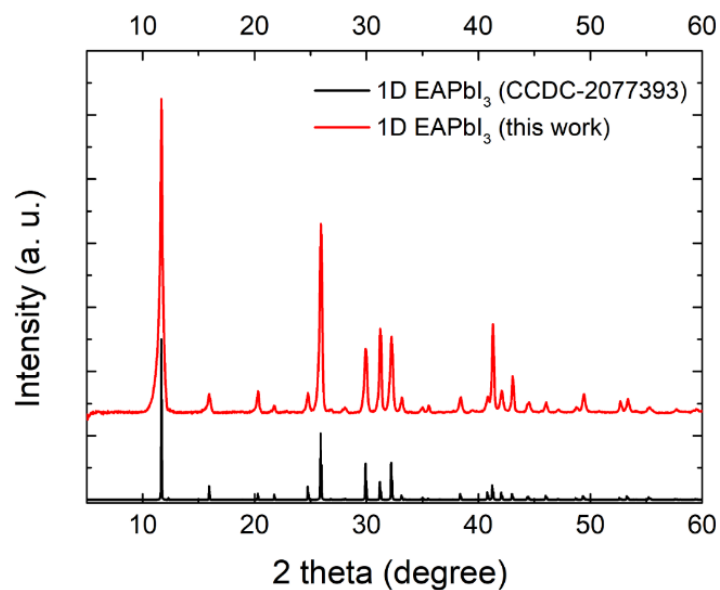


Figure 4.9. Comparison of the 1D EAPbI₃ crystals synthesized in this work and reference 1D EAPbI₃ (CCDC-2077393) XRD patterns

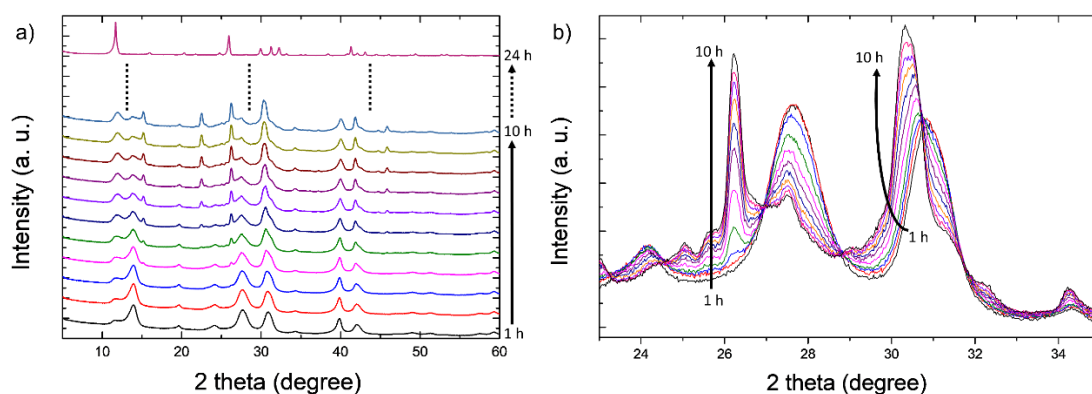


Figure 4.10. (a, b) The time-dependent XRD measurements of the EAPbI₃ perovskite nanocrystals. XRD analysis demonstrates that phase transformation starts after 2 hours in the drop-cast films of the EAPbI₃ nanocrystals under ambient conditions. After 24 hours, the EAPbI₃ perovskite phase completely transforms to δ - EAPbI₃ phase. (b) It is obvious that peak intensities change even 10 hours later, and phase transformation was not complete.

Time-dependent XRD analysis (Figure 4.10) showed that the transformation starts about 2 h after the sample was drop-cast in ambient conditions, and is complete after \sim 1

day. In some cases, other degradation products were observed, which we interpret as the formation of layered lead halide phases where either EA or excess oleylammonium served as a spacing cation (Figure 4.11).

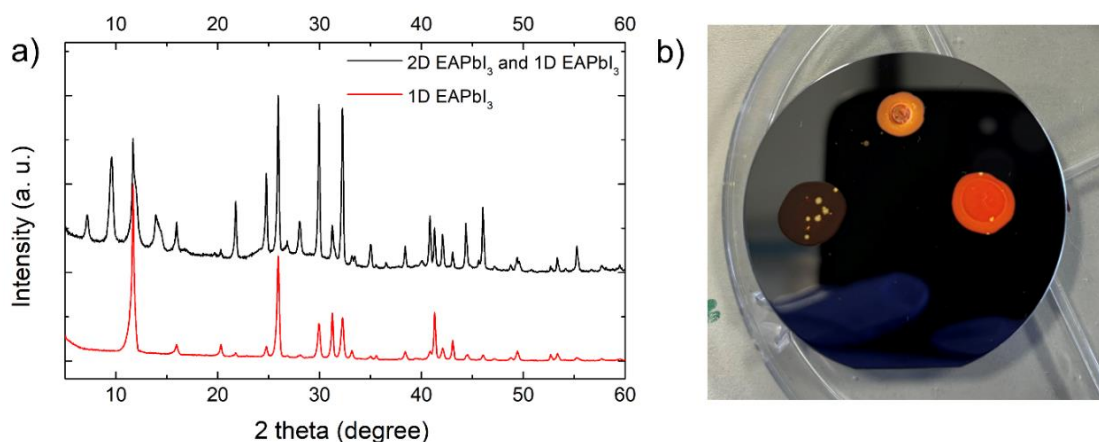


Figure 4.11. (a) Transformation of the EAPbI₃ perovskite phase to both 2D structures and the 1D EAPbI₃ simultaneously. Repetitive peaks at the low angle indicate the formation of 2D structures. Further, peaks at 11° and 26° indicate the formation of 1D EAPbI₃ in the black line. The red line demonstrates pure 1D EAPbI₃. (b) Digital images of the drop cast films in the case of the transformation from 3D EAPbI₃ to 2D and 1D EAPbI₃. The film's color was changed from black to orange. Also, it is possible to see some yellow spots related to 1D EAPbI₃ formation in the digital image.

Notably, transformations in halide perovskite NCs are also easily triggered by exposure to an electron beam in a TEM, which indeed in the present case induced the transformation of EAPbI₃ into PbI₂, similar to what was reported by Rothmann et al. for FAPbI₃.^{20,21} Pristine EAPbI₃ NCs were converted so quickly that the transformation could not be followed, and only the product PbI₂ nanoparticles could be imaged (Figure 4.12c). To slow down such degradation, we therefore replaced ~12% of the EA cations with Cs⁺ cations via post-synthesis cation exchange to stabilize the NCs during the acquisition of the HAADF-STEM images, including the one shown in Figure 4.12c (see Methods). The concentration of Cs⁺ was estimated from XRD by using the Vegard law³⁵, as discussed in the next section. Interestingly, the slower degradation of such Cs⁺-doped particles (Figure

4.12b) allowed to gain insight into the $\text{EAPbI}_3 \rightarrow \text{PbI}_2$ transformation mechanism.

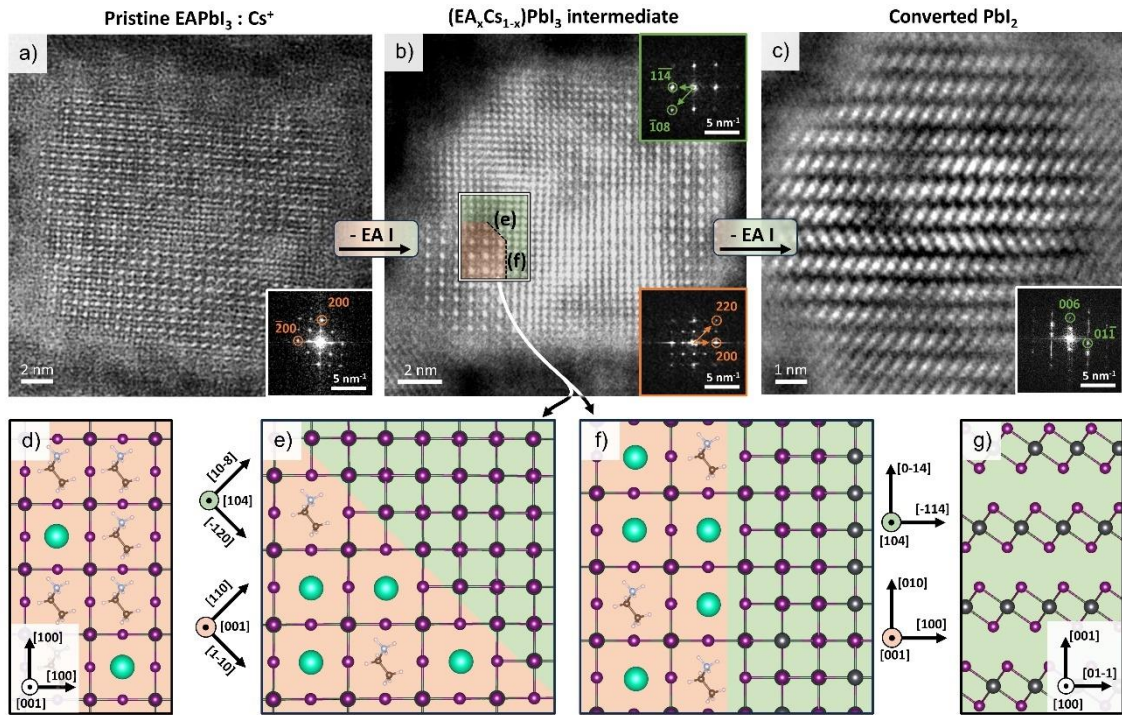


Figure 4.12. $\text{EAPbI}_3 \rightarrow \text{PbI}_2$ degradation mechanism under the electron beam. (a) HAADF-STEM images of a pristine $\text{EAPbI}_3:\text{Cs}^+$ NC. (b) Partially degraded $(\text{EA}_x\text{Cs}_{1-x})\text{PbI}_3/\text{PbI}_2$ heterostructure, formed as an intermediate while EAI leaves the NC and Cs^+ concentrates in the remaining pristine perovskite domains. (c) Fully transformed PbI_2 NC, still reminiscent of the initial cuboidal morphology of the perovskite NC. (d-g) Structure models of EAPbI_3 (d), PbI_2 (g) and of the $(\text{EA}_x\text{Cs}_{1-x})\text{PbI}_3/\text{PbI}_2$ epitaxial interface in two different directions (e,f). The co-presence of Cs^+ and EA^+ cations represents the alloyed nature of perovskite domain (see Figure 4.14 for further discussion).

The reaction proceeds through the formation of intermediate $(\text{EA}_x\text{Cs}_{1-x})\text{PbI}_3/\text{PbI}_2$ heterostructures (Figure 4.12b) and is favored by a non-trivial epitaxial relation between the perovskite and PbI_2 , as proposed in Figure 4.12e-f, which we identified using the Ogrpython library for the prediction of epitaxial interfaces (see Figure 4.13).^{34–36} This is in line with prior observations on the reactivity of lead halide perovskite NCs, which proceeds through reaction intermediates where reagent and product share an epitaxial relation.²⁰ As the reaction proceeds, the Cs^+ initially present as a minority cation is expelled from areas transformed into PbI_2 , and being less volatile than EA^+ it eventually

accumulates into $(\text{EA}_x\text{Cs}_{1-x})\text{PbI}_3$ domains, which are the last ones to be converted (see Figure 4.14 for additional analyses and differential phase-contrast images of the $(\text{EA}_x\text{Cs}_{1-x})\text{PbI}_3/\text{PbI}_2$ interface).

The stability enhancement achieved by partially replacing EA cations with Cs^+ cations prompted us to explore $(\text{EA}_x\text{FA}_{1-x})\text{PbI}_3$ and $(\text{EA}_x\text{Cs}_{1-x})\text{PbI}_3$ alloys, where a substantial fraction of EA is replaced with smaller FA and Cs^+ cations, respectively. As mentioned in the previous section, FA and Cs cations were introduced into the EAPbI_3 perovskite structure via post-synthesis cation exchange (See Methods section for details).

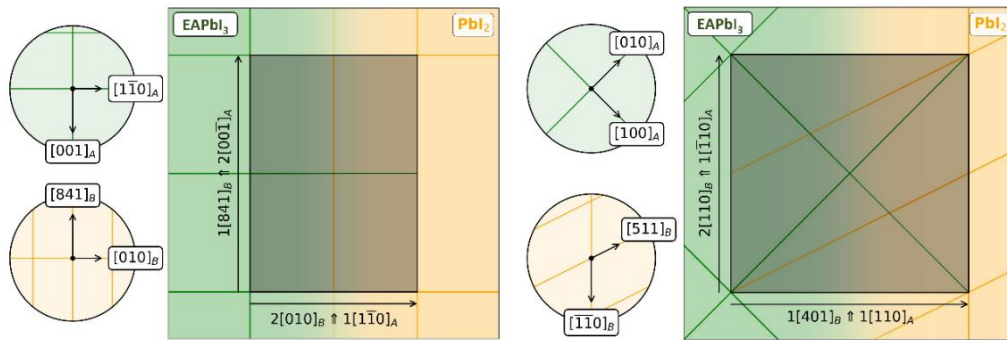


Figure 4.13. Interface supercells and relative orientation of the EAPbI_3 and PbI_2 lattices (in green and orange respectively) for the epitaxial interfaces shown in Figure 4.12e (left) and Figure 4.12f (right). The first interface occurs between the (110) plane of EAPbI_3 and the (10-8) plane of PbI_2 , and is characterized by a supercell area of 116 \AA^2 and 6 % strain. The second interface occurs between the (001) plane of EAPbI_3 and the (-114) plane of PbI_2 , and is characterized by a supercell area of 82 \AA^2 and 6 % strain. We note that this second epitaxial relation is equivalent to the one reported in Ref.²³ or the $\text{PbI}_2/\text{FAPbI}_3$ system. See Ref.³⁶ for details on the interpretation of these diagrams.

In both cases, the compositional tuning induced a red shift of both the absorption edge (Figure 4.15a,c) and the PL (Figure 4.15b,d), which was significantly more marked for FA^+ than for Cs^+ . Also, the PQLY of the FA^+ and Cs^+ alloyed EAPbI_3 NCs increased (Figure 4.16). The partial exchange with Cs^+ had a more prominent effect on the XRD pattern (Figure 4.15e,f), where the unit cell contraction is more significant due to the smaller ionic radius of cesium. Based on the Vegard's law³³, we estimated that the

maximum exchange ratios reached $\sim 55:45$ and $\sim 30:70$ for EA:FA and EA:Cs in alloyed EAPbI_3 NCs, respectively.

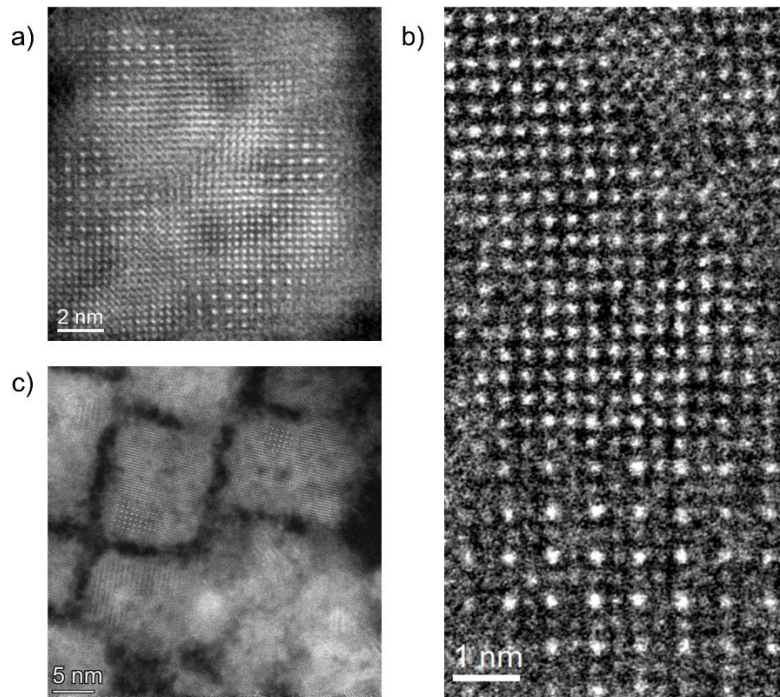


Figure 4.14. HAADF images of (a) $(\text{EA}_x\text{Cs}_{1-x})\text{PbI}_3$ perovskite domains together with trigonal PbI_2 domain in the single NC. The formation of $(\text{EA}_x\text{Cs}_{1-x})\text{PbI}_3/\text{PbI}_2$ heterostructures can be explained by the instability of the EAPbI_3 phase under an electron beam. (c) Lower magnification image of the $(\text{EA}_x\text{Cs}_{1-x})\text{PbI}_3/\text{PbI}_2$ heterostructures. Figure 2b shows an atomic resolution HAADF image of the interface between $(\text{EA}_x\text{Cs}_{1-x})\text{PbI}_3/\text{PbI}_2$ domains. The upper part of the images corresponds to the trigonal PbI_2 lattice at $[-22-3]$ projection; it is connected to the $(\text{EA}_x\text{Cs}_{1-x})\text{PbI}_3$ domain. Due to the very high beam sensitivity of the material, this analysis was made only qualitatively based on the intensity of the corresponding atomic columns. In the HAADF image the brightest columns correspond to Pb/I due to the highest average Z number. The minimum contrast corresponds to higher EA containing $(\text{EA}_x\text{Cs}_{1-x})$ columns. With an increase in Cs doping the contrast of (EA, Cs) columns is increased. The I columns in the $((\text{EA}_x\text{Cs}_{1-x})\text{PbI}_3)$ have a contrast similar to the (EA, Cs) columns enriched in Cs, due to the little difference in Z numbers of I and Cs.

The partial exchange with Cs^+ had a more prominent effect on the XRD pattern (Figure 4.15e,f), where the unit cell contraction is more significant due to the smaller ionic radius of cesium. Based on the Vegard's law³³, we estimated that the maximum exchange ratios reached $\sim 55:45$ and $\sim 30:70$ for EA:FA and EA:Cs in alloyed EAPbI_3 NCs, respectively. (see Table S4.1 and S4.2). The more marked spectral shift induced by FA^+ might appear counterintuitive, given that the unit cell actually contracts less than in the Cs^+ case.

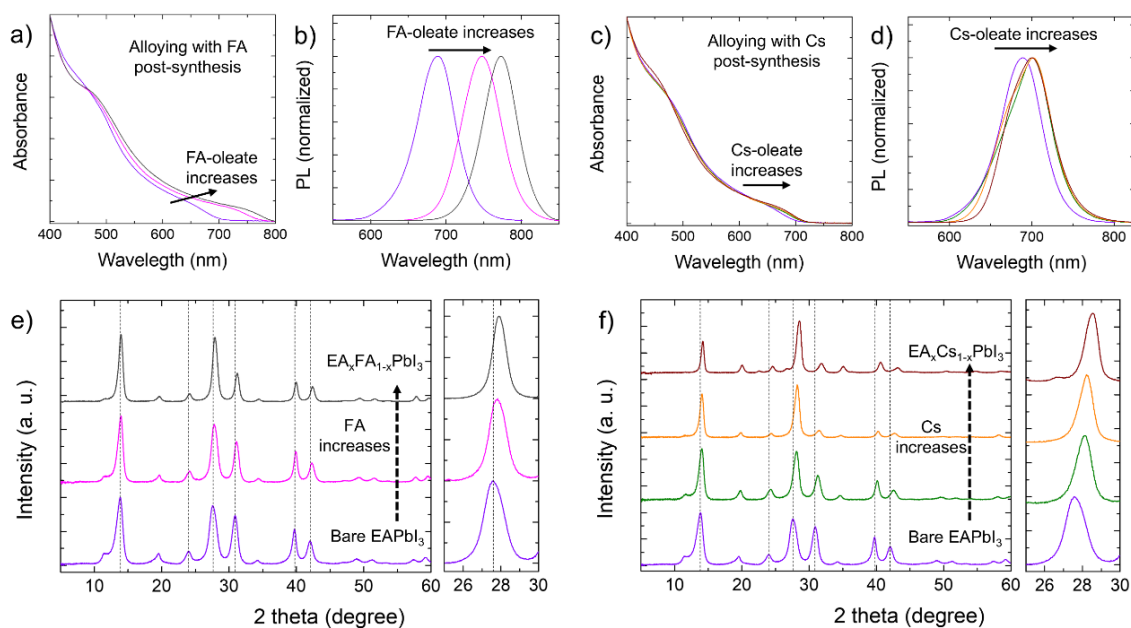


Figure 4.15. Alloys with FA and Cs. Characterization of $(\text{EA}_x\text{FA}_{1-x})\text{PbI}_3$ NCs (left) and $(\text{EA}_x\text{Cs}_{1-x})\text{PbI}_3$ NCs (right). From left to right and from top to bottom: optical absorption spectra (a,c); PL spectra (b,d); XRD patterns (e,f). The cation alloying ratios are extracted from XRD patterns in panels (e, f) by using Vegard's law.³⁵ The EA:FA ratios for $(\text{EA}_x\text{FA}_{1-x})\text{PbI}_3$ NCs were estimated to be 100:0 (violet), 60:30 (pink), and 55:45 (gray) (e). The EA:Cs ratios in $(\text{EA}_x\text{Cs}_{1-x})\text{PbI}_3$ NCs were determined to be approximately 100:0 (violet), 75:25 (green), 60:40 (orange), and 30:70 (red) from bottom to top (f).

However, a similarly non-linear dependence of the band gap when introducing larger A cations was reported for related Ruddlesden-Popper lead-iodide phases,¹⁷ where it was rationalized as the combination of gap widening due to the stretching of Pb-I bonds plus gap narrowing due to the reduced octahedra tilting. In this light, we justify the

stronger spectral shift induced by FA^+ with a shortening of the Pb-I bonds ($\text{EA}^+ = 274$ pm, $\text{FA}^+ = 253$ pm) accompanied by virtually no octahedra tilting, as both EAPbI_3 and FAPbI_3 adopt structures close to the ideal cubic prototype. Conversely, the introduction of the much smaller Cs^+ cation cannot shorten the Pb-I bonds much further, due to physical limits in the inter-ionic distance ($\text{FA}^+ = 253$ pm, $\text{Cs}^+ = 188$ pm), but it does cause major deviations from the ideal cubic symmetry. This is supported by extra peaks appearing in the XRD pattern of $(\text{EA}_x\text{Cs}_{1-x})\text{PbI}_3$ in the $22\text{-}27^\circ$ 2θ range, that are typical of a heavily distorted orthorhombic perovskite structure. In conclusion, the opposite effect of Pb-I bonds shortening and induced octahedra tilting likely balances out in the case of Cs^+ alloying, leaving the spectral properties of $(\text{EA}_x\text{Cs}_{1-x})\text{PbI}_3$ alloys almost unaffected.

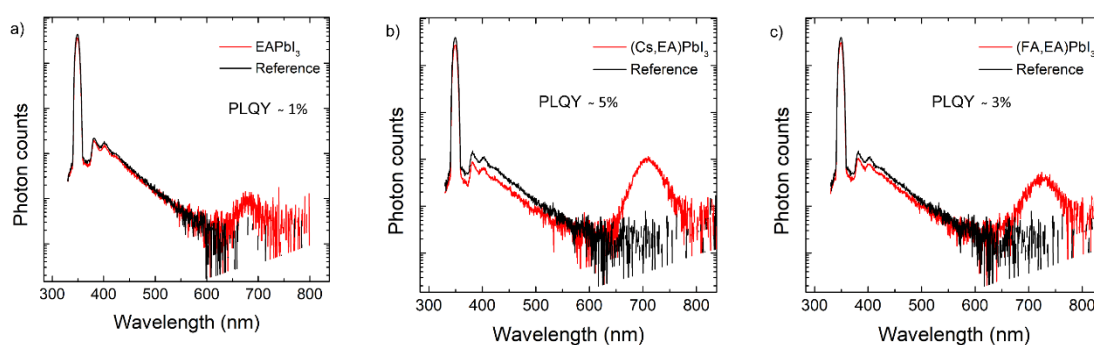


Figure 4.16. Spectra recorded for PLQY measurement of (a) EAPbI_3 , (b) $(\text{Cs}, \text{EA})\text{PbI}_3$, and (c) $(\text{FA}, \text{EA})\text{PbI}_3$ perovskite NCs, respectively.

Table 4.1. Extracted lattice parameters from XRD patterns of the $\text{EA}_x\text{FA}_{(1-x)}\text{PbI}_3$ NCs.

The corresponding composition (here indicating the fraction of EA^+ and FA^+ present in the alloy), was estimated by applying Vegard's law: $x = (d_x - d_B)/(d_A - d_B)$, where d_x , d_A , and d_B are the measured lattice constants of the alloy and of the pure materials A and B , respectively.

Material	Lattice constant (\AA)	Composition ($\text{EA}_x\text{FA}_{(1-x)}\text{PbI}_3$)
EAPbI_3	6.4308	1.00
$\text{EAPbI}_3 + 7 \mu\text{L FA-oleate}$	6.3980	0.61
$\text{EAPbI}_3 + 14 \mu\text{L FA-oleate}$	6.3919	0.54
FAPbI_3	6.3460	0.00

Table 4.2. Extracted lattice parameters from XRD patterns of the $EA_xFA_{(1-x)}PbI_3$ NCs. The corresponding composition (here indicating the fraction of EA^+ and FA^+ present in the alloy) was estimated by applying Vegard's law: $x = (d_x - d_B)/(d_A - d_B)$, where d_x , d_A , and d_B are the measured lattice constants of the alloy and of the pure materials A and B , respectively.

Material	Lattice constant (Å)	Composition ($EA_xCs_{(1-x)}PbI_3$)
EAPbI ₃	6.4308	1.00
EAPbI ₃ + 3.5 μL Cs-oleate	6.3722	0.73
EAPbI ₃ + 7 μL Cs-oleate	6.3481	0.62
EAPbI ₃ + 14 μL Cs-oleate	6.2786	0.29
CsPbI ₃	6.2151	0

Besides alloying, it is known that perovskites with large A^+ cations can be partially stabilized by adopting a thin platelet morphology.¹⁷ The lack of structural constraints in the thin direction of the platelets generates an element of anisotropy extrinsic to the crystal structure of the material,⁴⁰ and allows it to accommodate distortions that would not be compatible with a more extended crystal of the same material. Such mechanism justifies the stability of Ruddlesden-Popper lead-iodide phases¹⁶ when compared to their 3D-perovskite APbI₃ counterparts. However, similar effects were demonstrated also for colloidal perovskite nanoplatelets.¹⁷ Following this direction, we further modified our initial synthesis protocol to induce the formation of EAPbI₃ nanoplatelets, which was achieved by gradually reducing the amount of EA-oleate injected (see Methods). This caused a progressive blue-shift of both the optical absorption and PL spectra, concomitant with the formation of a sharp excitonic peak typical of highly confined perovskite NCs (Figure 4.17a-b). The successful formation of nanoplatelets was independently confirmed by TEM (Figure 4.17c), from which it could be seen that the particles adopt the characteristic face-to-face stacked assembly. Larger area TEM images of the nanoplatelets are reported in Figure 4.18. For the most confined platelets, the position of the spectral features (abs = 550 nm, PL = 577 nm) suggests a thickness of two octahedra layers, that is, 2 ML (Figure 4.17c), which can be gradually increased by adding more EA-oleate during the synthesis. However, this results in a lower level of control over their thickness distribution, as samples containing mostly 3ML nanoplatelets already exhibited

a shoulder in their PL spectrum that is compatible with higher thicknesses (Figure 4.17b). TEM images of the mixed thickness nanoplatelets are reported in Figure 4.19.

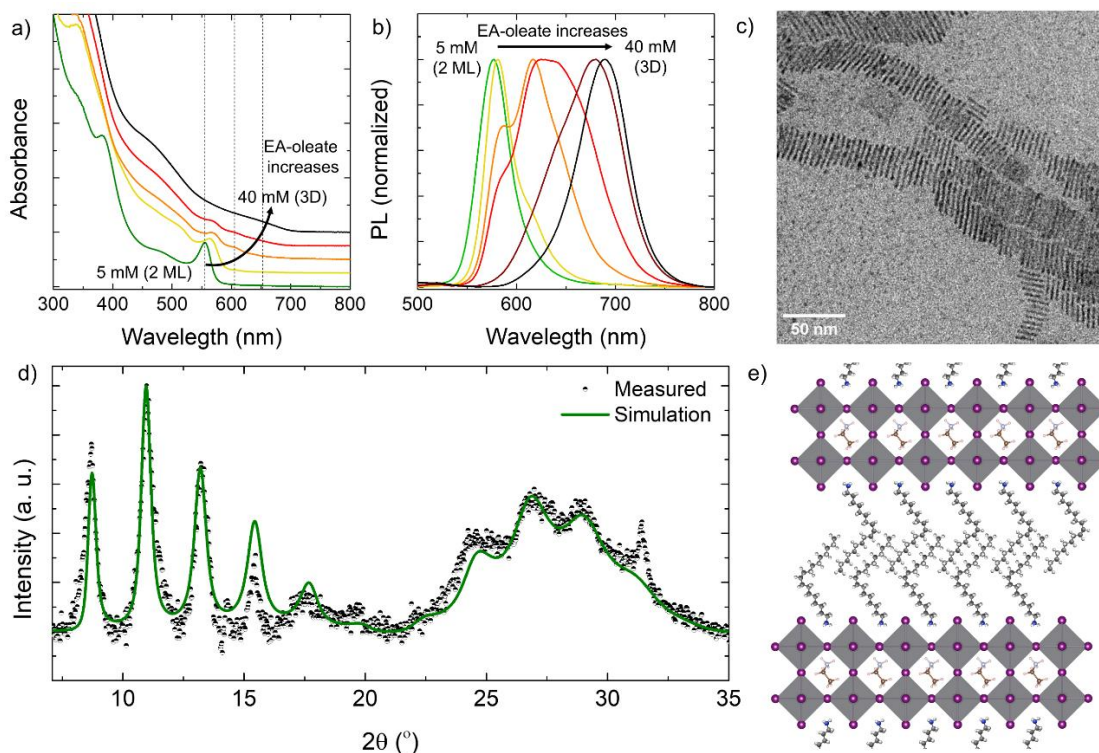


Figure 4.17. EAPbI₃ nanoplatelets. (a, b) Optical absorption (a) and PL (b) spectra of EAPbI₃ samples obtained with different concentrations of EA-oleate in the synthesis. The samples prepared with low EA-oleate concentration show the onset of a sharp excitonic peak, attributed to EAPbI₃ nanoplatelets with a thickness as small as 2 PbI₆ octahedra (2ML in short). (c) TEM images of 2ML EAPbI₃, highlighting the characteristic face-to-face stacking. (d) Structure representation of a stack of 2ML EAPbI₃ nanoplatelets, constructed according to the structural parameters extracted from the multilayer diffraction fit. (e) XRD pattern of 2ML EAPbI₃ analyzed via multilayer diffraction. The characteristic series of periodic peaks is a signature of the self-assembly of the nanoplatelets into flat and ordered stacks.³⁷⁻⁴⁰

An in-depth inspection of the XRD pattern of 2ML EAPbI₃ nanoplatelets, performed via multilayer diffraction analysis,³⁷⁻⁴⁰ revealed major deviations from the crystal structure of EAPbI₃ nanocubes. In particular, the Pb-Pb distance measured in the

platelets is significantly smaller than what we found in EAPbI₃ nanocubes (6.31 Å in platelets vs 6.43 Å in nanocubes, see Figure 4.20 and 4.21 for further discussion).

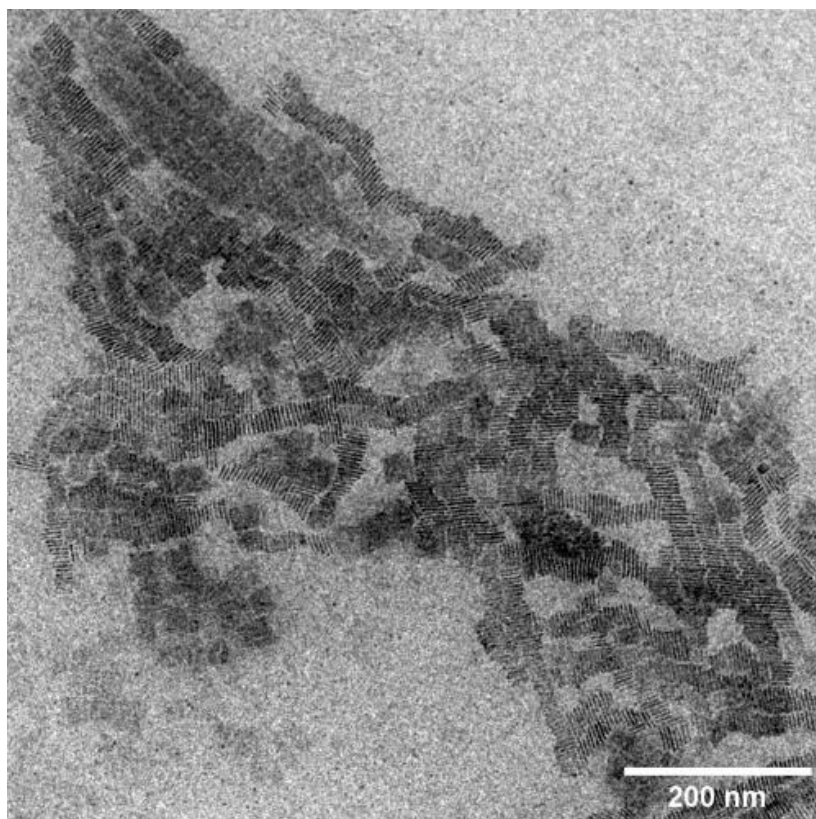


Figure 4.18. Low magnification and TEM images of the two monolayers EAPbI₃ nanoplatelets.

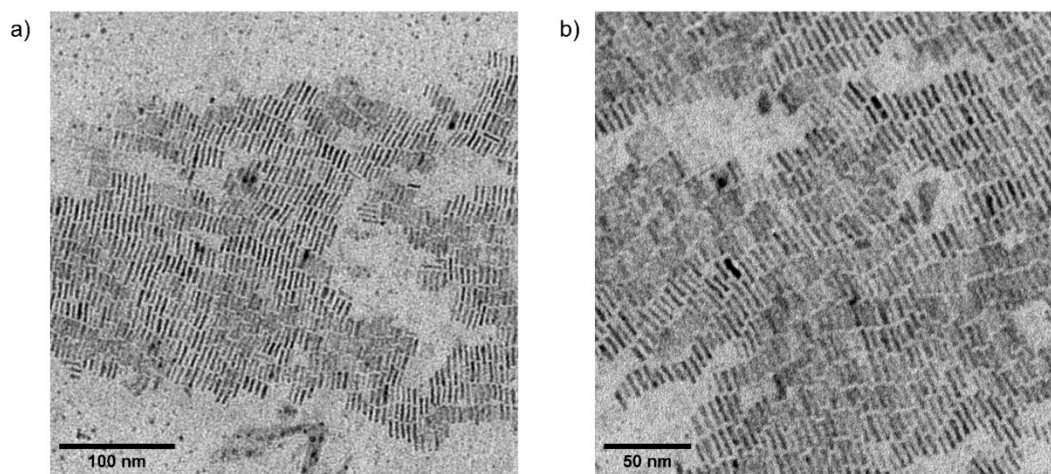


Figure 4.19. (a, b) Bright field TEM images of the mixed thickness EAPbI₃ nanoplatelets in different magnifications.

Unfortunately, multilayer diffraction is not sensitive enough to elucidate the position adopted by the EA cations in the structure, but it clearly indicates that these platelets are able to partially relax the tension imposed on the Pb-I bonds by the exceedingly large ionic radius of EA^+ . Indeed, we observed that EAPbI_3 nanoplatelets are significantly more robust than nanocubes of the same material, as little to no sign of degradation was observed even after several days from the synthesis (see Figure 4.22).

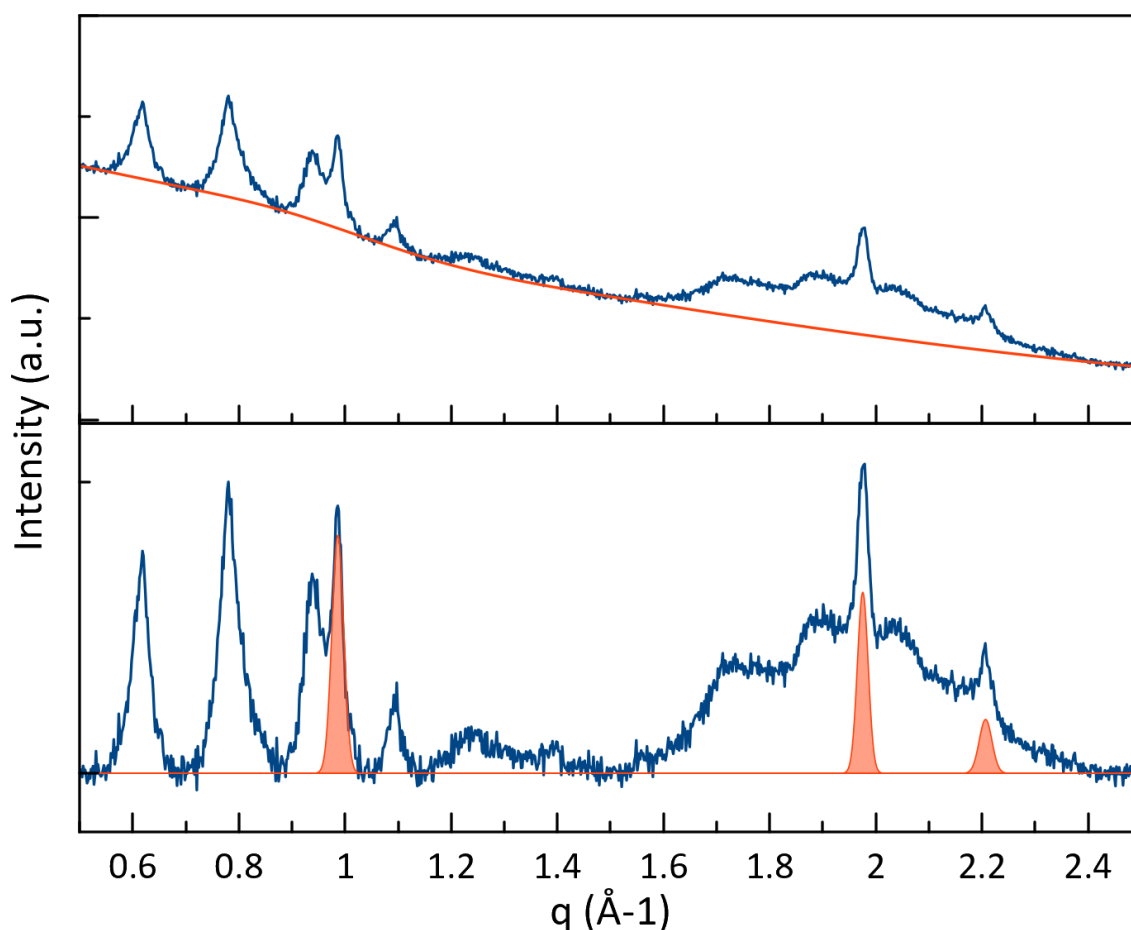


Figure 4.20. The pattern was prepared for the fit by performing a manual background subtraction (top), followed by the subtraction of residual peaks which do belong to EAPbI_3 nanoplatelets, but distributed in the wrong orientation (i.e., not lying flat and parallel to the substrate, and therefore not taking part to the multilayer interference). The resulting XRD pattern has been used as an input for the multilayer diffraction analysis script from Ref.³⁸

The XRD pattern of EAPbI_3 nanoplatelets shown in Figure 4.17d demonstrates the characteristic features of multilayer diffraction, that is a secondary interference effect occurring in XRD patterns of highly ordered assemblies of colloidal nanocrystals. The

phenomenon is described in detail in Refs.^{38,39}, but in short it consists in the formation of sharp fringes due to the constructive interference of radiation scattered by neighboring particles. For nanoplatelets, this XRD profile can be simulated, and in the best cases refined, using the code developed by us in Ref.³⁸.

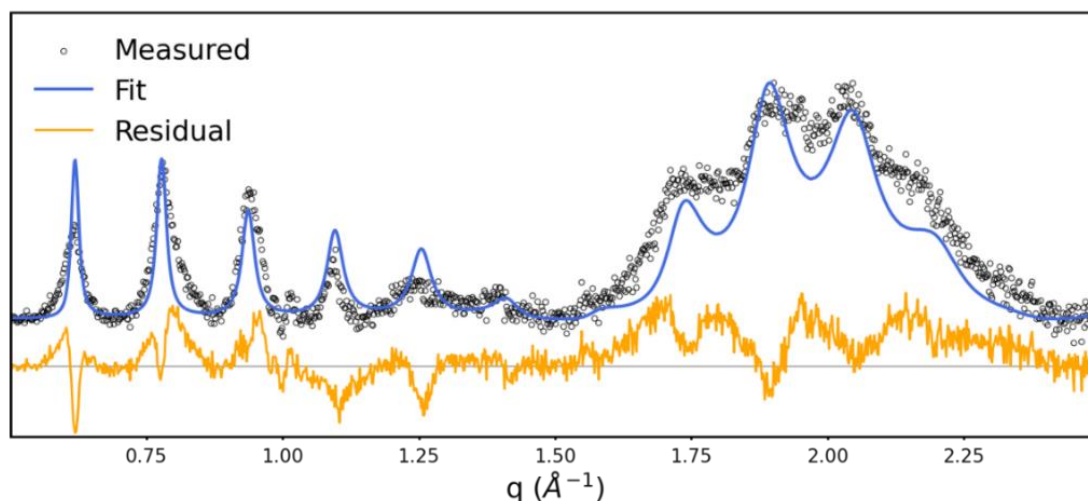


Figure 4.21. Multilayer diffraction simulation of the EAPbI₃ nanoplatelets XRD Pattern.

Although the quality of the pattern was insufficient for an accurate fit, the XRD profile is fully compatible with a thickness of 2 PbI₆ octahedra, corresponding to a nominal stoichiometry of (OLAM)₂EAPb₂I₇. The multilayer periodicity was estimated from the fit to 39.5 Å, while the stacking disorder parameter is estimated to $\sigma L = 0.8$ Å (see Ref.³⁸ for a full description of the method and parameters). The intensity profile in Figure S16 appears different from both Figure S15 and Figure 4 of the Main Text because the data analysis script adopted works by fitting the square module of the structure factor (shown here), and not the experimental intensity (shown in the main text). The two profiles can be interconverted via the Lorentz-Polarization correction factor.⁴¹

Prior to the analysis, the pattern must be prepared by performing a manual background subtraction (Figure 4.20, top), followed by the subtraction of residual peaks that do not belong to the equally spaced series of multilayer interference fringes (Figure 4.20, bottom). In this specific case, two of the residual peaks ($q = 1.0$ Å⁻¹ and $q = 2.0$ Å⁻¹) belong to EAPbI₃ nanoplatelets that are positioned perpendicular to the silicon substrate, and therefore do not take part to multilayer interference, while the peak at 2.2

\AA^{-1} is a spurious reflection from the substrate. From the EAPbI_3 residual peaks we can extract the lateral lattice periodicity (and therefore Pb-Pb distance), that is 6.35 \AA .

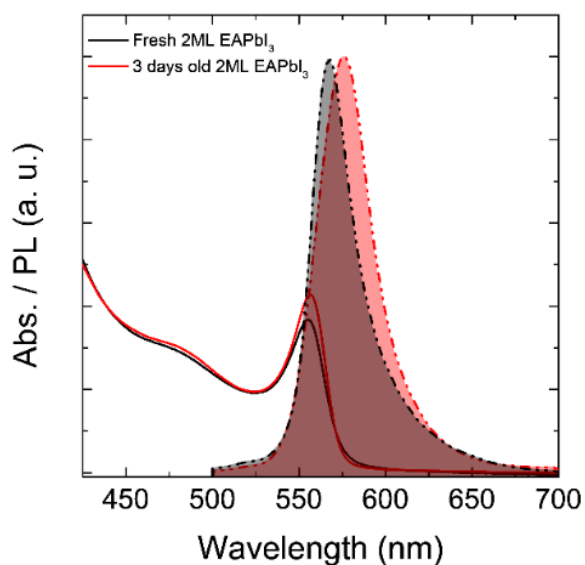


Figure 4.22. Optical absorbance and PL spectra of the 2 ML EAPbI_3 nanoplatelets as prepared (black) and after 3 days of aging (red) under ambient conditions in a closed vial.

4.3. Conclusion

In this work, we demonstrate the synthesis of ethylammonium lead iodide EAPbI_3 perovskite in the form of colloidal NCs. As a material, EAPbI_3 perovskite had never been reported previously. The EA cation was considered not to form a 3D perovskite structure due to its large ionic radius ($\sim 274 \text{ pm}$) and unfavorable Goldschmidt tolerance factor (1.03). Notably, EAPbI_3 is the lead-iodide perovskite with the largest lattice constant (when compared with NCs of similar size). This makes EAPbI_3 an interesting material for validating predictions of the electronic and crystal structure of lead iodide perovskites beyond the boundaries of previously reported phases.

4.4. Methods

4.4.1. Chemicals

Lead (II) iodide (PbI_2 , 99%), Cesium carbonate (Cs_2CO_3 , 99.9%), Formamidine acetate salt (FA-acetate, $\text{HN}=\text{CHNH}_2 \cdot \text{CH}_3\text{COOH}$, 99.9%), Ethylamine solution (2.0 M in tetrahydrofuran), oleylamine (OLAM, 70%), hydroiodic acid (HI, 57 wt. % in water), oleic acid (OA, 90%), Trioctylphosphine oxide (TOPO, 99%) and toluene were all purchased from Sigma-Aldrich except TOPO was purchased from Strem chemicals and used without any further purification.

4.4.2. Synthesis of OLAM-I

10 mL of OLAM and 1.68 mL of HI were loaded in a 100 mL three neck round bottomed flask. The mixture was heated to 130 °C for 2 hours under the nitrogen flow. Subsequently, the reaction was transferred to a vial while it was hot and then cooled to room temperature. 10 mL of dense OLAM-I solution prepared as described above was diluted with 14 mL OLAM for using experiments. OLAM-I solution gels at room temperature therefore prior to use, OLAM-I precursor heated at 120 °C.

4.4.3. Synthesis of EA-oleate

1.25 mL 2 M ethylamine solution in THF, and 2 mL of OA were mixed in a vial for 2 hours at room temperature. Afterwards, 6.75 mL of toluene was added into the vial. Prepared solution stored for further use.

4.4.4. Synthesis of Cs-oleate

407 mg of Cs_2CO_3 , and 2 mL of OA were mixed in a round bottom flask. The mixture was degassed at room temperature for 10 min, and then further degassed for 30 min at 120 °C. Temperature of the reaction vessel was set to 135 °C under the flow of nitrogen gas and kept at the same temperature until a clear solution was obtained. Afterwards, 8 mL of toluene was quickly injected into the reaction flask and the reaction

mixture was cooled down to room temperature. Cs-oleate often precipitate at room temperature. Cs-oleate was heated at 100 °C until all precipitate was dissolved prior to use.

4.4.5. Synthesis of FA-oleate

260 mg of FA-acetate and 2 mL of OA were loaded in a round bottom flask. The mixture was degassed at room temperature for 10 minutes. After that, the solution was inserted preheated oil bath at 130 °C under the nitrogen atmosphere for 5 minutes. Subsequently, the flask was removed from the oil bath and cooled for 2 minutes at ambient temperature. Later, the solution was dried at 55 °C under the vacuum for 10 minutes. And then, the FA-oleate solution was cooled to room temperature and stored for further use. The FA-oleate solution was preheated to 120 °C prior to use until the solution became clear.

4.4.6. Synthesis of Pb-precursor with OLAM-I and OA

0.4 mmol PbI₂, 500 μL of OLAM-I, and 400 μL of OA were loaded in a glass tube and degassed at 80 °C and subsequently, heated to 140 °C under vigorous stirring until all PbI₂ solution became completely clear. Then, 4 mL of toluene was added into the reaction mixture. The precursor solution was cooled down to room temperature and stored for further use.

4.4.7. Synthesis of Pb-precursor with TOPO

0.4 mmol PbI₂, and 400 mg of TOPO were loaded in a glass vial and, heated to 140 °C under vigorous stirring until all PbI₂ solution became completely clear. Then, 4 mL of toluene was added into the reaction mixture. The precursor solution was cooled down to room temperature and stored for further use.

4.4.8. EAPbI₃ NC Synthesis from Pb-precursor with OLAM-I and OA

1 mL of toluene, 200 μ L Pb-precursor, and 300 μ L of EA-oleate were added in a vial, and a slightly yellow solution was obtained. After the addition of 60-300 μ L of the oleic acid, the reaction immediately started, and the solution color was changed to black. The higher amount of the oleic acid used in the synthesis causes the formation of more quantum-confined NCs. The obtained NC solution was centrifuged at 4000 rpm for 2 minutes, and the precipitate and supernatant separated. Then, the precipitate was dispersed in toluene. Further, the supernatant was centrifuged at 14500 rpm for 10 minutes, then the precipitate dispersed toluene, and the supernatant was discarded.

4.4.9. EAPbI₃ NC Synthesis from Pb-precursor with TOPO

500 μ L of toluene, 100 μ L Pb-precursor (TOPO), 7 μ L of OLAM-I solution, and 150 μ L of EA-oleate were added in a vial, and a slightly yellow solution was obtained. After the addition of 100-800 μ L of the oleic acid, the reaction immediately started, and the solution color was changed to black. The higher amount of the oleic acid used in the synthesis causes the formation of more quantum-confined NCs. The obtained NC solution was centrifuged at 6000 rpm for 1 minutes and precipitate discarded and supernatant centrifuged again at 14500 rpm for 6 minutes, and supernatant discarded and precipitate dispersed in toluene. Sometimes precipitate can only be dispersed with the help of the ultrasonication.

4.4.10. EAPbI₃ NPL Synthesis

1 mL of the toluene, 200 μ L Pb-precursor (OLAM-I and OA), and 35 μ L of EA-oleate mixed, respectively. Then, 200 μ L of the oleic acid was added to this solution, and EAPbI₃ NPLs were immediately formed. This solution was centrifuged at 6000 rpm for 1 minute, and the precipitate was redispersed in toluene. After this NPL solution was centrifuged at 6000 rpm for 2 minutes, the precipitate was discarded, and the supernatant was taken for further use. For the TOPO Pb-precursor, 500 μ L toluene, 100 μ L Pb-oleate, 7.5 μ L OLAM-I solution, and 17.5 μ L EA-oleate mixed, respectively. After 200 μ L OA

was added, EAPbI₃ NPLs were immediately formed. The same centrifuge procedure described above was applied to separate the NPLs.

4.4.11. Cs or FA Alloyed EAPbI₃ NC Synthesis

After the synthesis of the EAPbI₃ perovskite NCs. (EA_xFA_{1-x})PbI₃ NCs 7 μL or 14 μL FA-oleate solution, for (EA_xCs_{1-x})PbI₃ NCs 3.5 μL, 7 μL, or 14 μL Cs-oleate solution was added to EAPbI₃ crude NC solution. It should be noted that half the amount of FA-oleate and Cs-oleate described above was used to alloy EAPbI₃ NCs synthesized using the TOPO route, as the TOPO synthesis contained half the amount of Pb and EA precursors. The cleaning procedure was the same as the EAPbI₃ NCs cleaning procedure described above; it only was changed depending on which PbI₂-precursor type was used.

4.4.12. Optical Characterization

UV-Vis absorption spectra were obtained using a Varian Cary 300 UV-Vis absorption spectrophotometer (Agilent). The spectra were collected by diluting 40 μL of the sample in toluene in 3 mL of toluene. Photoluminescence spectra were obtained on a Varian Cary Eclipse Spectrophotometer (Agilent). Time-resolved photoluminescence spectra were obtained using an Edinburgh FLS900 fluorescence spectrophotometer PL quantum yield measurements. PL decay traces were measured with a 508 nm picosecond pulsed laser diode (EPL-510, Edinburgh Instruments). Quantum yield measurements were acquired using a calibrated integrating sphere with $\lambda_{\text{ex}} = 350$ nm for all measurements (FS-5, Edinburgh Instruments). All solutions were diluted to an optical density of 0.1 - 0.2 at the excitation wavelength to minimize the reabsorption of the fluorophore. Quartz cuvettes with an optical path length of 1 cm were used for all-optical analyses.

4.4.13. Powder X-ray Diffraction (XRD) Analysis

XRD patterns were obtained using a PANalytical Empyrean X-ray diffractometer equipped with a 1.8 kW Cu K α ceramic X-ray tube and a PIXcel3D 2 × 2 area detector operating at 45 kV and 40 mA. The diffraction patterns were collected in the air at room

temperature using parallel beam (PB) geometry and symmetric reflection mode. All XRD samples were prepared by drop-casting a concentrated solution on a zero-diffraction quartz wafer.

The Vegard's law^{33,42,43} analysis of A⁺ cation alloys was performed by extracting the pseudocubic lattice parameters of samples via Le Bail fitting, like shown in Figure S3. The same approach was adopted to extract the lattice constants of pure CsPbI₃ (6.216 Å) and FAPbI₃ (6.346 Å) NCs, which serve as references for the application of Vegard's law. We opted not to adopt published references because the lattice constant of NCs can be slightly different from that of the corresponding bulk, and to ensure a consistent treatment and error cancellation, if present.

The multilayer diffraction analysis of EAPbI₃ nanoplatelets was performed using the code published.³⁸ Due to the lack of an established bulk structure for EAPbI₃, and to the likely disordered position of the EA⁺ cations, we opted to model its electron density by including in the multilayer model 2 atoms of carbon and 1 of nitrogen at the center of the unit cell. This choice is adequate for a preliminary modelling, as the EA⁺ contribution to the total electron density is negligible (18 electrons / formula unit, excluding hydrogens) compared to the contribution of heavy atoms (Pb²⁺ + 3 I⁻, 242 electrons / formula unit). The impact of EA becomes even smaller when considering that the actual stoichiometry of such nanoplatelets is (OLAM)₂EAPb₂I₇, as their thickness is just 2 PbI₆ octahedra.

4.4.14. Electron Microscopy

Bright field TEM images were acquired on a JEOL JEM-1400 microscope equipped with a thermionic gun at an accelerating voltage of 120 kV. The samples were prepared by drop-casting diluted NC suspensions onto 200 mesh carbon-coated copper grids.

High-resolution scanning transmission electron microscopy (STEM) images were acquired on a probe-corrected Thermo Fisher Spectra 30–300 S/TEM operated at 300 kV. Atomic resolution images were acquired on a high-angle annular dark field (HAADF) detector with a current of 30 pA and a beam convergence semiangle of 25 mrad.

4.4.15. Atomistic Simulations

All DFT simulations were performed with the VASP software⁴⁴ within the projector augmented plane wave⁴⁵ and adopting the PBE functional⁴⁶. For the simulated annealing molecular dynamics (MD) runs, the initial structure was generated by substituting -H with -CH₃ in the ground state of methylammonium lead halide perovskite⁴⁷ and contained 8 formula units. The temperature was increased to 1000 K in 5000 steps (time step 1 fs, NpT ensemble, Langevin thermostat). Then, the MD was run for further 50000 steps, taking one structure every 5000 steps and cooling it down to T=200 K in 5000 steps (slower cooling -40000 steps- adopted for those structures that would otherwise lose their perovskite structure upon cooling; one of them still cooled down in a non-perovskite structure and was thus discarded). Two additional structures were obtained with milder annealing at T=450 K. All these ab initio MD simulations were performed with gamma-point only reciprocal space sampling and a plane-wave energy cutoff of 320 eV. All the structures obtained were then tightly relaxed ($\Delta E=10^{-6}$) with a 2x2x2 k points sampling and an energy cutoff of 500 eV, adding the Tkatchenko-Sheffler correction⁴⁸ to account for dispersion forces, which was shown to give accurate results in methylammonium lead halide perovskites.⁴⁹

4.5. References

1. Shamsi, J.; Urban, A. S.; Imran, M.; De Trizio, L.; Manna, L. Metal Halide Perovskite Nanocrystals: Synthesis, Post-Synthesis Modifications, and Their Optical Properties. *Chem Rev* **2019**, *119* (5), 3296–3348.
2. Akkerman, Q. A.; Manna, L. What Defines a Halide Perovskite? *ACS Energy Letters*. American Chemical Society **2020**, pp 604–610.
3. Akkerman, Q. A.; Rainò, G.; Kovalenko, M. V.; Manna, L. Genesis, Challenges and Opportunities for Colloidal Lead Halide Perovskite Nanocrystals. *Nat Mater* **2018**, *17* (5), 394–405.
4. Dey, A.; Ye, J.; De, A.; Debroye, E.; Ha, S. K.; Bladt, E.; Kshirsagar, A. S.; Wang, Z.; Yin, J.; Wang, Y.; Quan, L. N.; Yan, F.; Gao, M.; Li, X.; Shamsi, J.; Debnath, T.; Cao, M.; Scheel, M. A.; Kumar, S.; Steele, J. A.; Gerhard, M.; Chouhan, L.; Xu, K.; Wu, X.; Li, Y.; Zhang, Y.; Dutta, A.; Han, C.; Vincon, I.; Rogach, A. L.;

- Nag, A.; Samanta, A.; Korgel, B. A.; Shih, C.-J.; Gamelin, D. R.; Son, D. H.; Zeng, H.; Zhong, H.; Sun, H.; Demir, H. V.; Scheblykin, I. G.; Mora-Seró, I.; Stolarczyk, J. K.; Zhang, J. Z.; Feldmann, J.; Hofkens, J.; Luther, J. M.; Pérez-Prieto, J.; Li, L.; Manna, L.; Bodnarchuk, M. I.; Kovalenko, M. V.; Roeffaers, M. B. J.; Pradhan, N.; Mohammed, O. F.; Bakr, O. M.; Yang, P.; Müller-Buschbaum, P.; Kamat, P. V.; Bao, Q.; Zhang, Q.; Krahne, R.; Galian, R. E.; Stranks, S. D.; Bals, S.; Biju, V.; Tisdale, W. A.; Yan, Y.; Hoye, R. L. Z.; Polavarapu, L. State of the Art and Prospects for Halide Perovskite Nanocrystals. *ACS Nano* **2021**, *15* (7), 10775–10981.
5. Saliba, M.; Matsui, T.; Seo, J. Y.; Domanski, K.; Correa-Baena, J. P.; Nazeeruddin, M. K.; Zakeeruddin, S. M.; Tress, W.; Abate, A.; Hagfeldt, A.; Grätzel, M. Cesium-Containing Triple Cation Perovskite Solar Cells: Improved Stability, Reproducibility and High Efficiency. *Energy Environ Sci* **2016**, *9* (6), 1989–1997.
 6. Livakas, N.; Toso, S.; Ivanov, Y. P.; Das, T.; Chakraborty, S.; Divitini, G.; Manna, L. CsPbCl₃ → CsPbI₃ Exchange in Perovskite Nanocrystals Proceeds through a Jump-the-Gap Reaction Mechanism. *J Am Chem Soc* **2023**, *145* (37), 20442–20450.
 7. Turren-Cruz, S.-H.; Hagfeldt, A.; Saliba, M. Methylammonium-Free, High-Performance, and Stable Perovskite Solar Cells on a Planar Architecture. *Science* **2018**, *362* (6413), 449–453.
 8. Otero-Martínez, C.; Imran, M.; Schrenker, N. J.; Ye, J.; Ji, K.; Rao, A.; Stranks, S. D.; Hoye, R. L. Z.; Bals, S.; Manna, L.; Pérez-Juste, J.; Polavarapu, L. Fast A-Site Cation Cross-Exchange at Room Temperature: Single-to Double- and Triple-Cation Halide Perovskite Nanocrystals. *Angewandte Chemie - International Edition* **2022**, *61* (34).
 9. Goldschmidt, V. M. Die Gesetze Der Krystallochemie. *Naturwissenschaften* **1926**, *14* (21), 477–485.
 10. Protesescu, L.; Yakunin, S.; Bodnarchuk, M. I.; Krieg, F.; Caputo, R.; Hendon, C. H.; Yang, R. X.; Walsh, A.; Kovalenko, M. V. Nanocrystals of Cesium Lead Halide Perovskites (CsPbX₃, X = Cl, Br, and I): Novel Optoelectronic Materials Showing Bright Emission with Wide Color Gamut. *Nano Lett* **2015**, *15* (6), 3692–3696.

11. Zhang, F.; Zhong, H.; Chen, C.; Wu, X.; Hu, X.; Huang, H.; Han, J.; Zou, B.; Dong, Y. Brightly Luminescent and Color-Tunable Colloidal $\text{CH}_3\text{NH}_3\text{PbX}_3$ (X = Br, I, Cl) Quantum Dots: Potential Alternatives for Display Technology. *ACS Nano* **2015**, *9* (4), 4533–4542.
12. Protesescu, L.; Yakunin, S.; Kumar, S.; Bär, J.; Bertolotti, F.; Masciocchi, N.; Guagliardi, A.; Grotevent, M.; Shorubalko, I.; Bodnarchuk, M. I.; Shih, C.-J.; Kovalenko, M. V. Dismantling the “Red Wall” of Colloidal Perovskites: Highly Luminescent Formamidinium and Formamidinium-Cesium Lead Iodide Nanocrystals. *ACS Nano* **2017**, *11* (3), 3119–3134.
13. Bodnarchuk, M. I.; Feld, L. G.; Zhu, C.; Boehme, S. C.; Bertolotti, F.; Avaro, J.; Aebli, M.; Mir, S. H.; Masciocchi, N.; Erni, R.; Chakraborty, S.; Guagliardi, A.; Rainò, G.; Kovalenko, M. V. Colloidal Aziridinium Lead Bromide Quantum Dots. *ACS Nano* **2024**, *18* (7), 5684–5697.
14. Petrosova, H. R.; Kucheriv, O. I.; Shova, S.; Gural’skiy, I. A. Aziridinium Cation Templating 3D Lead Halide Hybrid Perovskites. *Chemical Communications* **2022**, *58* (38), 5745–5748.
15. Akkerman, Q. A.; Martínez-Sarti, L.; Goldoni, L.; Imran, M.; Baranov, D.; Bolink, H. J.; Palazon, F.; Manna, L. Molecular Iodine for a General Synthesis of Binary and Ternary Inorganic and Hybrid Organic-Inorganic Iodide Nanocrystals. *Chemistry of Materials* **2018**, *30* (19), 6915–6921.
16. Fu, Y.; Hautzinger, M. P.; Luo, Z.; Wang, F.; Pan, D.; Aristov, M. M.; Guzei, I. A.; Pan, A.; Zhu, X.; Jin, S. Incorporating Large A Cations into Lead Iodide Perovskite Cages: Relaxed Goldschmidt Tolerance Factor and Impact on Exciton–Phonon Interaction. *ACS Cent Sci* **2019**, *5* (8), 1377–1386.
17. Hautzinger, M. P.; Pan, D.; Pigg, A. K.; Fu, Y.; Morrow, D. J.; Leng, M.; Kuo, M.-Y.; Spitha, N.; Lafayette, D. P.; Kohler, D. D.; Wright, J. C.; Jin, S. Band Edge Tuning of Two-Dimensional Ruddlesden–Popper Perovskites by A Cation Size Revealed through Nanoplates. *ACS Energy Lett* **2020**, *5* (5), 1430–1437.
18. Li, X.; Fu, Y.; Pedesseau, L.; Guo, P.; Cuthriell, S.; Hadar, I.; Even, J.; Katan, C.; Stoumpos, C. C.; Schaller, R. D.; Harel, E.; Kanatzidis, M. G. Negative Pressure Engineering with Large Cage Cations in 2D Halide Perovskites Causes Lattice Softening. *J Am Chem Soc* **2020**, *142* (26), 11486–11496.
19. Toso, S.; Akkerman, Q. A.; Martín-García, B.; Prato, M.; Zito, J.; Infante, I.; Dang, Z.; Moliterni, A.; Giannini, C.; Bladt, E.; Lobato, I.; Ramade, J.; Bals, S.;

- Buha, J.; Spirito, D.; Mugnaioli, E.; Gemmi, M.; Manna, L. Nanocrystals of Lead Chalcogenides: A Series of Kinetically Trapped Metastable Nanostructures. *J Am Chem Soc* **2020**, *142* (22), 10198–10211.
20. Rothmann, M. U.; Kim, J. S.; Borchert, J.; Lohmann, K. B.; O’Leary, C. M.; Shearer, A. A.; Clark, L.; Snaith, H. J.; Johnston, M. B.; Nellist, P. D.; Herz, L. M. Atomic-Scale Microstructure of Metal Halide Perovskite. *Science* **2020**, *370* (6516).
 21. Rothmann, M. U.; Lohmann, K. B.; Borchert, J.; Johnston, M. B.; McKenna, K. P.; Herz, L. M.; Nellist, P. D. Atomistic Understanding of the Coherent Interface Between Lead Iodide Perovskite and Lead Iodide. *Adv Mater Interfaces* **2023**, *10* (28).
 22. Guvenc, C. M.; Tunc, I.; Balci, S. L₂[GA_xFA_{1-x}PbI₃]PbI₄ (0 ≤ x ≤ 1) Ruddlesden–Popper Perovskite Nanocrystals for Solar Cells and Light-Emitting Diodes. *ACS Appl Nano Mater* **2022**, *5* (1), 1078–1085.
 23. Almeida, G.; Ashton, O. J.; Goldoni, L.; Maggioni, D.; Petralanda, U.; Mishra, N.; Akkerman, Q. A.; Infante, I.; Snaith, H. J.; Manna, L. The Phosphine Oxide Route toward Lead Halide Perovskite Nanocrystals. *J Am Chem Soc* **2018**, *140* (44), 14878–14886.
 24. Akkerman, Q. A.; Nguyen, T. P. T.; Boehme, S. C.; Montanarella, F.; Dirin, D. N.; Wechsler, P.; Beiglböck, F.; Rainò, G.; Erni, R.; Katan, C.; Even, J.; Kovalenko, M. V. Controlling the Nucleation and Growth Kinetics of Lead Halide Perovskite Quantum Dots. *Science* **2022**, *377* (6613), 1406–1412.
 25. Saleh, G.; Biffi, G.; Di Stasio, F.; Martín-García, B.; Abdelhady, A. L.; Manna, L.; Krahne, R.; Artyukhin, S. Methylammonium Governs Structural and Optical Properties of Hybrid Lead Halide Perovskites through Dynamic Hydrogen Bonding. *Chemistry of Materials* **2021**, *33* (21), 8524–8533.
 26. Knutson, J. L.; Martin, J. D.; Mitzi, D. B. Tuning the Band Gap in Hybrid Tin Iodide Perovskite Semiconductors Using Structural Templating. *Inorg Chem* **2005**, *44* (13), 4699–4705.
 27. Mao, L.; Wu, Y.; Stoumpos, C. C.; Traore, B.; Katan, C.; Even, J.; Wasielewski, M. R.; Kanatzidis, M. G. Tunable White-Light Emission in Single-Cation-Templated Three-Layered 2D Perovskites (CH₃CH₂NH₃)₄Pb₃Br₁₀-XCl_x. *J Am Chem Soc* **2017**, *139* (34), 11956–11963.

28. Goesten, M. G.; Hoffmann, R. Mirrors of Bonding in Metal Halide Perovskites. *J Am Chem Soc* **2018**, *140* (40), 12996–13010.
29. Kovalenko, M. V; Protesescu, L.; Bodnarchuk, M. I. *Properties and Potential Optoelectronic Applications of Lead Halide Perovskite Nanocrystals*; **2017**; Vol. 358.
30. Zhu, H.; Teale, S.; Lintangpradipto, M. N.; Mahesh, S.; Chen, B.; McGehee, M. D.; Sargent, E. H.; Bakr, O. M. Long-Term Operating Stability in Perovskite Photovoltaics. *Nature Reviews Materials*. Nature Research September 1, **2023**, *8* (9), 569–586.
31. Zhumeckenov, A. A.; Saidaminov, M. I.; Haque, M. A.; Alarousu, E.; Sarmah, S. P.; Murali, B.; Dursun, I.; Miao, X. H.; Abdelhady, A. L.; Wu, T.; Mohammed, O. F.; Bakr, O. M. Formamidinium Lead Halide Perovskite Crystals with Unprecedented Long Carrier Dynamics and Diffusion Length. *ACS Energy Lett* **2016**, *1* (1), 32–37.
32. Muralidhar, J. R.; Salikolimi, K.; Adachi, K.; Hashizume, D.; Kodama, K.; Hirose, T.; Ito, Y.; Kawamoto, M. Chemical Storage of Ammonia through Dynamic Structural Transformation of a Hybrid Perovskite Compound. *J Am Chem Soc* **2023**, *145* (31), 16973–16977.
33. Denton, A. R.; Ashcroft, N. W. *Vegard's Law*; **1991**; Vol. 43.
34. Toso, S.; Dardzinski, D.; Manna, L.; Marom, N. Fast Prediction of Ionic Epitaxial Interfaces with OGRE Demonstrated for Colloidal Heterostructures of Lead Halide Perovskites.
35. Moayedpour, S.; Dardzinski, D.; Yang, S.; Hwang, A.; Marom, N. Structure Prediction of Epitaxial Inorganic Interfaces by Lattice and Surface Matching with OGRE. *Journal of Chemical Physics* **2021**, *155* (3).
36. Moayedpour, S.; Bier, I.; Wen, W.; Dardzinski, D.; Isayev, O.; Marom, N. Structure Prediction of Epitaxial Organic Interfaces with OGRE, Demonstrated for Tetracyanoquinodimethane (TCNQ) on Tetrathiafulvalene (TTF). *The Journal of Physical Chemistry C* **2023**, *127* (21), 10398–10410.
37. Toso, S.; Baranov, D.; Altamura, D.; Scattarella, F.; Dahl, J.; Wang, X.; Marras, S.; Alivisatos, A. P.; Singer, A.; Giannini, C.; Manna, L. Multilayer Diffraction Reveals That Colloidal Superlattices Approach the Structural Perfection of Single Crystals. *ACS Nano* **2021**, *15* (4), 6243–6256.

38. Toso, S.; Baranov, D.; Giannini, C.; Manna, L. Structure and Surface Passivation of Ultrathin Cesium Lead Halide Nanoplatelets Revealed by Multilayer Diffraction. *ACS Nano* **2021**, *15* (12), 20341–20352.
39. Toso, S.; Baranov, D.; Filippi, U.; Giannini, C.; Manna, L. Collective Diffraction Effects in Perovskite Nanocrystal Superlattices. *Acc Chem Res* **2023**, *56* (1), 66–76.
40. Akkerman, Q. A.; Martín-García, B.; Buha, J.; Almeida, G.; Toso, S.; Marras, S.; Bonaccorso, F.; Petralanda, U.; Infante, I.; Manna, L. Ultrathin Orthorhombic PbS Nanosheets. *Chemistry of Materials* **2019**, *31* (19), 8145–8153.
41. Fullerton, E. E.; Schuller, I. K.; Vanderstraeten, H.; Bruynseraede, Y. *Structural Refinement of Superlattices from X-Ray Diffraction*; **1991**; Vol. 45.
42. Cullity, B. D., *Elements of X-Ray Diffraction*; Addison-Wesley Publishing Company, Inc., **1978**.
43. Holder, C. F.; Schaak, R. E. Tutorial on Powder X-Ray Diffraction for Characterizing Nanoscale Materials. *ACS Nano*. American Chemical Society, **2019**, *13* (7), 7359–7365.
44. Kresse, G.; Furthmüller, J. Efficient Iterative Schemes for Ab Initio Total-Energy Calculations Using a Plane-Wave Basis Set. *Phys Rev B* **1996**, *54* (16), 11169–11186.
45. Kresse, G.; Joubert, D. From Ultrasoft Pseudopotentials to the Projector Augmented-Wave Method. *Phys Rev B* **1999**, *59* (3), 1758–1775.
46. Perdew, J. P.; Burke, K.; Ernzerhof, M. Generalized Gradient Approximation Made Simple. *Phys Rev Lett* **1996**, *77* (18), 3865–3868.
47. Hata, T.; Giorgi, G.; Yamashita, K.; Caddeo, C.; Mattoni, A. Development of a Classical Interatomic Potential for MAPbBr₃. *Journal of Physical Chemistry C* **2017**, *121* (7), 3724–3733.
48. Tkatchenko, A.; Scheffler, M. Accurate Molecular van Der Waals Interactions from Ground-State Electron Density and Free-Atom Reference Data. *Phys Rev Lett* **2009**, *102* (7).
49. Beck, H.; Gehrman, C.; Egger, D. A. Structure and Binding in Halide Perovskites: Analysis of Static and Dynamic Effects from Dispersion-Corrected Density Functional Theory. *APL Mater* **2019**, *7* (2).

CHAPTER 5

CONCLUSION AND OUTLOOK

5.1. Conclusion

This thesis focuses on the synthesis of halide perovskite nanocrystals (NCs) using large perovskite cations (EA and GA). To achieve this, we developed a room-temperature, polar solvent-free synthesis method, which was utilized in all the projects presented in this thesis.

In the first project, we successfully synthesized colloidal Ruddlesden-Popper (R-P) perovskite $L_2[GA_xFA_{x-1}PbI_3]PbI_4$ NCs and tuned their optical properties by modulating the GA and FA concentrations.

In the second project, we achieved the synthesis of $CsPbX_3$ ($X = Cl, Br$) nanocubes at room temperature. We demonstrated that GA cations bind more favorably to the perovskite surface compared to long-chained alkyl ammonium molecules. Furthermore, the smaller GA molecules prevent the restricted monomer addition caused by long-chained alkyl molecules, forming $CsPbX_3$ ($X = Cl, Br$) nanocubes with high photoluminescence quantum yield (PLQY) values.

In the third project, we successfully synthesized $EAPbI_3$ perovskite NCs, a material not previously demonstrated in prior studies. This new member of the family exhibits the largest halide perovskite lattice constant reported to date. Our findings show that materials unattainable in bulk form can be synthesized at the nanoscale due to the relaxed structural constraints imposed by finite size.

5.2. Outlook

Colloidal lead halide perovskite nanocrystals (NCs) have gained significant attention due to their defect tolerance, tunable band gaps across the visible spectrum, high photoluminescence quantum yield (PLQY) values, and scintillation capabilities. However, these materials are often suffered from instability, both in phase and PL, under ambient conditions. A-site cation engineering has emerged as a powerful strategy to

enhance the stability of halide perovskites at ambient conditions. Introducing additional A-site cations offers new compositions that not only improve stability but also enable fine-tuning of the optical properties of perovskites. Identifying and incorporating novel organic cations capable of supporting the perovskite structure could pave the way toward achieving stable halide perovskite materials.

VITA

EDUCATION

- 2018-2024 Doctor of Philosophy
*Department of Material Science and Engineering
Izmir Institute of Technology*
- 2014-2017 Master of Science
*Department of Material Science and Engineering
Anadolu University*
- 2009-2014 Bachelor of Science
*Department of Material Science and Engineering
Anadolu University*

WORK EXPERIENCE

- 2018- Research Assistant
*Department of Material Science and Engineering
Izmir Institute of Technology*
- 2023-2024 Visiting Researcher (TUBİTAK 2214-A Scholar)
*Nanochemistry
Italian Institute of Technology*

PUBLICATIONS

1. Guvenc, C. M.; Toso, S.; Yurii, P. I.; Saleh, G.; Balci, S.; Divitini, G.; Manna L., Breaking the Boundaries of the Goldschmidt Tolerance Factor with Ethylammonium Lead Iodide Perovskite Nanocrystals. 2024. (*Submitted*)
2. Guvenc, C. M.; Kocabas, A.; Balci, S., Polar Solvent-Free Room Temperature Synthesis of CsPbX₃ (X = Br, Cl) Perovskite Nanocubes. *Journal of Materials Chemistry C*, 2023, 11 (8), 3039-3049.
3. Sarisozen, S.; Polat, N.; Balci, F. M.; Guvenc, C. M.; Kocabas, C.; Yaghioglu, H. G.; Balci, S., Strong Coupling of Carbon Quantum Dots in Liquid Crystals. *The Journal of Physical Chemistry Letters*, 2022, 13 (16), 3562-3570.
4. Guvenc, C. M.; Tunc I.; Balci, S., L₂[GaxFA1-xPbI₃]PbI₄ (0 ≤ x ≤ 1) Ruddlesden-Popper Perovskite Nanocrystals for Solar Cells and Light-Emitting Diodes. *ACS Applied Nano Materials*, 2022, 5, 1078-1085.
5. Guvenc, C. M.; Balci, S., Seed mediated synthesis of colloidal 2D halide perovskite nanoplatelets. *ChemNanoMat*, 2021, 7 (11), 1249-1257.
6. Balci, F. M.; Sarisozen, S.; Polat, N.; Guvenc, C. M.; Karadeniz U.; Tertemiz A.; Balci, S., Laser assisted synthesis of anisotropic metal nanocrystals and strong light-matter coupling in decahedral bimetallic nanocrystals. *Nanoscale Advances*, 2021, 3 (6), 1674-1681.
7. Aouadja F.; Bouzerara F.; Guvenc, C. M.; Demir, M. M., Fabrication and properties of novel porous ceramic membrane supports from the (Sig) diatomite and alumina mixtures. *Boletín de la Sociedad Española de Cerámica y Vidrio*, 2021.
8. Guvenc, C. M.; Polat, N.; Balci, S., Strong plasmon-exciton coupling in colloidal halide perovskite nanocrystals near a metal film. *Journal of Materials Chemistry C*, 2020, 8 (46), 16520-16526.
9. Guvenc, C. M.; Balci, F. M.; Sarisozen, S.; Polat, N.; Balci, S., Colloidal Bimetallic Nanorings for Strong Plasmon Exciton Coupling. *The Journal of Physical Chemistry C* 2020, 124 (15), 8334-8340.
10. Guvenc, C. M.; Yalcinkaya, Y.; Ozen, S.; Sahin, H.; Demir, M. M., Gd³⁺-Doped α-CsPbI₃ Nanocrystals with Better Phase Stability and Optical Properties. *The Journal of Physical Chemistry C* 2019, 123 (40), 24865-24872.
11. Guvenc, C. M.; Adem, U., Influence of aging on electrocaloric effect in Li⁺ doped BaTiO₃ ceramics. *J. Alloys Compd.* 2019, 791, 674-680.
12. Özer, İ. Ö.; Güvenç, Ç. M., A systematic procedure to study hot pressing and spark plasma sintering kinetics. *Anadolu University Journal of Science and Technology A- Applied Sciences and Engineering*, 2017, 18(2), 419 – 428.